UNIVERSIDADE ESTADUAL DE CAMPINAS

Faculdade de Engenharia Elétrica e de Computação

BRUNO GUILHERME AGUIAR FREITAS

SUPERCAPACITOR: DEVELOPMENT OF SELF-SUPPORTED ELECTRODES, ELECTROCHEMICAL ANALYSIS AND ADVANCED STUDIES IN OPERATING REGIME

SUPERCAPACITORES: DESENVOLVIMENTO DE ELETRODOS AUTOSSUSTENTÁVEIS, ANALISE ELETROQUÍMICA E ESTUDOS AVANÇADOS EM MODO DE OPERAÇÃO

CAMPINAS

2023

UNIVERSIDADE ESTADUAL DE CAMPINAS

Faculdade de Engenharia Elétrica e de Computação

BRUNO GUILHERME AGUIAR FREITAS

SUPERCAPACITOR: DEVELOPMENT OF SELF-SUPPORTED ELECTRODES, ELECTROCHEMICAL ANALYSIS AND ADVANCED STUDIES IN OPERATING REGIME

SUPERCAPACITORES: DESENVOLVIMENTO DE ELETRODOS AUTOSSUSTENTÁVEIS, ANALISE ELETROQUÍMICA E ESTUDOS AVANÇADOS EM MODO DE OPERAÇÃO

Thesis presented to the School of Electrical and Computer Engineering of the University of Campinas in partial fulfillment of the requirements for the degree of Doctor in Electrical Engineering, in the area of ELECTRICAL ENERGY (AF).

Tese apresentada à Faculdade de Engenharia Elétrica e de Computação da Universidade Estadual de Campinas como parte dos requisitos exigidos para a obtenção do título de Doutor em Engenharia Elétrica, na área de ENERGIA ELÉTRICA (AF).

Supervisor/*Orientador*: Dr. HUDSON GIOVANI ZANIN

Co-supervisor/*Coorientadora*: Dra.CRISTIANE BARBIERI RODELLA

Este trabalho corresponde à versão final da tese defendida pelo aluno Bruno Guilherme Aguiar Freitas, orientada pelo Prof. Dr. Hudson Giovani Zanin e coorientada pelo Profa. Dra. Cristiane Barbieri Rodella.

CAMPINAS

2023

Ficha catalográfica
Universidade Estadual de Campinas
Biblioteca da Área de Engenharia e Arquitetura
Rose Meire da Silva - CRB 8/5974

F884s

Freitas, Bruno Guilherme Aguiar, 1989-
Supercapacitor: development of self-supported electrodes, electrochemical analysis and advanced studies in operating regime / Bruno Guilherme Aguiar Freitas. – Campinas, SP : [s.n.], 2023.

Orientador: Hudson Giovani Zanin.
Coorientador: Cristiane Barbieri Rodella.
Tese (doutorado) – Universidade Estadual de Campinas, Faculdade de Engenharia Elétrica e de Computação.

1. Armazenamento de energia. 2. Raios X - Difração. 3. Compostos de carbono. 4. Caracterização in situ. 5. Eletroquímica - Análise. I. Zanin, Hudson Giovani, 1983-. II. Rodella, Cristiane Barbieri, 1971-. III. Universidade Estadual de Campinas. Faculdade de Engenharia Elétrica e de Computação. IV. Título.

Informações Complementares

Título em outro idioma: Supercapacitores: desenvolvimento de eletrodos autossustentáveis, analise eletroquímica e estudos avançados em modo de operação
Palavras-chave em inglês:
Supercapacitors
Energy storage
X-rays - Diffraction
Carbon compounds
In situ characterization
Electrochemistry - Analysis
Área de concentração: Energia Elétrica
Titulação: Doutor em Engenharia Elétrica
Banca examinadora:
Hudson Giovani Zanin [Orientador]
Rubens Maciel Filho
Alfredo Carlos Peterlevitz
Reinaldo Cesar
Francisca Elenice Rodrigues de Oliveira
Data de defesa: 02-03-2023
Programa de Pós-Graduação: Engenharia Elétrica

Identificação e informações acadêmicas do(a) aluno(a)
- ORCID do autor: https://orcid.org/0000-0001-5718-2931
- Currículo Lattes do autor: http://lattes.cnpq.br/3088802071323083

COMISSÃO JULGADORA – TESE DE DOUTORADO

Candidato: Bruno Guilherme Aguiar FreitasRA: 228041

Data da defesa: 02 de março de 2023

Título da Tese (inglês): Supercapacitor: development of self-supported electrodes, electrochemical analysis and advanced studies in operating regime

Título da Tese (português): Supercapacitores: desenvolvimento de eletrodos autossustentáveis, analise eletroquímica e estudos avançados em modo de operação

Prof. Dr. Hudson Giovani Zanin (Presidente)

Prof. Dr. Rubens Maciel Filho

Dr. Alfredo Carlos Peterlevitz

Dr. Reinaldo Cesar

Dra. Francisca Elenice Rodrigues de Oliveira

A Ata de Defesa, com as respectivas assinaturas dos membros da Comissão Julgadora, encontra-se no SIGA (Sistema de Fluxo de Dissertação/Tese) e na Secretaria de Pós-Graduação da Faculdade de Engenharia Elétrica e de Computação.

To my parents, I admire and love.
Aos meus pais, minha fonte admiração e amor.
Antônio D. Freitas
Maria Ducy L. A. Freitas

ACKNOWLEDGEMENTS

To all my family who, with much love, patience and support, made every effort to get me to this moment.

To my professor Hudson Giovani Zanin and Dra. Cristiane Barbieri Rodella, in addition to the great help, through teachings, tips and advice in the guidelines made possible the conclusion of this work.

To my friends Bruno Morandi, Cesar Brocchi, Chayene Anchieta, Manuel Pinzón, Rafael Vicentini, Raissa Venâncio and Willian Nunes who with their help, suggestions and conversations helped me to carry out this work.

To my researchers' colleagues, for the moments of relaxation and the great environment in which I could conduct my experiments and my studies, in addition to the great friends and people I had the honor of meeting.

To all friends and colleagues who directly or indirectly contributed to me. For the encouragement, for the constant support and for the unforgettable moments during this journey.

This study was financed in part by the Fundação de Desenvolvimento da Unicamp - FUNCAMP through agreement nº 5333.7.

“Caminante, no hay camino se hace camino al andar”
Antonio Machado.

“O binômio de Newton é tão belo como a Vênus de Milo. O que há é pouca gente para dar por isso.”
Alvaro de Campos

ABSTRACT

The ability of supercapacitors to store energy is strictly associated with the structure of the electrodes and the chemical behavior of the electrode/electrolyte interfaces. One way to increase capacitance is to use pseudocapacitive processes that can store Faradaic current through charge transfer between the electrode and the electrolyte. The first part of this work reports a multi-walled carbon nanotubes (MWCNTs) and an activated carbon (AC) composite material as an electrode for EDLCs. We investigated the specific capacitance, equivalent series resistance, working voltage window (WVW), and the specific energy and power. A high WVW of 1.4 V was verified in aqueous solution. Simultaneously, the symmetric cells were able to cycle for more than one million cycles in fast charge discharge galvanostatic tests with 93% capacitance retention. Overall, this novel electrode material exhibits a set of exciting properties, which we now tested in EDLCs. In the next work, a study was conducted to evaluate the best practices to determine the WVW for capacitive current in an absence of water splitting using complementary techniques such as cyclic voltammetry (CV), chronoamperometry (CA), and the electrochemical impedance spectroscopy (EIS). To accomplish this end, we use the composite developed in the previous work (buckypaper). The presence of residual Faradaic current is verified in the transients from the CA study, as well as the impedance changes revealed by EIS as a function of the applied voltage. Some orientations are presented to instigate the establishment of some good scientific practices concerned with the reliable characterization of supercapacitors. Finally, in the last work, we studied the damage in devices when using voltages in abusive conditions above the WVW. We report here the transient modification of electrode/electrolyte interface tracked by *operando* synchrotron X-ray diffraction and Raman spectroscopy analysis combined with *in situ* electrochemistry and theoretical calculations. We explore the lithium carbonate (Li2CO3) species formation and reversible degradation in supercapacitors prepared with nickel oxide (NiO) decorated MWCNT electrodes. A plausible reason for Li_2CO_3 formation is CO_2 evolution due to the degradation of the MWCNT electrode and Li^+ ions from the electrolyte, catalysed by NiO nanoparticles. Interestingly, the Li_2CO_3 is reversible on the full cycle cell scan in the presence of NiO, being able to explore different applications in energy storage.

Key Words: Supercapacitors; Energy storage; X-rays - Diffraction; Carbon compounds; In situ characterization; Electrochemistry - Analysis

RESUMO

A capacidade dos supercapacitores de armazenar energia está estritamente associada à estrutura dos eletrodos e ao comportamento químico das interfaces eletrodo/eletrólito. Uma forma de incrementar a capacitância é utilizar processos pseudocapacitivos que podem armazenar corrente Faradáica por meio da transferência de carga entre o eletrodo e o eletrólito. A primeira parte deste trabalho apresenta um material compósito de *multi-walled carbon nanotubes* (MWCNTs) e carvão ativado (AC) como eletrodo para EDLCs. Investigamos a capacitância específica, a resistência em série equivalente, a *working voltage window* (WVW) e a energia e potência específicas. Foi verificada uma alta WVW de 1,4 V em solução aquosa. Simultaneamente, as células simétricas foram capazes de ciclar por mais de um milhão de ciclos em testes galvanostáticos de carga e descarga rápida com 93% de retenção de capacitância. No geral, esse novo material de eletrodo exibe um conjunto de propriedades interessantes, que testamos em EDLCs. No trabalho seguinte, foi realizado um estudo para avaliar as melhores práticas para determinar a WVW para corrente capacitiva na ausência de eletrolise usando técnicas complementares como voltametria cíclica (CV), cronoamperometria (CA) e espectroscopia de impedância eletroquímica (EIS). Para isso, utilizamos o compósito desenvolvido no trabalho anterior (buckypaper). A presença de corrente Faradáica residual é verificada nos transientes do estudo CA, bem como as mudanças de impedância reveladas pelo EIS em função da tensão aplicada. São apresentadas algumas orientações objetivando proporcionar o estabelecimento de boas práticas científicas para a caracterização confiável de supercapacitores. Por fim, no último trabalho, estudamos os danos em dispositivos ao utilizar tensões em condições abusivas acima da WVW. Relatamos aqui a modificação transitória da interface eletrodo/eletrólito rastreada por difração de raios X síncrotron *operando* e análise de espectroscopia Raman combinada com eletroquímica *in situ* e cálculos teóricos. Exploramos a formação e degradação reversível de espécies de carbonato de lítio (Li_2CO_3) em supercapacitores preparados com eletrodos MWCNT decorados com óxido de níquel (NiO). Uma razão plausível para a formação de Li_2CO_3 é a evolução de CO_2 devido à degradação do eletrodo MWCNT e íons Li^+ do eletrólito, catalisada por nanopartículas de NiO. Curiosamente, o Li_2CO_3 é reversível na varredura cíclica da célula completa na presença de NiO, podendo explorar diferentes aplicações no armazenamento de energia.

Palavras-chave: Supercapacitores; Armazenamento de energia; Raios X - Difração; Compostos de carbono; Caracterização in situ; Eletroquímica - Análise

LIST OF FIGURES

LIST OF TABLES

LIST OF ABBREVIATIONS

AC	Activated Carbons
AISI	American Iron and Steel Institute
ASAP	Accelerated Surface Area and Porosimetry System
BC	Black Carbon
BET	Brunauer–Emmett–Teller
BJH	Barrett-Joyner-Halenda
BP	Buckypaper
CA	Chronoamperometry
CDC	Carbide-Derived Carbons
CE	Coulombic Efficiency
CNT	Carbon Nanotubes
CPE	Constant Phase Element
CV	Cyclic Voltammetry
CVD	Chemical Vapour Deposition
DEMS	Differential Electrochemical Mass Spectrometry
EC	Electrochemical Capacitor
EDL	Electrical Double-Layer
EDLC	Electric Double-Layer Capacitor
EES	Electrochemical Energy Storage
EIS	Electrochemical Impedance Spectroscopy
ES	Electrochemical Supercapacitors
ESR	Equivalent Series Resistance
FTIR	Fourier Transform Infrared
FWHM	Full Width at Half Maximum
GCD	Galvanostatic Charge-Discharge
GO	Graphene Oxide
HER	Hydrogen Evolution Reaction
HFIP	1,1,1,3,3,3-Hexafluoroisopropan-2-ol
ICSD	Inorganic Crystal Structure Database
IL	Ionic Liquid
LDOS	Local Density of States
LNLS	Brazilian Synchrotron Light Laboratory
LO	Longitudinal Optical
MWCNT	Multi-Walled Carbon Nanotubes
NMP	N-Methyl-2-Pyrrolidone
NMR	Nuclear Magnetic Resonance
OCP	Open Circuit Potential
OEMS	On-line Electrochemical Mass Spectrometry
OER	Oxygen Evolution Reaction
PC	Propylene Carbonate
PCVW	Practical Capacitive Voltage Window
PTFE	Polytetrafluoroethylene

PVDF	Polyvinylidene Difluoride
SC	Specific Capacitance
SDS	Sodium Dodecyl Sulfate
SEM	Scanning Electron Microscopy
SSC	Single-Step Chronoamperometry
TEM	Transmission Electron Microscopy
WISE	Water-in-Salt
WVW	Working Voltage Window
XRD	X-Ray Diffraction

CONTENTS

1. INTRODUCTION

Electric energy storage systems have received more attention in recent decades with the increasing demand for environmentally friendly and renewable energy resources increasingly needed in society [1], [2]. Among clean energy technologies, the storage and conversion of electrochemical energy, such as batteries and supercapacitors, are considered viable alternatives to meet this growing demand [3]. Batteries and supercapacitors are electrochemical devices designed to convert energy through chemical reactions into electrical energy, thus they are devices capable of storing electrical energy in the form of chemical energy [2], [4]–[7]. Supercapacitors (SCs) have lower energy density compared to batteries, but they have several other advantages such as high-power density, fast charge and discharge capacity and significantly long cycle life, presenting properties that fill a gap between batteries and electrolytic capacitors. Supercapacitors are an interesting alternative in this scenario, as we can see in the power versus energy density plot, known as the Ragone plot, Figure 1, which shows the relationship between power density and energy density for several typical electrochemical energy storage (EES) systems [8], [9].

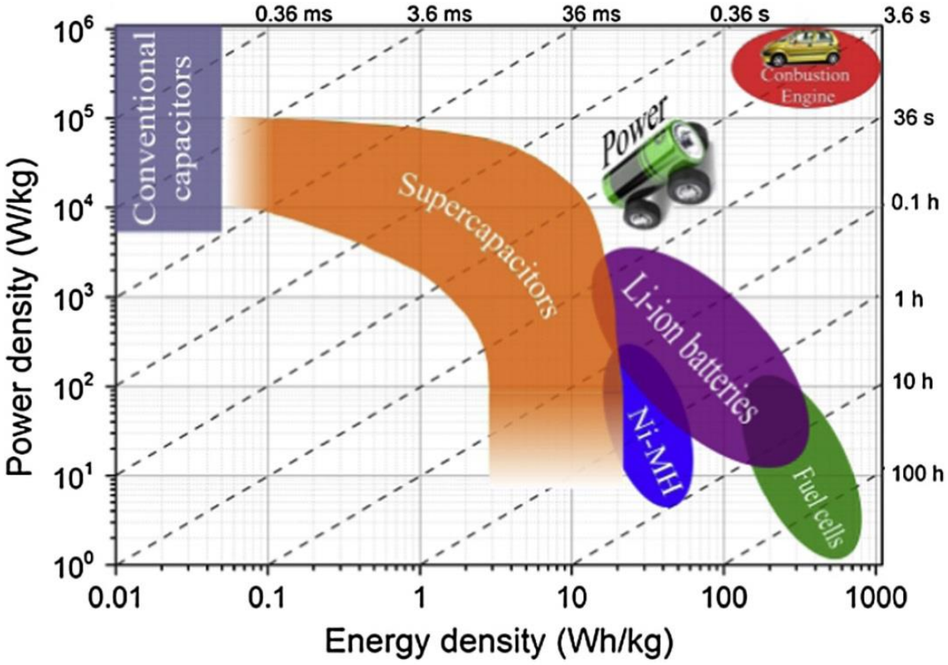

Figure 1. Ragone plot for different electrochemical energy storage systems [10].

1.1. Faradaic and Non-Faradaic Processes

Supercapacitors are commonly classified into two main types of materials that differ in the way they store charge according to the mechanism responsible for the charge storage process at the electrode/solution interface [11], [12]: (i) electrochemical electric double layer capacitors (EDLCs) based on the charge/discharge of the electric double layer formed at the electrode/electrolyte interface (non-faradaic process ideally polarized electrode) [12] that occur through electrostatic phenomena at the electrode-electrolyte interface when there is an approximation of positive and negative charges [13]. The ability to store charge through a non-Faradaic process, which does not involve charge transfer between the electrode and the electrolyte, is characteristic of the double layer phenomenon and which are called Electrochemical Double Layer Capacitors (EDLCs) [8], [14]–[17]. (ii) electrochemical pseudocapacitors (EPCs), based on pseudocapacitance arising from surface solid state redox reactions (faradaic process) [12], [18]–[21]. The Faradaic processes occur when there is oxidation and reduction between two species with different electrochemical potentials providing a flow of electrons and performing electrical work between the electrodes [13]. The phenomena that involve the transfer of charge between the electrode and the electrolyte, known as pseudocapacitive processes, occur with the transfer of charge through the double layer that generates a Faradaic current by the supercapacitor cell [8].

There are different ways to classify the mechanisms by which charge is being stored. It is necessary to observe how the material stores the charge, which can be through: a) solely by the accumulation of ions at an electrical double layer a, or b) faradaic (electron-transfer) process (Figure 1) [12].

Supercapacitors based on carbon materials are ultrafast energy storage devices such as active carbon, graphene and carbon nanotubes [22]–[36]. The ability of those devices to effectively and efficiently store energy is associated chemistry of the electrode surfaces and electrodes/electrolytes interfaces. High surface area, chemically stable electrodes and electrode/electrolyte interface knowledge are crucial for supercapacitors. Electric double layer capacitor is a type of supercapacitor that is basically based on non-faradaic absorption processes, which are quasi-instantaneous and able to produce high capacitance [37]–[41].

1.2. Decoration

In order to overcome that, faradaic reactions (redox processes similar to those on batteries) are added on the electrodes, transforming those devices on pseudocapacitors. Those faradaic reactions could be successively obtained by decoration carbon nanotubes with nanoparticles of metal oxides such as MnO_2, $NiCo_2O_4$, RuO_2, $Ni(OH)_2$, $LiCoO_2$ etc, which allowed ultrafast electron transfer on electrode/electrolyte interfaces [42]–[46].

Among the materials used as electrodes in the production of energy-storage devices are transition metal oxides that have exceptionally high specific capacity/capacitance. Several transition metal oxides appear as electrode material candidates for application in pseudocapacitors. Metal oxides onto multi-walled carbon nanotube have been used as electrode material, since its electrochemical and structural properties were described in other works and presented excellent result.

Pseudocapacitors represent a class of supercapacitors that, in addition to the capacitive properties, also store Faradaic current through charge transfer between an electrode and an electrolyte [47]. Several transition metal oxides appear as electrode material candidates for application in pseudocapacitors. Metal oxides onto multi-walled carbon nanotube have been used as electrode material, since its electrochemical and structural properties were described in other works and presented excellent results [12], [48].

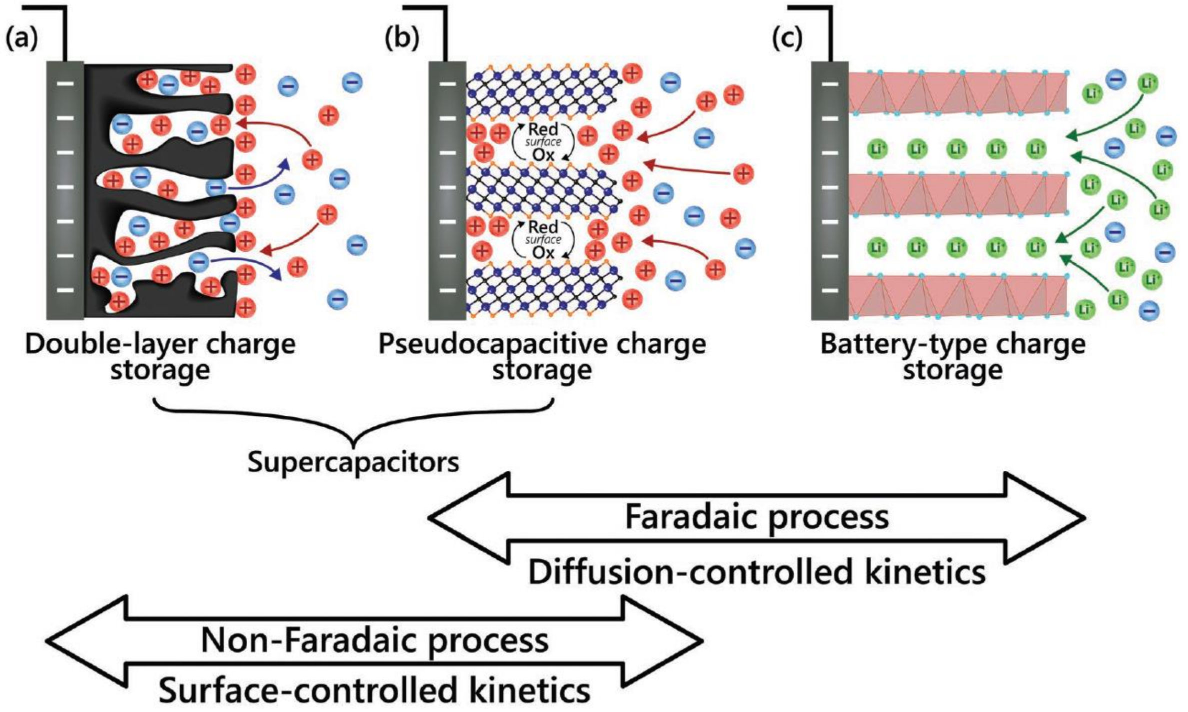

Figure 2. a) Electrical double-layer capacitive; b) Pseudocapacitive; c) Faradaic electrodes [12]

The development of pseudocapacitors has been driven by the desire to increase the specific energy of conventional EDLCs while retaining comparable the high power and long-term cyclability of EDLCs. One strategy to improve the long-term cyclability of these devices is to use metal-oxide-based materials, which is usually achieved by forming metal oxide composite materials or using asymmetrical cell designs. The construction of ‘‘asymmetric’’ devices is such that an electrode is made of faradic metal oxide combined with another non-faradic carbon electrode [49]. This approach can produce very high capacitance devices, as both double-layer and pseudocapacitance contributions are utilized, and the cyclability of the redox electrode can be improved by restricting its operating state of charge and voltage ranges. The design typically consists of a ‘‘battery-type’’ electrode (e.g., a faradic or intercalating metal oxide) and an EDLC-type electrode (high surface area carbon) as shown schematically in Figure 2 [12].

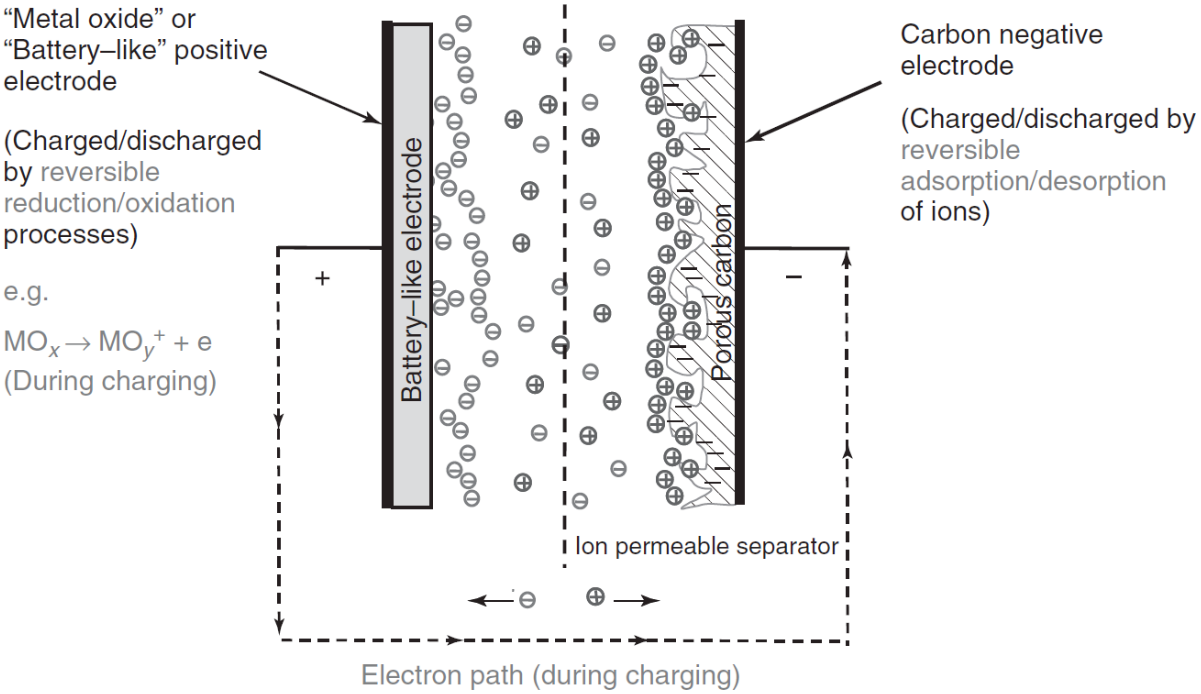

Figure 3. Schematic of a charged asymmetric electrochemical capacitor [48]

As seen previously, energy storage in an electrochemical capacitor (EC) occurs through phenomena at the interface between the electrode and the electrolyte through the polarization of charges with the application of a potential during the charging and discharging of devices [50]. These surface phenomena in a supercapacitors occur with the approximation of opposite charges at very small distances, in the order of molecular magnitude, which gives these devices a high energy storage capacity through charge polarization in large areas to high-area materials surface, such as porous carbons or by Faradaic processes involved in pseudocapacitors that can help to achieve a higher specific capacitance, examples are metal oxides, conductive polymers, etc. [1], [8], [51].

This manuscript aims to cover all the work developed during the doctoral course through which advanced studies were carried out on supercapacitors devices, such as the development of self-supported carbon-based electrodes with high surface area, in addition to a systematic electrochemical study to determine the correct working voltage window in ECs for aqueous-based systems and advanced measurements in operating mode to investigate the processes involved in the charge and discharge cycles under abusive voltage application to supercapacitors. These studies resulted in the publication of scientific articles published in recognized journals and are presented in the next three chapters of this manuscript: Chapter 2)

Carbon composite self-supported for supercapacitores; 3) Approach to identify the working voltage window for supercapacitors &; 4) Study under abusive regime of supercapacitor using *operando* XRD & Raman techniques.

2. CARBON COMPOSITE SELF-SUPPORTED FOR SUPERCAPACITORS

The low molecular mass of the active electrode component, feasible cost, chemical stability, and high capability to store charge for thousands of cycles are aspects of interest for materials used in the energy storage devices called electrochemical capacitors or supercapacitors [52]. Thus, fulfilling these requirements, some carbon allotrope materials have gained attention due to the high specific surface area, which has implications in the specific capacitance, energy, and power characteristics. The electrical double-layer capacitors (EDLCs) based on the physical charge separation process are intrinsically different from the pseudocapacitors (PCs) where intercalation and/or surface faradaic reactions significantly contribute to the overall charge-storage mechanism. In the former case, arising from the formation of an electrical double-layer (EDL) at the electrode/electrolyte interface, the charge storage process on carbon materials occurs through ionic adsorption (e.g., generations of ionic surface excess) at the walls of the accessible pores as a function of the applied electric potential or voltage [53]. Because the energy is practically stored due to the electrostatic phenomenon involving finite-sized ionic species and electrons at both sides of the interface, EDLC devices do not present expansion in the crystalline materials or pronounced redox reactions during the charge-discharge processes. Only minor contributions from the solid-state faradaic reactions occur in EDLCs due to the almost reversible redox activity involving the oxygenated surface groups. As a result, the EDLCs are highly stable, thus permitting to perform up to million cycles during its service life [54].

According to the theoretical capacitance equation presented by Helmholtz *et al.* [55], the higher the surface area so is the capacitance. However, experimental results show that although the surface area is relevant, the predicted linear relationship does not always apply [56], in part, because the finite-sized solvated ionic species from the electrolyte may not access some porous regions of the electrode material containing narrow micropores (0.2 to 2 nm). An exception is some carbide-derived carbons (CDCs), where a deep insertion of the bare ionic species into the micropores can be verified [57].

Deemed to be the best commercial material for EDLCs due to its cost-effective characteristics, activated carbons (ACs) are 3D porous materials with sp^2 hybridization, which are commonly synthesized from physical and chemical activation process from different organic precursors [58], [59]. ACs can have a very high surface area (e.g., $\approx$ 1000 to 3000 m^2 g^{-1}), and they exhibit low-moderate electronic conductivity. In this sense, at least in principle, combining AC structures with metallic conductive additives, such as black carbon (BC) or multiwalled carbon nanotubes (MWCNT), is an excellent strategy to overcome some drawbacks exhibited by ACs. As a result, the charge-storage process can be accomplished without significant ohmic losses during the electron flow across the hierarchically interconnected pores' walls, improving the overall EDLC characteristics. The traditional recipe found in the literature typically involves a mix of AC (80%) with additives (10%) and a binder (10% of PVDF or PTFE). This mixture forms a slurry that can be conveniently deposited onto a thin foil aluminum current-collector, mainly when organic electrolytes are used. Although necessary, binder species result in very poorly conducting media, thus significantly contributing to the equivalent series resistance (ESR). Moreover, binder substances adequate for EDLCs are costly and may require the use of unfriendly solvents (e.g., N-methyl-2-pyrrolidone (NMP)) with carcinogenic properties [60].

2.1. Electrolytes

As another relevant parameter of supercapacitors, electrolytes play an essential role in these devices' overall electrochemical performance. Therefore, companies are intensely interested in increasing the *working voltage window* (WVW) of different electrolyte solutions that are less harmful and not flammable to boost the specific energy density, i.e., $E = 0.5CV^2$, where C is the specific capacitance, and V is the WVW [10]. Electrolytes also influence the ESR, operating temperature, distributed capacitance, self-discharge, toxicity, and fabrication costs [61], [62].

Table 1 gathers some properties of carbon-based electrodes using different electrolytes. For instance, Li *et al*. [63] developed a free-standing composite material made of carbonized cellulose and AC using an ionic liquid (IL) as the electrolyte. This material housed in a two-electrode system yielded a WVW of 3 V and a specific capacitance of 85 F g^{-1} (0.1 A g^{-1} and BMPY/TFSI). In principle, ILs are considered promising candidates to conventional organic electrolytes since they exhibit high thermal stability and good ionic conductivity. Besides, its solvent-free characteristics permit to obtain very high WVWs (e.g., 3.5 to 4.0 V). However, a significant drawback involving ILs is their high costs compared to the organic electrolytes used in practical devices [64], [65].

Organic electrolytes may also present a potential window in the range of 2.5 to 2.8 V, resulting in high specific energies [61]. As a consequence, they have been traditionally used in several commercial devices. Gogotsi *et al*. [66] reported MWCNT (200 $m^2 g^{-1}$, 15 mg cm^{-2}, and 1.5 M $TEABF_4$) with a low specific capacitance of 18 F g^{-1} and a WVW of 2.3 V. These authors claimed the low capacitance is mainly due to the low specific surface area. In the study conducted by Jung *et al*. [67], using CNTs and reduced graphene oxide (rGO) as a free-standing composite film, and 1.0 M $TEABF_4$ + PC, the authors reported a moderate capacitance value of 110 F g^{-1} at 0.5 A g^{-1}. These authors emphasized the high-surface area of graphene of 2630 $m^2 g^{-1}$, which, in principle, might result in a theoretical capacitance of *ca*. 550 F g^{-1}.

Therefore, nanostructured carbon materials' practical response is still far from the expected theoretical values [68], [69]. In this sense, graphene still poses challenges regarding its high scalability, a more easy synthesis process, and strategies to avoid the re-stacking process caused by the π-π interactions which severely decrease the effective surface area in electrode materials [70]–[72].

For example, using a conventional carbon material, Francke *et al*. [73] reported a detailed study using commercial AC from Kuraray Chemicals Co. (Japan) with a specific surface area of 1600 $m^2 g^{-1}$. Using *1,1,1,3,3,3*-Hexafluoroisopropan-*2*-ol (HFIP) as the electrolyte, whose conductivity is higher than the mixture propylene carbonate (PC) + 1 M $TEABF_4$, these authors found a specific capacitance for the individual electrodes of 110 F g^{-1}.

To summarize, besides presenting a wider WVW, organic electrolytes' use is further due to the practical absence of corrosion processes involving the aluminum current collector materials. Nonetheless, issues related to high cost, toxicity, flammability, volatility, and safety concerns remain. Moreover, a complex purification process is necessary for removing impurities, such as water, which, besides safety concerns, may lead to fast electrolyte degradation and accelerated self-discharge processes [61], [74], [75]. From these reasons, since 1997, the study of aqueous-based electrolytes has become very exciting to obtain more friendly conditions for the use and fabrication of SCs.

A significant issue regarding the aqueous electrolytes is the low WVW of *ca*. 1.0 V. Due to thermodynamic and kinetic factors, the water-splitting reaction commonly occurs at low cell voltages. Therefore, the great challenge involving these electrolytes is to increase the WVW to improve the overall device performance characteristics. Different aspects regarding the water-based electrolytes were discussed by Beguin *et al*. [76], who showed that for neutral solutions (e.g., Li_2SO_4 and Na_2SO_4), the WVW is higher when compared to the H_2SO_4 and KOH solutions. However, H_2SO_4 solutions are widely used in the literature reports [71]. As reported by Zhong *et al*. [61], H_2SO_4 solutions are exciting due to its higher ionic conductivity that leads to low ESR values. For instance, Deng *et al*. [77] developed a CNT/holey graphene binder-free electrode (1.0 mg), which in 0.5 M H_2SO_4 presented a specific capacitance for the individual electrodes of 268 F g^{-1} at 0.25 A g^{-1}. Kaempgen *et al*. [78] developed a single-walled CNT printed thin-film supercapacitor and presented a comparative study involving several electrolyte species. Using a 1.0 M H_2SO_4 solution, the highest achieved capacitance by these authors was 120 F g^{-1} at 1.0 A g^{-1}. This value corresponded to an real capacitance of 0.25 F cm^{-2}. In the case of alkaline solutions, Chang *et al*. [79], using a biomass-derived carbon composite containing rGO (137 m^2 g^{-1} and 0.95 mg), reported a specific capacitance for the individual electrodes of 216 F g^{-1} at 0.1 A g^{-1} (6.0 M KOH).

It is crucial to emphasize that the electrode active mass strongly influences the capacitance values [80]. The former should be higher than 10 mg with a lower capacitance limit of 0.25 F. Likewise, as stated by Gogotski and Simon [81], commercial electrodes traditionally possess 100 to 200 μm of a thickness corresponding to a mass loading of ≈ 10 mg cm^{-2}. It is important to note that the possibility to extrapolate the electrode performance considering a low thickness of ≈ 1 μm for practical applications is meaningless. In this sense, Peng *et al*. [58], [82] presented a carbon-based material derived from the biomass-derived carbon obtained from tea leaves. For a high specific surface area of 2841 m^2 g^{-1} and an electrode mass of 8 mg, these authors found a high value of 330 F g^{-1} in 2.0 M KOH for the individual electrode capacitance. However, it is worth mentioning that real symmetric devices commonly exhibit ¼ of the specific capacitance verified for individual electrodes measured in three-electrode cells.

From the above considerations, we report in this work binder-free and self-supported MWCNT:AC buckypaper electrodes in an aqueous electrolyte where no metallic current collector was used to avoid corrosion issues. In this sense, we also presented an innovative, robust weld technology capable of delivering secure and facile fastening of metallic connectors to the free-standing electrode, whereas guaranteeing high electronic contact. The buckypaper was synthesized using several MWCNT:AC ratios aiming to provide the best electrode mass-loading conditions that resemble commercial devices. Since the porous buckypaper material has several voids between the carbon particles, we applied a hot-pressing treatment to improve the composite’s overall conductivity. A rigorous experimental procedure was reported to correctly identify the capacitive voltage range in the absence of water-splitting.

Table 1. Carbon-based free-standing electrodes and their electrochemical characteristics.

Electrode material	**SSA (m^2 g^{-1})**	**Electrolyte (mol l^{-1})**	**C_g (F g^{-1}) C_a (mF cm^{-2}) C_v (F cm^{-3})**	**Mass loading (µg cm^{-2})**	**Electrode thickness (µm)**	**Voltage window (V)**	**Test conditions**	**Ref.**
Graphene-CNT composite	-	1 M $TEABF_4/PC$	110 (g) 78 (g)	-	-	3	0.5 Ag $^{-1}$ 5 A g^{-1}	[67]
Kuraray AC	1600	1 M $TEABF_4$/HFIP	110 (g)	-	200	-	1 mV s^{-1} (3el)	[73]
Graphene//MnO_2 /grapene		Na_2SO_4 (1)	31 (g)			2	500 mA g^{-1} (2el)	[83]
MWCNT	200	$TEABF_4$ (1.5)	18 (g)	15000	-	2.3	5 mA cm^{-2} (2el)	[66]
SWCNT / PANI		H_2SO_4 (1)	55 (g)	-	0.120	0.8	2.6 A g^{-1}	[84]
PANI@CNT		H_2SO_4/PVA gel	346.6 (g)	-	-	0.8	10 mV s^{-1}	[85]
Graphene/CNT	-	H_2SO_4 (1)	120 (g)	-	-	0.6	CV	[86]
CNT Activated CNT NMCNT	218 778 200	H_2SO_4 (1)	48.4 151.7 190.8	-	-	1	5 mV s^{-1}	[87]
SWCNT	-	H_2SO_4 (1) PVA / H_3PO_4	120 (g) 110 (g)	-	20-40	1	1 mA mg^{-1}	[78]
rGO–CNT	240	KOH (6)	250 (v)	13000	-	1.2	1 A g^{-1}	[88]
AC/CNT/rGO	913.4	$LiClO_4$ (1)	101 (g)	0.453	-	3	0.2 A g^{-1}	[89]
Bacterial cellulose - rGO/CNF	137	KOH (6)	216 (g)	Mass – 0.95 mg	1200	1	1 A g^{-1}	[79]
Submicron CFs	1005	Na_2SO_4 (1)	47 (g)	-	-	1.3	1 A g^{-1}	[90]
Submicron activated CFs	-	KOH (6)	344 (g)	1800		1	10 mV s^{-1}	[91]

Carbon monolith	770	EMITFSI	75 (g)	-	-	2.5	10 mV s^{-1}	[92]
Lithographically AC	1636	H_2SO_4 (1)	325	-	~1.5	0.6	45 A g^{-1}	[93]
AC/graphene	2070	H_2SO_4 (1)	186 (g)	-	-	1.1	0.5 A g^{-1} (3el)	[94]
AC	1137	LiOH (1)	204 (g)	-	600	0.8	1 A g^{-1}	[95]
CNT/holey graphene	-	H_2SO_4 (0.5)	268 (g)	1000	-	0.7	0.25 A g^{-1} (3el)	[77]
AC	2562	Na_2SO_4 (1)	294.3 (g)	20000	-	1.79	0. 5 A g^{-1} (2el)	[96]
CNT fiber	-	H_2SO_4-PVA	4.28 (a)	-	-	0.8	50 mV s^{-1}	[97]
Self-stacked solvated graphene film	-	H_2SO_4 (1)	215 (g)	45	-	1	0.1 A g^{-1} (2el)	[98]
Flower-like hierarchical porous carbon	761.5	Na_2SO_4 (1)	35.6 (v)	-	-	1.8	-	[99]
Laser-scribed graphene	1520	NEt_4–BF_4 in ACN (1)	265 (g) 4.82 (a)	-	< 100	3	-	[100]
		$EMIMBF_4$	276 (g) 5.02 (a)			4		

2.2. Experimental Section

2.2.1. Materials

Model Ctube-120 MWCNT (95% purity, the diameter of 10 to 40 nm, and length of 1 to 40 μm) were purchased from CNT Co. Ltd. (Korea) while model YP-50F AC (1692 $m^2 g^{-1}$ and 0.3 g mL^{-1}) was purchased from Kuraray Co. Ltd. (Japan). The other “purum” p.a. chemicals were furnished by Synth® (Brazil) and used without further purifications.

2.2.2. Preparation of the MWCNT:AC buckypaper electrodes

Buckypaper electrodes were synthesized using the MWCNT:AC mass ratios of 1:0, 1:1, 1:2, and 1:3, henceforth referred to as $b_{1:0}$, $b_{1:1}$, $b_{1:2}$, and $b_{1:3}$, respectively. Mass values are specified in Table 2.

Table 2. Buckypaper masses for the different electrode samples.

Sample	**MWCNT:AC ratio**	**MWCNT (wt.%)**	**AC (wt.%)**	**Electrode mass (mg)**
$b_{1:0}$	1:0	100.0	0.0	33.3
$b_{1:1}$	1:1	50.0	50.0	29.1
$b_{1:2}$	1:2	33.3	66.7	27.5
$b_{1:3}$	1:3	25.0	75.0	29.3

The materials were dispersed in deionized water for each sample using a 0.5 wt.% sodium dodecyl sulfate (SDS) solution. The SDS was added to increase the interaction of the MWCNT with water. MWCNTs are hydrophobic, making buckypaper with them hard and inefficient in the production in aqueous media (water is the cheapest, low toxic and easy handle solvent). We added SDS, because it has polar and nonpolar parts, which means hydrophilic and hydrophobic parts in its molecule binding to water and MWCNT make them join together. Afterward, the suspension was sonicated using an ultrasound tip probe from

Ultronique® (80 W and 30 min) to obtain homogenous dispersion of carbons. Each dispersion was then filtered under a vacuum using a 0.22-μm PTFE porous membrane (Millipore®) during ≈ 2 h. The residue of SDS was removed after a copious washing process using deionized water. The carbon-based layers formed after filtration were peeled off from the PTFE membrane. After the preparation of buckypaper, we washed then carefully and many times and dried at room temperature overnight. The hot-pressing method was applied to improve the physical/electrical contact between the carbon material particles. The treatment was accomplished at 100°C and 10 rpm using a hot-rolling press (TOB-DR-H150). For each sample, the procedure was repeated twice. Lastly, the electrodes with appropriate diameters to fit the model CR2032 coin cell were punched out of the buckypaper for the cell assembling process [101], [102].

2.2.3. Materials characterization

Surface morphologies were examined by scanning electron microscopy (SEM) using a model S-3400N equipment from Hitachi. Structural micrographs were performed by JEOL JEM 2100 LaB_6. X-ray diffraction was performed by Philips Analytical X-Ray diffractometer with Cu-Kα radiation ($\lambda = 1.5418$ Å) in a Bragg–Brentano θ/θ configuration (Goniometer PW3050/10) for investigation on the crystalline of nanoparticles. The diffraction patterns were collected with steps of 0.01° and accumulation time of 0.6 s per step within the range of 10°- 60° (2θ). Raman spectra were taken in a Renishaw inVia spectrometer with a 633-nm excitation wavelength (50% of laser intensity, 10 accumulations, and 5× objective lens). Notably, the authors compared the first and last intensity ratios (I_D/I_G) of Raman bands to ensure that the incoming laser radiation did not damage the samples. The BET and BJH analyses comprising the specific surface area and pore size distribution, respectively, of the carbon materials were accomplished from the physical adsorption technique using N_2 at 77 K with a model ASAP 2010 equipment from Micromeritics®. Firstly, samples were preconditioned in a dry oven at 70°C utilizing a vacuum for 12 h. Afterward, the samples were heated to 120°C for 6 h until the desired isobaric condition ($P = 2$ μm Hg).

2.2.4. Electrochemical characterization using a symmetric coin cell

For the electrochemical tests, the buckypaper electrodes and the porous separator (cellulosic membrane) housed in the symmetric CR2032 coin cell were soaked with 60 μL of a 1.0 M Li_2SO_4 solution (aqueous electrolyte).

An experimental approach to correctly identify the capacitive voltage window in SCs – A significant issue regarding SCs is concerned with the apparent (incorrect) evaluation of the capacitive voltage window due to the contribution to the overall current of a small faradaic current due to the solvent decomposition (e.g., water-splitting). The situation is more dramatic for techniques involving the rapid application of the voltage or current increments, as are the CV and GCD techniques. Therefore, these techniques must be carefully applied to identify the capacitive voltage interval correctly. In this sense, the capacitive voltage window was determined in the present work by combining the CV and single-step chronoamperometry (SSC) experiments. Firstly, CVs were recorded at a low scan rate of 5 mV s^{-1} since this condition permits identifying the presence of an irreversible faradaic process close to the vertex voltages. The cell voltage was progressively increased from the OCP in steps of 0.1 V until detecting a voltammetric ‘current tail.’ Afterward, an SSC experiment was carried out for that voltage to verify if the transient current becomes negligible after a brief interval of c.a. 150 s. If an almost stationary (faradaic) current is confirmed, the voltage window is reduced in small voltage steps until a negligible background current is obtained. In addition, the impedance spectra were recorded at different d.c. voltages and used to discriminate the correct capacitive voltage window in the absence of water-splitting, i.e., the almost-vertical straight line verified in the complex-plane plot at low frequencies for a pure capacitive behavior becomes a poorly developed semicircle in the presence of water electrolysis due to the charge-transfer resistance occurring in parallel to the electrical double-layer capacitance.

Cyclic voltammetry (CV), galvanostatic charge-discharge (GCD), single-step chronoamperometry (SSC), and electrochemical impedance spectroscopy (EIS) experiments were accomplished using a model BCS-810 cycler equipment from Bio-logic Science Instruments®. For the different fixed (d.c.) voltages, the EIS findings were registered for the frequency range of 10 kHz to 10 mHz by applying a small sinusoidal signal of 10 mV (peak-to-peak) to ensure linearity on the impedance response.

After the correct determination of the WVW as mentioned above, CV and GCD experiments were performed at more realistic dynamic conditions of 100 mV s^{-1} and 1.0 A g^{-1}, respectively, to evaluate the carbon-based symmetric coin cell's overall performance. Cyclability tests were performed in the best samples for 1 mi cycles at 2 A g^{-1}.

2.3. Results and Discussion

2.3.1. Materials characterization

2.3.1.1. SEM and TEM images

Figure 4 shows the SEM micrographs of the buckypaper samples. According to Figure 4 (a), one can see the material morphology's alteration upon increasing the AC mass ratio. As a template, Figure 4 (a-c) depicts the buckypaper synthesized using only MWCNT ($b_{1:0}$). The illustrated morphology of the $b_{1:0}$ sample conveys the advantage of the MWCNT entangled a spaghetti-like distribution, which provides a freestanding, mechanically robust, and flexible carbon sheet. MWCNT presented diameters ranging from 20 to 40 nm and an average length of 40 µm by the SEM micrographs (Figure 4 (d)). Analogously, by increasing the AC mass ratio, a morphology with more flakes is evident, as shown in Figure 4 (e-p). It is worth noting that the sample with the highest AC mass ratio ($b_{1:3}$) corresponds to the freestanding material that still can attain its remarkable mechanical properties. According to Figure 4 (m-p), in the case of the $b_{1:3}$ sample, one can observe that AC is homogeneously dispersed throughout the sample. In contrast, the MWCNT involves the AC flakes, thus creating a highly conducting network. As a result, this material sample is expected to provide good electron transport during the rapid charge-discharge processes (Please see further discussion).

Figure 5 (a,b) shows structural micrographs of the MWCNT and AC samples, respectively. TEM confirms that MWCNTs have diameters ranging from 20 to 30 nm with turbostratic structure and negligible internal pores i.e., close caps (Please see detail in hand left size of tube Figure 2 (a) or Figure 2 (h) in reference [101] for instance). At the same time, according to the different contrasts in the images, the AC sample showed a not well crystalline material with macro- (> 50 nm), meso- (2–50 nm), and micro-pores (< 2 nm) indicated with green, yellow and blue colors respectively.

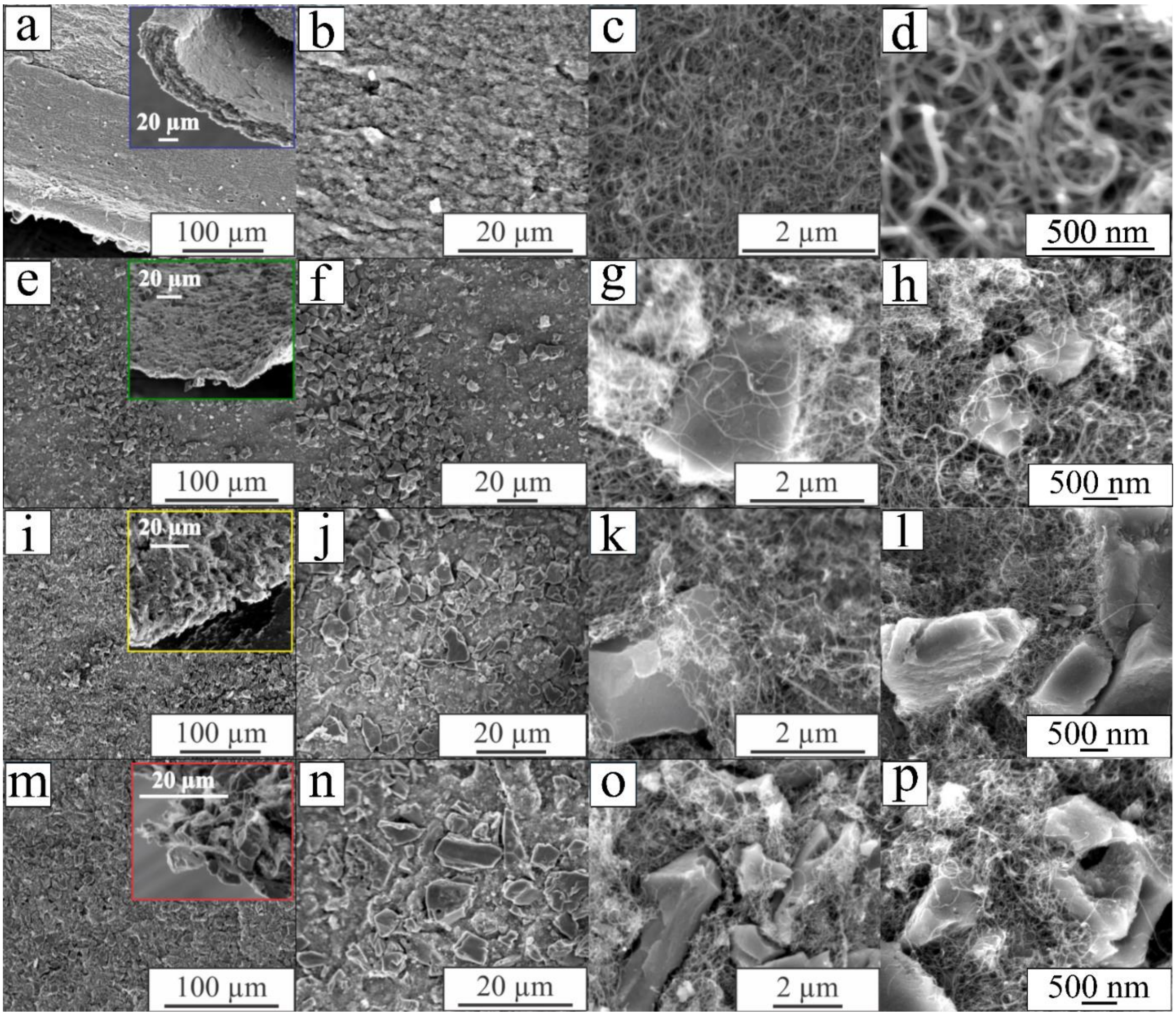

Figure 4. SEM micrographs of the different buckypaper samples: (a-d), $b_{1:0}$; (e-h), $b_{1:1}$; (i-l), $b_{1:2}$; (m-p), $b_{1:3}$.

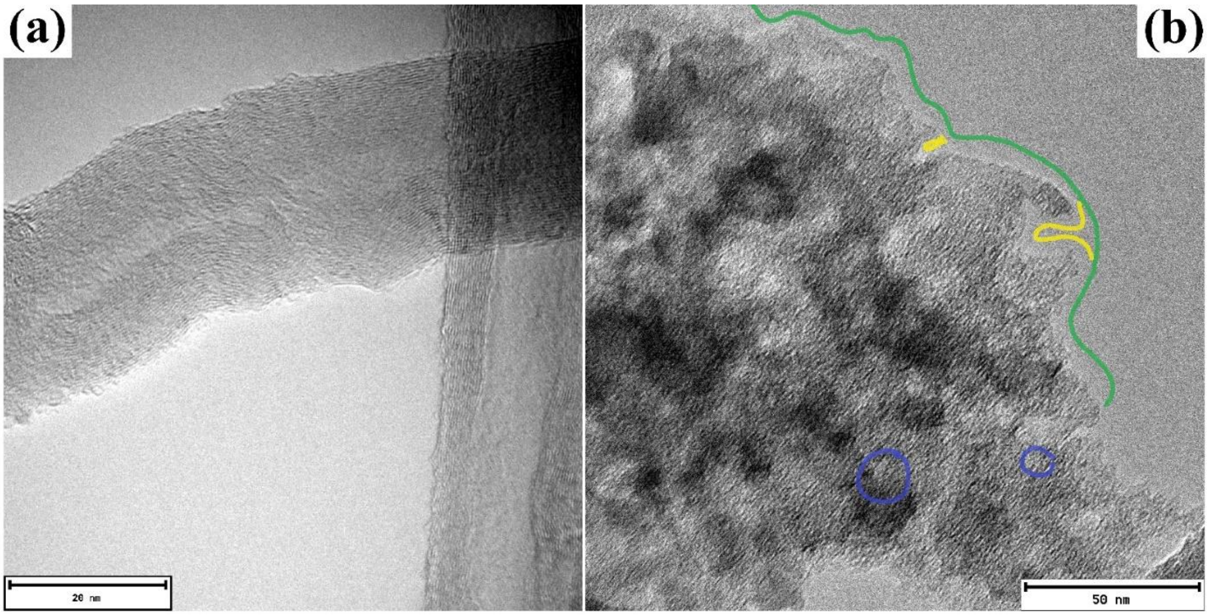

Figure 5. TEM images were obtained from the **(a)** MWCNT and **(b)** AC carbon materials. We highlighted in green an example of macropore, yellow of mesopores and blue of micropores.

2.3.1.2. Raman Spectra

Raman spectroscopy was used to investigate the chemical and structural properties of the carbon-based samples. The findings are shown in Figure 6 (a-d). Based on signal deconvolution of the MWCNT spectrum presented in Figure 6 (b), the findings evidenced the prominent D, G, D’, and 2D bands at 1326 cm$^{–1}$, 1580 cm$^{–1}$, 1612 cm$^{–1}$, and 2649 cm$^{–1}$, respectively. Besides, two less intense peaks at ~1139 cm$^{–1}$ (D*) and ~1477 cm$^{–1}$ (D$^{\#}$) were also observed. The AC Raman spectrum that is showed in Figure 6 (c) evidenced two main D and G peaks at 1321 cm$^{–1}$ and 1600 cm$^{–1}$, respectively. Three less intense peaks denoted as D* (1171 cm$^{–1}$), D$^{\#}$ (1506 cm$^{–1}$), and 2D (2649cm$^{–1}$) were also verified for the AC sample. Please note that G ranges from 1580 to 1600cm^{-1}, D* ranges from 1139 to 1171 cm^{-1} and D$^{\#}$ ranges from 1477 to 1506 for different carbon forms. All this discrepancy of band position is related to the crystallinity of the materials. Our analysis revealed that the Raman spectrum of the composite samples containing MWCNT and AC is constituted of the materials’ individual responses.

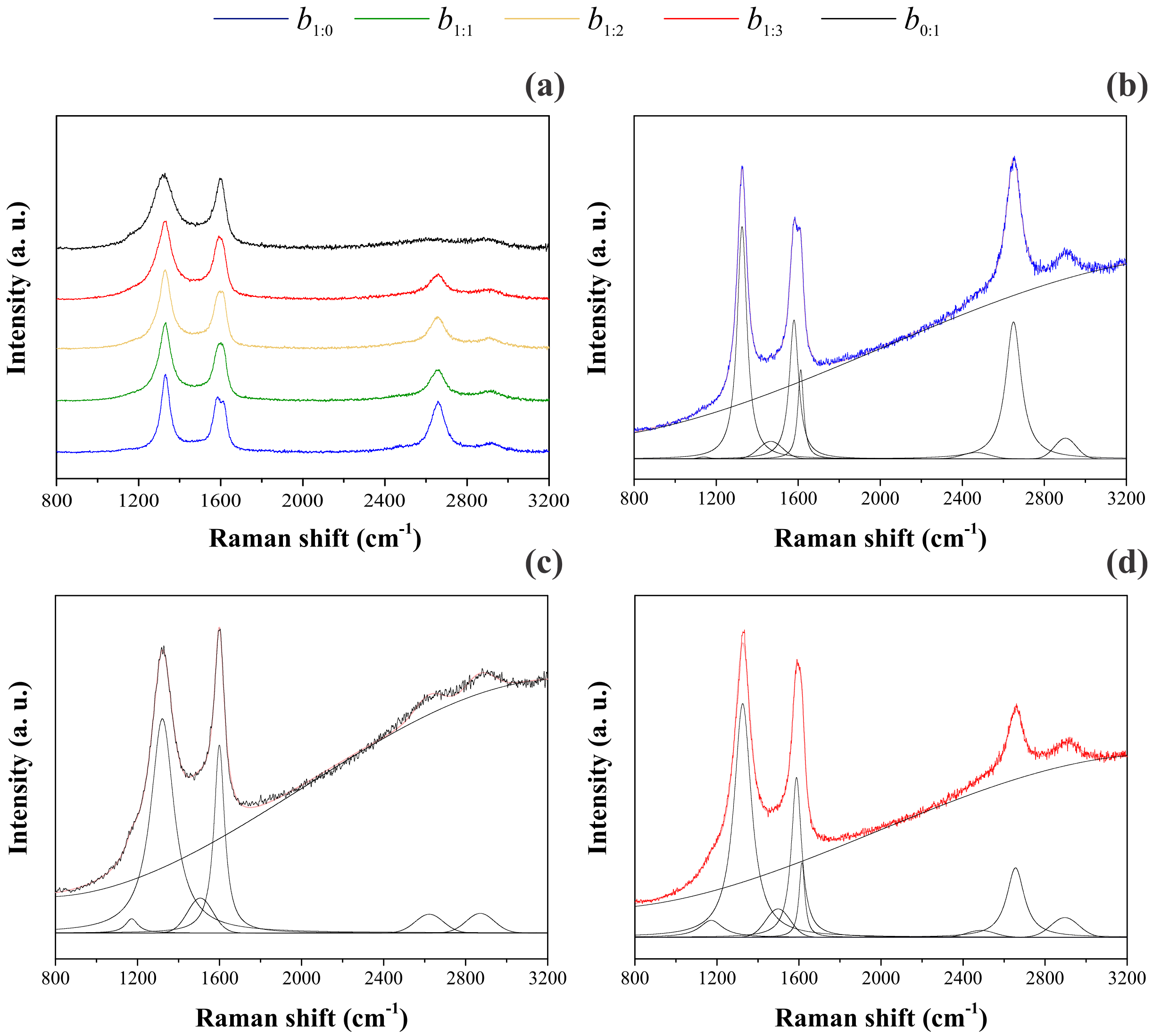

Figure 6. Raman spectra of the carbon-based composites (a) and the individual components ((b) MWCNT & (c) AC). The $b_{1:3}$ composite is also shown in (d).

The G-band, also reported as E_{2g}, is centered in 1582 to 1600 cm^{-1}. This band is originated by double degenerate vibrational modes of iLO and iTO phonon branches, crossing at the Γ point in the first Brillouin zone, according to the theoretical band model proposed for the graphene materials [103]–[105]. On the other hand, the D-band corresponds to the high-frequency E_{2g} phonon at the Γ point. In this case, the band appearance requires a defect for its activation to account for the breathing modes of the six-atom rings exhibited by the graphene layers [106]. These structural defects are generally concentrated at the crystallite edges or boundaries [107], [108]. Again, the D-band appears when the lattice vibrational (Raman-inactive modes) presents a symmetry-breaking defect, affecting the selection rules ($q = 0$). D-band is double resonant LO phonons [106]. It is dispersive with excitation wavelength due to Kohn anomaly around the K point, i.e., its position depends on the laser excitation wavelength. D* band is related to amorphous-like carbons (e.g., defect-rich short carbon layers). The $D^{\#}$ band is assigned to oxygen functional groups onto carbon surface such as C-O, C=O, COO^- as reported by us elsewhere [109]–[113]. Therefore, we refer to $D^{\#}$ as Carbon with functional oxygen group band, CfO. The 2D-band is a harmonic of the D signal, but it does not need a defect to be active, which means that phonon is not scattered during the double resonance process [114].

Table 3 gathers the Raman's dependency of the relative intensities as a function of the AC mass ratio used in the buckypaper samples.

Table 3. Effect of the AC mass ratio in the different samples on the Raman bands' relative intensity.

Sample	**Relative intensity of Raman bands**				
	(I_G/I_D)	**($I_{D'}/I_D$)**	**(I_{2D}/I_D)**	**(I_{CfO}/I_G)**	**(I_{CfO})/I_D**
$b_{1:0}$	0.63	0.44	0.64	0.12	0.07
$b_{1:1}$	0.61	0.43	0.4	0.20	0.12
$b_{1:2}$	0.6	0.42	0.39	0.17	0.10
$b_{1:3}$	0.45	0.32	0.3	0.18	0.12

Table 3 shows I_G/I_D, $I_{D'}/I_D$, I_{2D}/I_D, I_{CfO}/I_G, I_{CfO}/I_D intensities ratios. With AC incorporation, the I_G/I_D & I_{2D}/I_D decrease, suggesting that carbon composite lose crystallinity, which agrees with TEM data. To support this claim, Figure A.1 shows the X-ray diffraction pattern of carbon materials. The peaks set correspond to crystalline phases of Carbon, the well-organized graphene hexagonal structuring of spatial group *P63/mmc* (PDF# 01-089-7213) [115]; the two peaks can be indexed as the lattice planes (002) and (101) in 26.5° and 44.5° as 2θ, respectively. It is evident that with AC incorporation, those peaks broadening like a band. We also observe that I_{CfO} and I_D or I_G ratio intensity increase by adding AC. That oxygen functional groups are essential to improve the wettability of MWCNT:AC electrode at first cycles. AC's introduction also promotes improvement regarding the specific surface area due to its highly porous characteristics.

2.3.1.3. Brunauer–Emmett–Teller (BET) analysis

Therefore, an excellent experimental strategy involves the right balance between the intrinsic properties of the individual carbon materials used in the composite samples. From these considerations, BET analyses were accomplished for the different samples. The isotherms are presented in Figure 7, while Table 4 gathers the specific surface area values.

Table 4. Specific surface area (SSA) as a function of the AC mass ratio in the carbon composites.

Sample	$b_{1:0}$	$b_{1:1}$	$b_{1:2}$	$b_{1:3}$	$b_{0:1}$
SSA/m^2 g^{-1}	147	718	988	1117	1692

Figure 7 (a – d) presents the isotherms of the adsorbed volume of N_2 as a function of relative pressures ($P\ P_0^{-1}$). The large adsorbed volumes are typical from meso- and micropores materials. As can be seen, the data in Table 4 indicates that SSA scaled to the high AC mass ratio due to micropores' influence. This proposal is sustained by the pronounced slope verified in the BET plots in low relative pressure (Please see B point in Figure 2 II reference [116]).

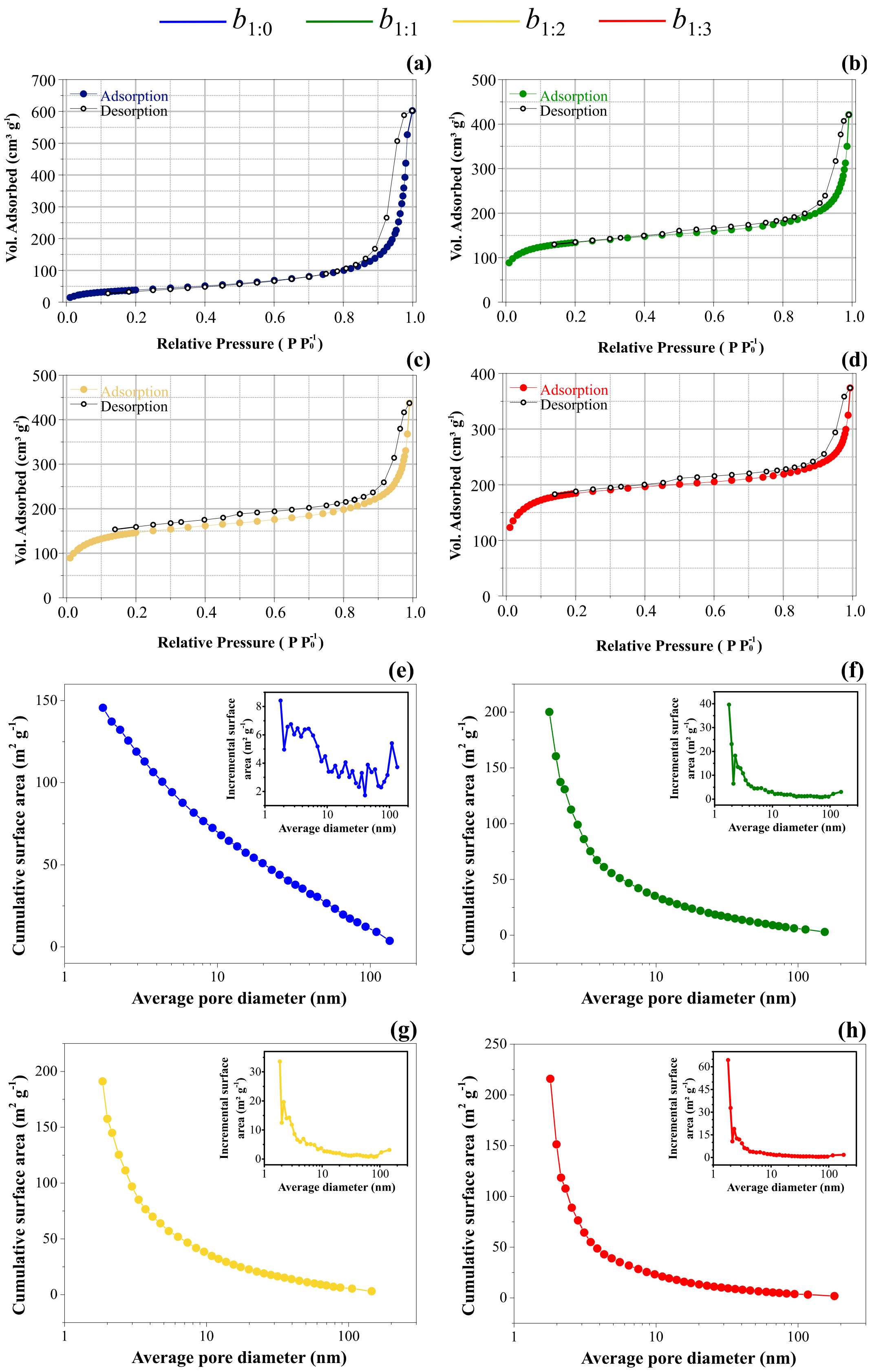

Figure 7. (a-d) The nitrogen isotherms and (e-h) pore size distribution obtained for the different carbon-based samples used in the BET analysis. (a & e) $b_{1:0}$, (b & f) $b_{1:1}$, (c & g) $b_{1:2}$, and (d & h) $b_{1:3}$.

As one may see in Figure 7 (e-f), MWCNT bucky paper has mesopores predominantly with almost homogeneous distribution from 1nm to 100nm, i.e., it is almost a straight-line the accumulative surface area with pores distribution (Please see Figure 7(e)). Figure 7 (f-h) shows that the incorporation of activated Carbon in buckypaper changes the uniform pores-size distribution scenario, and one may observe exponential decay on the pores size contribution concerning the accumulative surface area. The main reason is that activated Carbon has mainly micropores which have a higher contribution to the surface area i.e., micropores and smaller size mesopores contribute more to the accumulative surface area, and with AC incorporation, there are more present in these samples.

2.3.2. Electrochemical characterization of the composite buckypaper electrodes

Figure 8 presents the effect of the MWCNT:AC mass ratio on the electrochemical behavior of the buckypaper electrodes. The electrochemical findings were obtained using a symmetric coin cell filled with 1.0 mol dm^{-3} Li_2SO_4 aqueous solutions. Figure 8 reveals the value of 1.4 V for the working voltage window (WVW) determined using a low scan rate of 5 mV s^{-1} to ensure the absence of the parasitic water-splitting reaction during the capacitive process (Please see data in Table A.1). We performed additional experiments using the SSC technique to hold the maximum cell voltage referring to the WVW while the corresponding current transient was measured. This procedure permitted us to discriminate the physicochemical origin of the background/residual current. While a capacitive current must fade away after a brief time interval, the presence of a faradaic current due to water-splitting results in a current plateau according to the electrolysis Faraday`s law. It is worth noting that the use of high scan rates (e.g., ≈ 50–100 mV s^{-1}) is not appropriate for WVW determination since, due to its irreversible kinetics, the water decomposition reaction can be not clearly identified by a ‘current tail’ in the CV profiles, thus leading to unsatisfactory results. Therefore, low scan rates are mandatory for the correct determination of the capacitive voltage range in SCs. Unfortunately, these precautions are not considered in several literature reports, resulting in very high (incorrect) WVW values.

From these considerations, we adopted in the present work a set of experiments using the CV, SSC, and EIS techniques to determine the WVW (Please, see the Experimental section). It was generally verified almost the same residual (background) current after 25 s for the several voltages applied using the SSC technique (Please see Figure 8 (b) and Figure A.2-A.6). From the theoretical viewpoint, after applying a step-voltage function, the transient (capacitive) current must obey the relationship $I = I_0 \times \exp(-t/\tau)$, where I_0 is the initial current at $t = 0$ and τ is the system's time constant. Thus, when the I/I_0 ratio is inferior to 0.01, representing a 99% decrease in the measured current, one can assert that the capacitive current is practically negligible for the corresponding time interval. Therefore, the resulting 'almost stationary' current measured for the interval (e.g., $t \geq 25$ s, depending on the intrinsic capacitance and resistance) in the SSC experiment is only due to the parasitic water-splitting reaction. In this sense, the transient response's behavior comprises a rigorous criterion for the correct identification of the capacitive voltage window in SCs.

The SSC experimental findings showed in Figure 8 (b) corroborate the nearly perfect rectangular mirror-like voltammetric profiles expected for EDLCs (Please see Figure 8 (a)). The almost vertical straight lines verified in the low-frequency range of the complex-plane plots (see Figure 8 (c)) and the almost perfect triangular GCD profile comprise the behavior theoretically predicted for real EDLCs (see Figure 8 (d)). GCD data at different current densities were also performed and the corresponding findings are presented in Figure A.2.

Regarding the EIS findings, it is worth mentioning that a small semicircle in the high-frequency range is due to the '*distributed capacitance*' phenomenon originated from the electrochemically active narrow pores. Unfortunately, this well-known porous impedance behavior is commonly misinterpreted as caused by false mass-transport limitations and unrealistic ohmic contacts between the electrode/current collector solid interface. According to the robust theoretical EIS model proposed by Bisquert *et al*. [117], the impedance behavior verified in Figure 8 (c) denounces an anomalous charge transport in the solid and liquid phases in intimate contact caused by the porous nature of the electrode material. In these cases, the central information for SCs can be extracted from the low-frequency response that yields the electrical double-layer capacitance (C_{edl}) and the high-frequency limit (e.g., 10 kHz) where the ESR value is accurately determined.

It was verified that the substitution of MWCNT by the AC particles does not affect the WVW of 1.4 V observed for the buckypaper electrodes. Since this value is higher than the

1.23 V, i.e., the theoretical prediction according to thermodynamics under ‘standard conditions’ (e.g., $p(O_2)$ and $p(H_2)$ partial pressures of 1.0 bar), we can assert from the kinetic viewpoint that the carbon materials used in the buckypaper electrodes exhibited high overpotentials (e.g., electrochemical activation energies) for the water-splitting reaction. We also observed that the incorporation of AC particles in the buckypaper electrodes increases the specific capacitance (Please see Table 5). It was verified large increases of ≈ 50% and 75% for the $b_{1:1}$ and $b_{1:3}$ electrodes, respectively. Importantly, for AC loadings higher than 75%, the buckypaper does not form nor maintains its good mechanical characteristics such as freestanding and flexible properties.

Considering that the $b_{1:3}$ electrode has the highest specific capacitance and the maximum specific surface area (SSA) (Please see Figure 7 and Table 4), we can propose that the charge-storage process roughly scales SSA. In this sense, considering as a benchmark for common carbon-based electrodes an area capacitance of 5 $\mu F\ cm^{-2}$ (or 0.05 $F\ m^{-2}$) [118], we found for our data a corresponding specific capacitance of ≈ 50 $F\ g^{-1}$ for the $b_{1:3}$ electrode. After normalizing the pertinent quantity (e.g., 50 $F\ g^{-1}$/0.05 $F\ m^{-2}$), one obtains an SSA value of 1000 $m^2\ g^{-1}$. Supported by the BET analysis (ASAP measurements), this calculation indicates that almost the entire specific surface area of 1170 $m^2\ g^{-1}$ of the porous carbon-based electrode is electrochemically active) charge-storage process. From the theoretical viewpoint, these findings support the presence of accessible narrow pores interconnected with the meso- and macro-pores that provides the ionic species for the rapid charge-discharge processes.

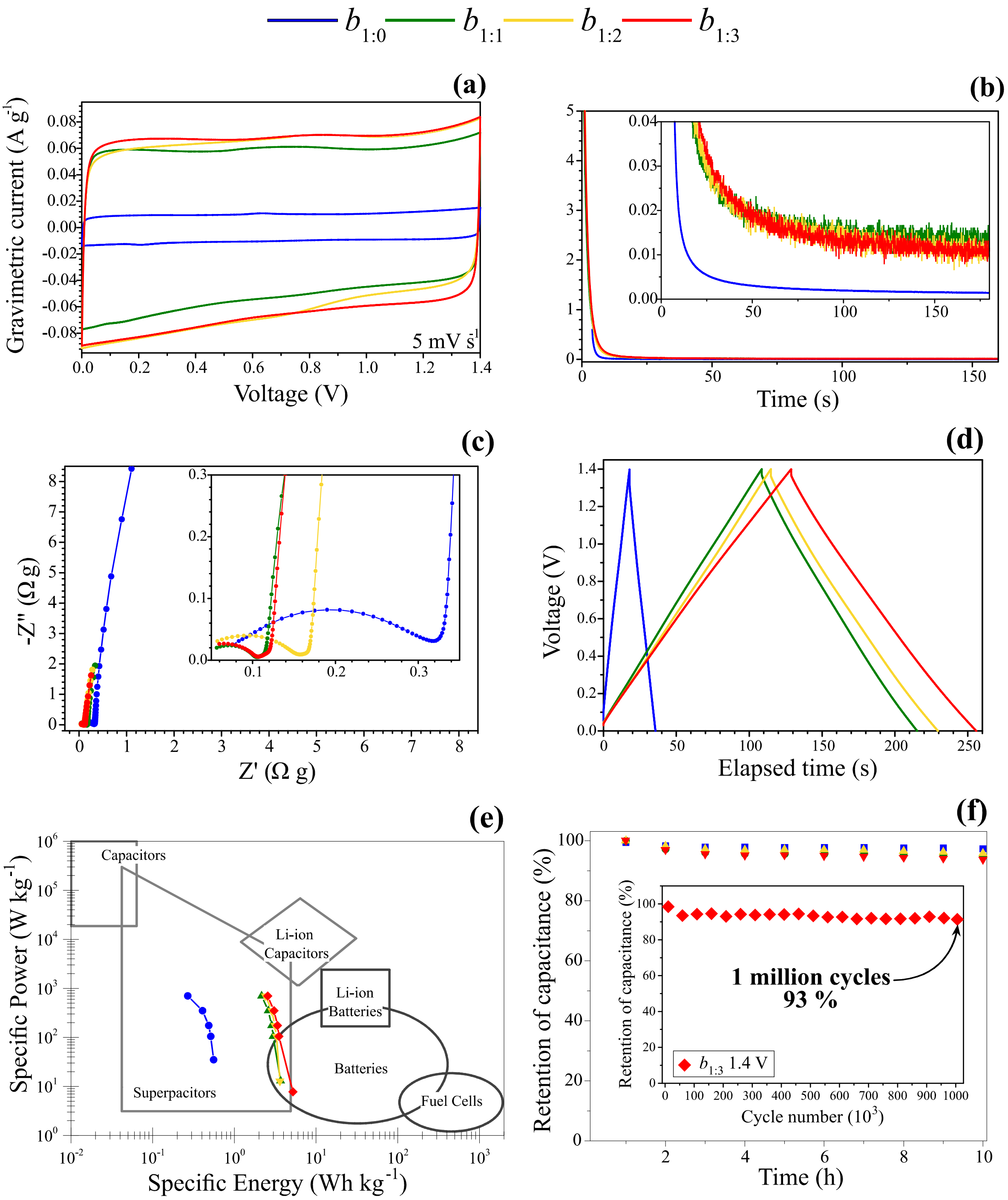

Figure 8. Electrochemical data and performance of the symmetric coin cell as a function of the MWCNT:AC mass ratio. (a) VCs at 5 mV s^{-1}, (b) transient currents during the SSC experiments at 1.4 V, (c) EIS at 1.4 V, (d) GCD at 0.15 A g^{-1}, (e) the Ragone plot, and (f) capacitance retention after 1 mi cycles. Electrolyte: 1.0 mol dm^{-3} Li_2SO_4.

Table 5 gathers the specific capacitance determined from the GCD data. The ESR values for the different samples remained in the range of 140 ± 40 mΩ g. In all cases, the capacitance data corresponds to an applied specific current of 0.15 A g^{-1}.

Ragone Plot is presented in Figure 8 (e), evidencing that activated carbon incorporation into MWCNT buckypaper electrodes improves the energy density of the devices considerably. Also, it is essential to check the capacitance retention after several cycles. To exterminate any doubt from the scientific community and our curiosity, we check capacitance retention after 1 million cycles with a GCD technique at 2.0 A g^{-1} for our best composite (Others samples were not tested because the test took 100 days to be completed). A working voltage window of 1.4 V. Figure 8 (f) shows a high coulombic efficiency of about 93% each is incredibly good, evidence that the energy storage process here is mainly electrostatic.

Table 5. Effect of the MWCNT:AC mass ratio on the specific capacitance (SC) of the buckypaper electrodes.

Sample	SC ($F\ g^{-1}$)
$b_{1:0}$	7.6
$b_{1:1}$	44.0
$b_{1:2}$	48.2
$b_{1:3}$	51.7

After all, there is a significant concern regarding the self-supported electrode materials, which are great for fundamental science but useless in terms of scalability. The main issue concerns welding freestanding carbon materials, making it difficult to associate them in series or parallel. In this sense, we developed a particular welding process to overcome these constraints and presented that in Figure 9. First, we separate the several buckypaper strips and aligned them face-to-face. A Ni tab is on both the bottom- and topsides of one tip of the buckypaper strips, and with a spot welder, we weld several times the robust material i.e., dots at Ni tabs. The electric contact between tabs and buckypaper is excellent, showing metallic continuity i.e., 0Ω.

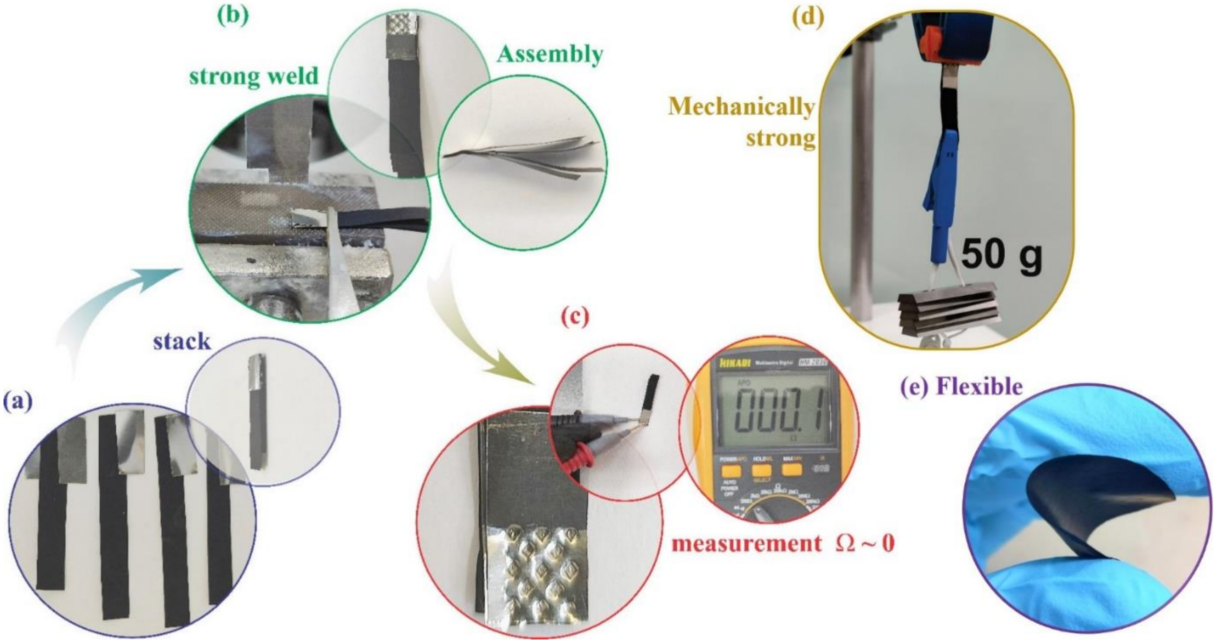

Figure 9. Four steps for welding buckypapers: (a) stacking, (b) welding, (c) measuring the electric contact, and (d) evaluation of the mechanical robustness (e) flexible material.

2.4. Conclusions

We reported the synthesis of binder-free, self-supported, and flexible high-surface-area buckypaper electrodes composed of mixtures containing Activated Carbon (AC) and multi-walled carbon nanotubes (MWCNT). Our innovative electrode synthesis avoided corrosion issues regarding the current collector. We carried out a robust welding technology capable of providing secure and facile fastening of metallic connectors to the freestanding electrode with very high electronic contact. The Raman study revealed the chemical properties of the MWCNT:AC composite is due to both species, confirming reduction on crystallinity and insertion of oxygen functional groups. The AC particles provided a large specific surface area while the MWCNT introduced several alternative electron transport pathways. The porous electrode structure was composed of homogeneously dispersed AC particles where MWCNT involves the AC flake-like structures. The use of self-supported electrodes permitted an increase of the capacitance from 7.6 to 51.7 F g^{-1}, which is very close to the carbon material's theoretical limit considering 5 μF cm^{-2} of several Carbon materials.

The buckypaper electrode containing an MWCNT:AC ratio of 1:3 exhibited the best conditions for the charge-storage process, due to its higher surface area. A high working voltage window (WVW) of 1.4 V was obtained in an aqueous electrolyte in the total absence of the water-splitting reaction. The complementary use of chronoamperometry and impedance techniques in addition to cyclic voltammetry seems to be mandatory for the correct identification of WVW.

It was verified that for AC loadings higher than 75%, the buckypaper does not form nor maintains its good mechanical characteristics (e.g., freestanding and flexible properties). The theoretical analysis indicated that almost the entire specific surface area of the buckypaper electrode is electrochemically active during the charge-storage process, which is one great advantage of binder-free systems. It was verified very high electrode stability with 93% capacitance retention after one million charge-discharge cycles. In general, the composite buckypaper electrode material reported in this work is a promising candidate for several different technological applications involving aqueous-based supercapacitors.

3. APPROACH TO IDENTIFY THE WORKING VOLTAGE WINDOW FOR SUPERCAPACITORS

Electrochemical capacitors (ECs) or supercapacitors (SCs) have attracted the attention of the scientific community due to their unique features related to high specific power (P), moderate specific energy (E), and long lifespan (e.g., > 100,000 charge–discharge cycles) [119], [120]. To increase the E-values, we can focus on the capacitance and/or the *working voltage window* (WVW) or *practical capacitive voltage window* (PCVW) since:

$$E = \frac{CU^2}{2}$$

where U is the cell voltage and C is the specific capacitance. Both C and U parameters are affected by the nature of the electrolyte and electrode materials. The most used electrolytes in ECs are organic-based since the latter enable operational conditions up to ~ 3 V [61]. However, organic electrolytes are toxic, flammable, challenging to handle because they are susceptible to contamination with air humidity, and quite expensive [121]. On the contrary, aqueous-based electrolytes are not costly, and they are highly conductive, easy to handle, non-flammable, and environmentally friendly. That is why the aqueous-based electrolytes have attracted so much attention recently for applications in ECs [122].

The main disadvantage exhibited by aqueous electrolytes is the low PCVW predicted in as a result of the water-splitting reaction. In this sense, there is great confusion in the literature regarding the PCVW-values that can be effectively achieved in the case of the aqueous-based supercapacitors. In our opinion, the discrepancies verified in the literature are mainly related to the fact that erroneous assumptions are commonly made considering only the *electrostatic character* of the *charge-storage process* occurring in the *electrical double-layer structure*, i.e., the physicochemical aspects involving the electrolyte stability and the water-splitting process are commonly disregarded by several authors. Hypothetically, we might consider from a *purely electrostatic viewpoint* that a *single symmetric supercapacitor* (e.g., a two-electrode cell system) can be adequately described as a passive system composed of *two identical capacitors connected in series* due to the existence of *two electrical double-layer in sequence*. However, the *maximum cell voltage*, where the water is chemically stable, thus resulting in the existence of a PCVW where the electrical-double layer behavior dominates the electric response, is dictated by thermodynamic and kinetic considerations, since the electrochemical cell can become a ‘reactive system’ losing its apparently ‘passive character' when a voltage threshold is achieved permitting the occurrence of the water electrolysis. As a result, we might erroneously consider that under *standard thermodynamic conditions* (please, see further discussion) a conventional symmetric coin cell would exhibit a *minimum cell voltage* (U_{min}) value of 2.46 V [123]. However, this is not the case since in practice the standard (idealized) thermodynamic value of 1.23 V for the virtual chemical equilibrium involving the irreversible water-splitting process is indeed composed by two different half-reactions occurring at the positive (anode) and negative (cathode) electrodes [122], [124].

According to the principles of chemical thermodynamics, when the activity coefficients (*a*) and fugacities (*f*) of the relevant chemical species are considered unitary (e.g., the standard conditions), we have that a *minimum cell voltage* (U_{min}) of 1.23 V, measured under *zero-current (equilibrium) conditions*, must be applied to establish a *hypothetical chemical equilibrium* for the water electrolysis, which is, in reality, an intrinsically irreversible reaction [122]. Considering the two *half-reactions* occurring simultaneously at the anode (+) and the cathode (−) to originate the water electrolysis, we have that (please, see ref.[124]):

$$\Delta E^{o}(V) = E^{o}_{(+)} - E^{o}_{(-)}$$

$$\equiv U_{min}(V) = 1.23 + 0.0147\ \log[p(O_2)/1.0bar] + 0.0295\log[p(H_2)/1.0bar]$$

Firstly, we verify that the solution pH does not affect the U_{min} values. By contrast, one has that $U_{min} < 1.23$ V when the partial pressures $p(H_2)$ and $p(O_2)$ are lower than 1.0 bar. In practice, since finite U_{min}-values are verified for the coin cells, we have that the partial pressures at the onset of the electrolysis must resides in the range of $0 < p < 1$, thus resulting in a PCVW lower than 1.23 V. This outcome can be the common situation for the aqueous-based supercapacitors since pure hydrogen and oxygen gases at higher partial pressures ($p \cong 1$ bar) are not commonly injected inside the supercapacitor prototypes (e.g., coin cells) [122]. Besides, it is worth noting when the partial pressures are *considered to be zero* at the onset of the water splitting reaction, due to the absence of the gas species, that U_{min} no longer can be thermodynamically described/predicted, i.e., it becomes an undefined quantity. This is the real reason for the *arbitrary choice* of the standard conditions where $p(H_2) = p(O_2) \equiv 1$ are used to 'obtain (predict)' the theoretical value of $\Delta E^{o} = U_{min} = 1.23$ V.

Despite the above thermodynamic (equilibrium) considerations, we have in practice for a given electric current (I) (e.g., kinetic conditions) flowing in the electrochemical system that the *overall cell voltage* (U) for the water electrolysis is given by:

$$U = \Delta E^{o} + \eta_{(OER)} + \eta_{(HER)} + IR_{ESR}$$

where $\eta_{\mathrm{(OER)}}$ and $\eta_{\mathrm{(HER)}}$ are the *overpotentials* for the gas-evolving reactions, and the IR_{ESR} is the ohmic drop due to the presence of an equivalent series resistance (ESR). Therefore, we can argue that the different PCVWs commonly verified in the literature for several different aqueous-based electrolytes, and electrode materials, are mainly due to the different electrocatalytic activities exhibited by the anode and cathode materials for the OER and HER. As can be seen, the question regarding the theoretical predictions of the PCVW is not straightforward since it involves several chemical and thermodynamic aspects.

From the above considerations, we must emphasize that very high working voltage ranges (e.g., ~ 2.0 V) in aqueous media can be achieved in practice using the *water-in-salt electrolytes* (WISEs) [96][125]–[127]. In this case, the interface and bulk properties of the solvent can be drastically affected due to an excess of salt particles in relation to the water molecules which in turns lead to very strong short-range coulombic interactions, i.e., pronounced deviations from the ideal solution behavior can be expected for WISEs since the *activity* and *osmotic coefficients* are affected by the strong solute–solute interactions. As a result, the relative permittivity (ε_{r}) and the specific conductance (δ) inside the cell can be drastically affected thus altering the specific capacitance and the electrolyte resistance, as well as the overpotential for the gas-evolving reactions due to water-splitting [128]–[130]. The latter effect is the major factor to obtain in practice a high capacitive working voltage range in an aqueous medium.

Several literature reports discussed that aqueous-based supercapacitors can exhibit voltage values higher than 1.23 V [131]–[135]. Some works even reported values of up ~ 1.5 V to ~ 3.0 V [90]–[105]. As can be verified, the question regarding the practical capacitive voltage ranges attained for different aqueous-based electrolytes is a source of great confusion in the literature. Therefore, several research groups, including ourselves, are devoting efforts to optimize the electrolyte conditions to improve the practical (experimental) working voltage window for aqueous based supercapacitors. It is worth mentioning that electrochemical methods such as cyclic voltammetry (CV) and galvanostatic charge–discharge (GCD) are not very sensitive to detect the water-splitting process since the use of a dynamic variable (e.g., the scan rate or the applied gravimetric current) masks the occurrence of the irreversible ‘parasitic’ electrochemical reactions. As a result, only after the long-term GCD we can indirectly detect the gas evolution process through the internal pressure increase. On the contrary, with the use of the *single-pulse chronoamperometr*y (CA) and/or the *electrochemical impedance spectroscopy* (EIS) techniques the *real capacitive voltage interval* where the electrolyte decomposition is absent can be detected.

In the case of CA, we have after application of the different voltage pulses that the nature of the measured current can be easily discriminated, i.e., a true capacitive current must exponentially decrease to zero while in the case of the Faradaic current a non-negligible constant current is verified after longer polarization times. Considering the EIS experiments, the occurrence of a true capacitive process in the presence of an ESR is characterized by an inclined line in the complex-plane (Nyquist) plot that is almost parallel to the imaginary axis due to occurrence of a phase angle (ϕ) very close to − 90°. On the contrary, the presence of a Faradaic current implies in the existence of a *charge-transfer resistance* (R_{ct}) in parallel to the *electrical double-layer capacitive behavior* and, therefore, the complex-plane plot exhibits a well-defined *depressed semicircle* whose radius progressively decreases as a function of the applied voltage.

From the above considerations, the aim of the present work is the application of different electrochemical techniques to correctly identify the true *working voltage window* (WVW) for aqueous-based supercapacitors. We hope that our work aids different researchers to identify true capacitive voltage intervals thus avoiding the publication of illusory/erroneous specific capacitance, energy, and power for supercapacitors due to the undesirable presence of a parasitic Faradaic process.

3.1. Experimental Section

We applied an all-carbon electrode to be an electrochemical platform for study this work. For that, we prepared buckypaper (BP), combining multi-walled carbon nanotubes (MWCNTs) with activated carbon (AC) on ratio mass of 1 (MWCNT):2 (AC), which is our optimized version we produced in our lab. MWCNTs were purchased from CNT Co., Ltd., Korea (conditions: Ctube-120, 95% purity, diameter from 10 to 40 nm, and length from 1 to 25 μm). AC was purchased from Kuraray Co., Ltd, Japan (conditions: YP-50F, surface area

1692 m^2 g^{-1}, bulk density 0.3 g mL^{-1}). Sodium dodecyl sulfate (SDS) was purchased from Synth, 90% purity. Purum P.A. products were used throughout.

We sonicated 200 mL of deionized water with SDS in the presence of 25 mg of MWCNTs and 50 mg of AC for 30 min (constant duty-cycle, 80 W) [149]. The suspension was then slowly filtered using vacuum filtration with a 0.22 μm PTFE membrane from Millipore. The entire process was accomplished after 2 h. Samples were washed several times with deionized water to remove all SDS. Buckypaper was peeled directly from the PTFE membranes and dried at room temperature overnight. The BP was cut with a diameter of 1.2 cm to fit the CR2032 coin cell.

Scanning electron microscopy (SEM) experiments were performed using a FEI inspect F50 microscope. Raman spectrum was taken using a Renishaw inVia Raman spectroscope employing a 633 nm excitation wavelength.

All electrochemical analyses were performed using CR2032 coin cell, two identical optimized BP discs as the electrodes, a porous cellulosic membrane separator soaked in 1.0 M Li_2SO_4 aqueous solution. Electrochemical studies started after the activation process accomplished by applying twenty consecutive voltammetric cycles to permit adequate electrolyte penetration inside the porous electrode structure. For this first stability test, we ranged the cell voltage from 0 to 0.7 V, where we have only the electrostatic process. For the first window, we increased the voltage from 0 to 0.1 V, and then back to 0 V. In the sequence, we increased from 0 to 0.2 V and then back to 0 V, and so on. For each window, we performed CV, CA, and EIS experiments before extending the voltage to the next level.

For each voltage window, voltammetric curves (VCs) were registered using the scan rates of 1, 10, and 100 mV s^{-1}. To assure internal consistency regarding the different electrochemical findings, CA experiments were performed by applying a voltage step function where the latter was fixed equal to the maximum (vertex) voltage previously verified in the voltammetric experiments. For the different windows, the transient current was measured during 300 s. Accordingly, for each voltage window, an EIS experiment was accomplished using a d.c. bias equals the vertex voltage verified in the voltammetric analysis. A frequency range of 100 kHz to 10 mHz with ten points collected per decade was used in all cases by applying a small sinusoidal perturbation of 10 mV (peak-to-peak) to ensure linearity on the impedance response. Electrochemical studies were performed using a model VersaSTAT 4 potentiostat from Ametek.

3.2. Results and discussion

Figure 10 presents typical SEM micrographs (a–d) of the bulkypaper (BP) electrodes used in this work. The inset of Figure 10 (a) shows a picture of the as-prepared flexible BP disc electrode. From SEM data, we can observe a highly porous electrode surface composed of ~ 7-µm AC particles and MWCNTs with an average diameter of ~ 30 nm, and length higher than 2 µm. The entangled MWCNTs interconnect several AC particles forming a complex porous network. The connections between CNTs and ACs allowed for greater mechanical strength and flexibility, as well as higher electronic conductivity. The obtained carbon electrode is robust and easy to handle.

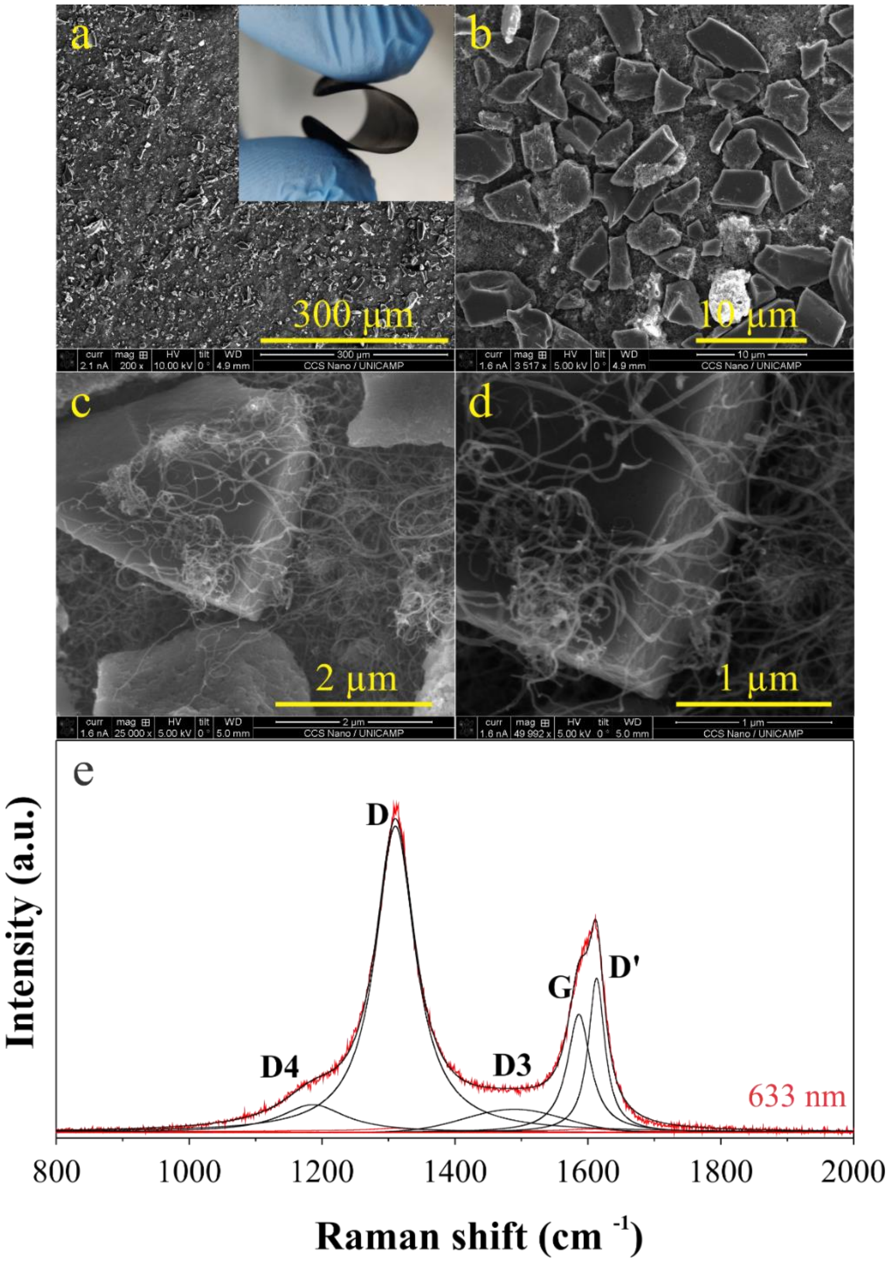

Figure 10. SEM micrographs (a–d) and (e) Raman spectrum took from BP electrodes. The inset in (a) shows a photo of the as-prepared flexible BP disc electrode used in the CR2032 coin cell.

Figure 11 (e) shows the Raman spectrum for the as-prepared BP sample which we deconvoluted into five peaks (e.g., four D-like peaks and one G-peak). The D-peak appears when the lattice vibration (Raman-inactive process) hits a defect causing the breaking of the symmetry. Accordingly, the D-peak is double resonant LO phonons around the K point [106] while the G-band is an E_{2g} optical mode centered at 1582 cm^{-1}, originated from the double degenerate vibrational mode of iLO and iTO phonon branches crossing at the Γ point in the first Brillouin zone of the graphite structure. The G-peak corresponds to the high-frequency E_{2g} phonon at Γ and D is the breathing modes of six-atom rings, requiring a defect for its activation [150].

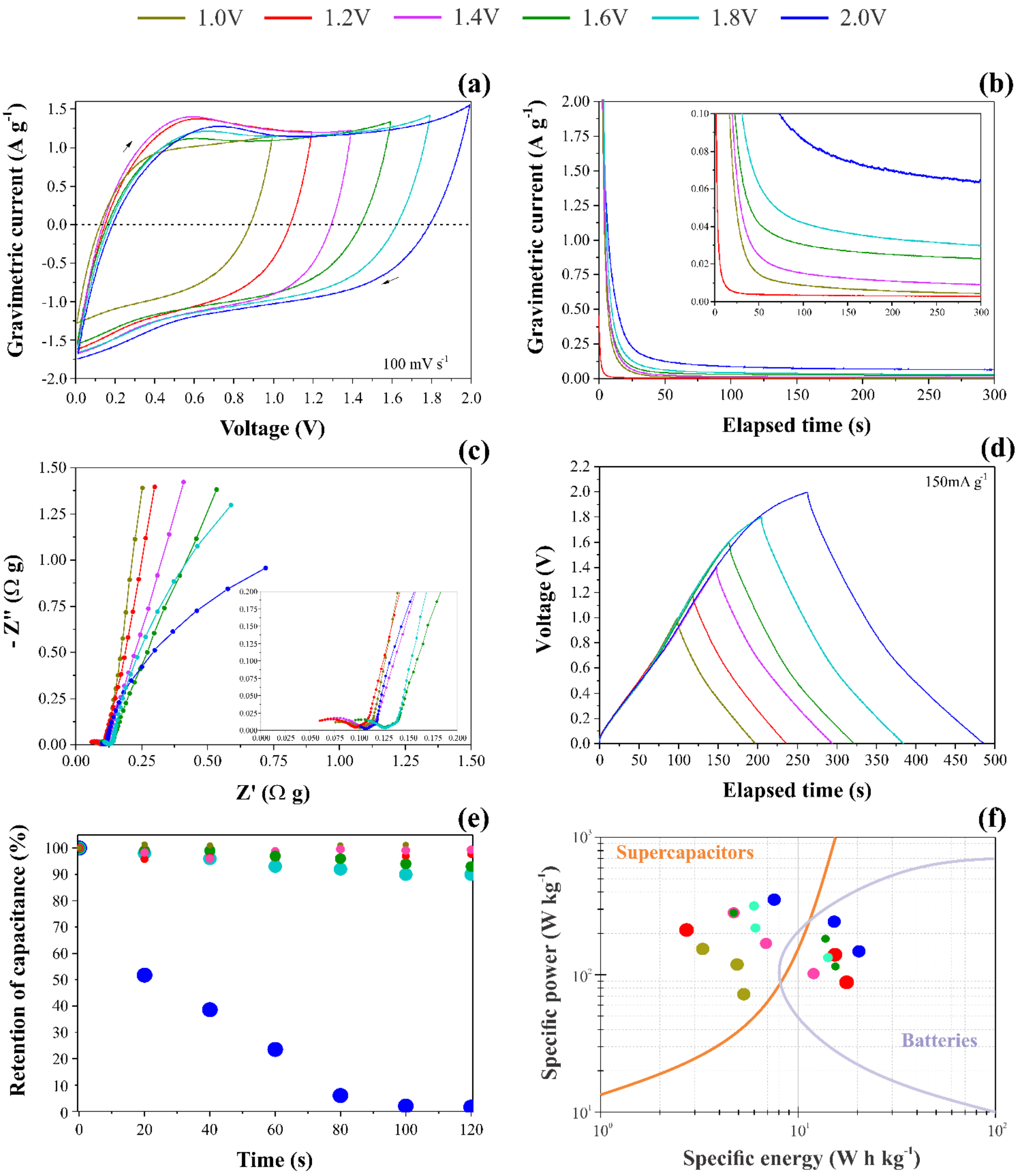

Figure 11. Electrochemical findings obtained for the symmetric CR2032 supercapacitor prototype containing a 1.0 M Li_2SO_4 solution: (a) voltammetric curves with different working voltage windows; (b) chronoamperometric data; (c) impedance findings (Nyquist plots); (d) galvanostatic charge–discharge curves; (e) cyclability test, and (f) Ragone Plot.

Figure 11 shows several electrochemical findings obtained using different experimental techniques. Firstly, the criterion to register the CVs in a given electrolyte using a potentiostat is the accurate choice of a voltage window where the electrolyte is stable and the electrodes do not undergo wear. As a result, we expect to obtain almost rectangular (“mirror-like”) voltammetric profiles. For sake of running a large number of assisted experiments extending the voltage window, it is more pleasured to scan cells at relatively fast scan rates (e.g., ~ 100 mV s$_{-1}$), which is also more close to fast charge/discharge events occurring in the supercapacitor. However, for this relatively high scan rates, a small parasitic Faradaic current is present due to water electrolysis. This is the normal case even when we have quasi-rectangular EDLC patterns for CVs since the cyclic voltammetry is not sensitive to discriminate a pure capacitive process from an irreversible gas-evolving reaction occurring in parallel with a relatively small current efficiency.

Figure 12 (a) shows CVs obtained at 100 mV s^{-1} as a function of the anodic vertex voltage, which behavior is characteristic of supercapacitors. It is worth mentioning that the presence of a ’tail’ at the vertex voltage is commonly adopted as clear evidence of the water-splitting process. However, this criterion alone is not entirely satisfactory for practical purposes. Please, from Figure 12, see a further discussion regarding the crucial influence of the scan rate on the CV profiles.

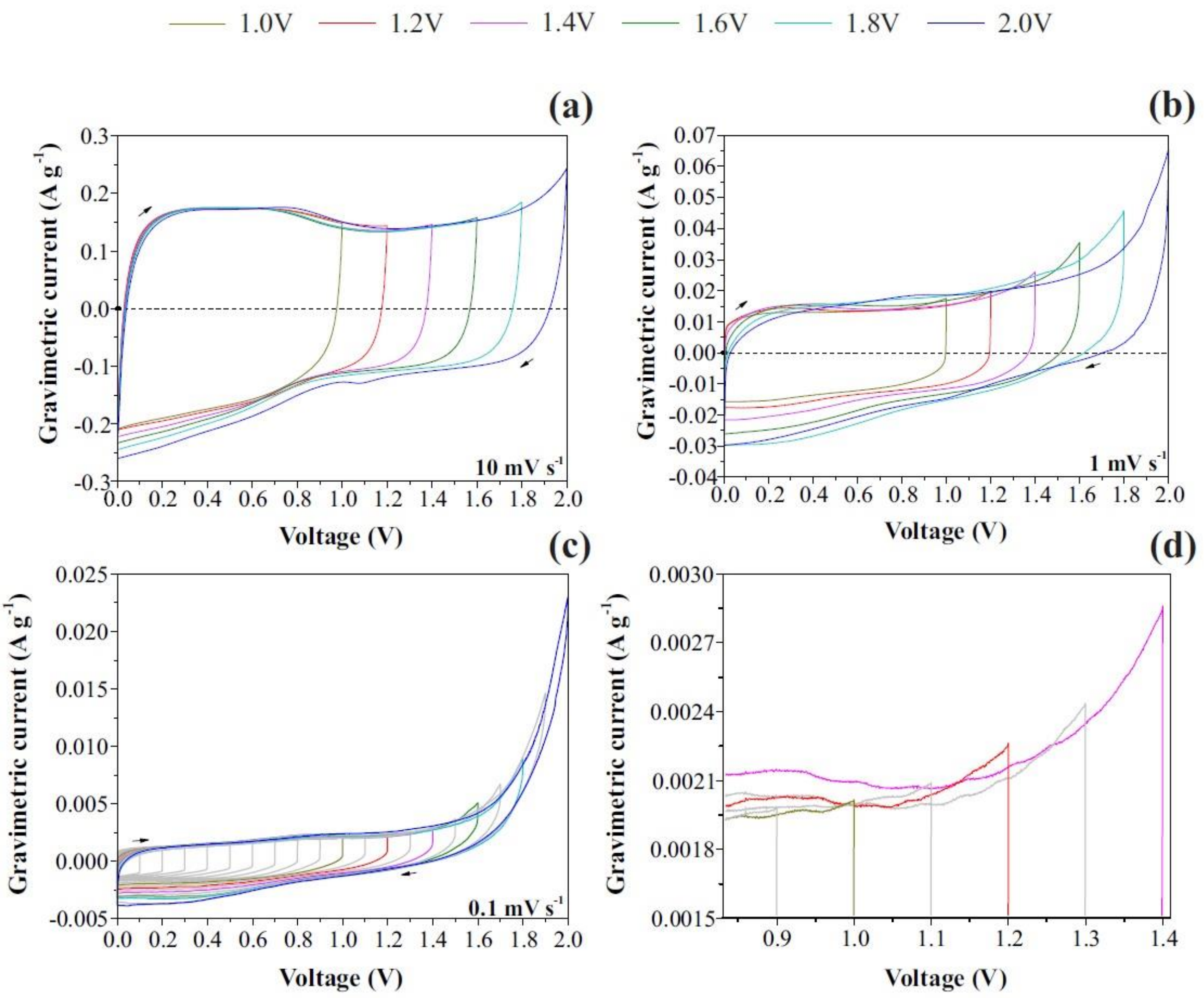

Figure 12. Voltammograms obtained at (a) 10 mV s^{-1}, (b) 1 mV s^{-1}, (c) 0.1 mV s^{-1} and (d) zoom in the region 0.9 to 1.4 V of the graphic (c) for the symmetric coin using BP electrodes soaked with a 1.0 M Li_2SO_4 aqueous solution.

From the above considerations, we performed additional experiments using the CA technique to correctly identify the eventual presence of a Faradaic current occurring during the transient current characteristic of a capacitive discharge process. After a long polarization time necessary for a practical full discharge of the device in the absence of a Faradaic (parasitic) current (see Figure 11 (b)), we observed for voltages higher than 1 V the presence of almost stationary currents whose magnitude dramatically increased with the window voltage (e.g., 2.6 mA g^{-1} @ 1.2 V and 64 mA g^{-1} @ 2 V). These findings confirmed the occurrence of the water-splitting reaction, which was not possible to detect using only the CV technique. Therefore, we can affirm that our aqueous-based EDLC device can only be operated with confidence in the absence of parasitic gas-evolving reactions when $U \leq 1.2$ V.

Even considering that the CA findings are quite conclusive to correctly identify the real capacitive voltage window for supercapacitors, we performed further complementary studies in the frequency domain using the EIS technique. Figure 11 (c) shows the Nyquist plots obtained for different d.c. bias corresponding to the voltages used in the CV and CA experiments. For lower d.c. voltages (e.g., 1 and 1.2 V), it was verified in the low-frequency range of the spectra a strong capacitive behavior characterized by an exponent (n) of the constant phase element (CPE) higher than 0.9. Considering that

$$Z_{CPE} = \frac{1}{Y_0(j\omega)^n}$$

when $n = 1$ one has that $Y_0 = C_{\mathrm{edl}}$, i.e., the electrical double layer capacitance is unambiguously determined. However, due to the dispersive capacitive effects, inherent to the presence of surface inhomogeneities in solid electrodes, using the well-known Brugg–Sluyters formula we have as a guide for the precise determination of the capacitance value the practical interval of $0.9 \leq n \leq 1$. For these conditions regarding the CPE behavior, we have that the impedance response in the low-frequency range for EDLCs is characterized by a straight line almost parallel to the imaginary ($Z_{//}$) axis. As seen in Figure 11 (c), for higher voltages (e.g., $U \geq 1.4$ V) the EIS findings at low frequencies start to form a semicircle characterized by $n < 0.9$ since in these cases we have strong deviations from the ideal capacitive behavior due to the presence of a Faradaic component in the Nyquist plot. The inset of Figure 11 (c) evidences the medium–high frequency region where the capacitance dispersion can be attributed to the well-known porous electrode behavior. More precisely, for this type of dispersive effect where we identify the presence of a high-frequency semicircle followed by an inclined line at intermediate frequencies with a phase angle close to − 45°, the porous electrode behavior can be represented by a two-channel transmission line incorporating the anomalous (non-Fickian) transport of the charge carriers in the interconnected solid and liquid phases, i.e., in this case, the Bisquert #2 impedance model can be adequately used for simulation of the impedance data using, for example, the Zview and NOVA software. From these considerations, we can affirm from the perspective of the frequency domain analysis that $U = 1.4$ V is the maximum voltage window that can be used with confidence to avoid the presence of water-splitting in the coin cell.

A comparison of the CA and EIS findings reveals that the former technique is more sensitive for the quantitative identification of parasitic Faradaic reaction occurring simultaneously with the electrical double-layer charge discharging processes. In addition, it became obvious for us that the CV technique is the worst electrochemical technique to be used when the proposal is the accurate identification of the capacitive voltage window for EDLCs.

Figure 11 (d) shows the galvanostatic charge–discharge (GCD) curves obtained for the different voltage windows used to determine the coulombic efficiency and the ESR value. Electrochemical data obtained from GCD analysis were gathered in Table 6. As can be seen, the coulombic efficiency (CE) reduced with the increasing voltage window, i.e., unacceptable values were observed above 1.6 V.

Table 6. CE and ESR values as a function of the working voltage window (WVW).

Working Voltage Window (V)	**Coulombic Efficiency (%)**	**ESR by GCD (Ω g)**
1.0	100	0.16
1.2	100	0.16
1.4	99	0.18
1.6	96	0.17
1.8	88	0.18
2.0	85	0.20

As seen, the CE values only evidenced the presence of a parasitic Faradaic process when $U \geq 1.4$ V. Besides, we verified that the GCD curves have similar triangular profiles characteristic of well-behaved supercapacitors even considering the presence of a small parasitic Faradaic process at voltages higher than 1.2 V (see the previous discussion). Again, we can affirm that the use of the GCD method alone is not satisfactory for the correct identification of the capacitive voltage window. From the GCD findings, we determined the ESR values using the abrupt voltage drop [151].

$$ESR = \frac{\Delta U_{drop}}{2I}$$

As seen in Table 6, the ESR values slightly increased as a function of the cell voltage. In principle, this behavior can be ascribed to the presence of gas bubbles from the water-splitting reaction inside the coin cell, which in turn increased the overall cell resistance.

The practical consequences of the inadequate choice of the voltage window for supercapacitors are shown in Figure 11 (e). As seen, there was an exponential decay of the capacitance value to zero after a cycling process using the floating time method accomplished during 120 min at 2.0 V. On the contrary, there was almost no impact (e.g., 96%) on the capacitance retention at 1.2 V. The accumulation of gases inside the hermetically sealed coin cell provided by the water-splitting process was so great that it caused irreversible damage for the coin cell operated at 2.0 V (i.e., it expanded to open up). Unfortunately, some researchers are inclined to push the working window voltage to erroneously suggest that their cells exhibit more energy and power than other systems reported in the literature. This type of biased (incorrect) characterization of supercapacitors can lead to illusory figures-of merit as can be seen in Figure 11 (f). For instance, the Ragone plot indicated that at 2.0 V the cell has higher energy and power storage capabilities, which is not true since for these conditions part of the electric current is due to water-splitting instead of the reversible charge-storage process.

In several literature reports, the CV experiments are accomplished using high scan rates ($v \geq 50$ mV s$_{-1}$). In this sense, we performed complementary experiments using very low scan rates from 10 to 1.0 mV s^{-1}. These complementary findings are shown in Figure 12. From the theoretical viewpoint, a ‘perfect supercapacitor’ must exhibit a symmetric response of rectangular shape for all scan rates when the ESR is negligible. Therefore, a change in the CV profile as a function of the scan rate due to the appearance of an ‘anodic tail’ close to the vertex voltage is an indication of the occurrence of a parasitic Faradaic reaction, as is the case of the electrolyte decomposition. In this sense, we verified that the apparent capacitive voltage window decreased from ≈1.6 to ≈1.2 V when the scan rate was reduced from 10 to 0.1 mV s^{-1}, respectively. On the whole, these complementary findings support the previous CA results where a true capacitive window was verified only when $U \leq 1.2$ V.

3.3. Conclusion

We reported in this work on the best scientific practices regarding the correct identification of the capacitive working voltage window for supercapacitors. We used as a model device a symmetric aqueous-based supercapacitor composed of carbon-based buckypaper electrodes. Our motivation for this study is the continuous verification in the literature of works that report unrealistic/incorrect figures-of-merit for supercapacitors (e.g., the specific energy and power). We demonstrated here that although there is a pronounced capacitive characteristic verified in the voltammetric study (e.g., quasi-rectangular shaped voltammograms), that these findings can mask the parasitic occurrence of the Faradaic water-splitting process. We verified that the cyclic voltammetry (CV) or galvanostatic charge–discharge (GCD) approaches cannot be used with confidence to correctly identify the capacitive working voltage window for supercapacitors. As a result, complementary studies involving the application of the chronoamperometry (CA) and the impedance (EIS) techniques are highly recommended, if not mandatory, for the accomplishment of a reliable electrochemical characterization of supercapacitors. To quote, we verified that an apparent voltage window of 2 V determined using the CV technique is drastically decreased to 1.2 V after a close inspection of the CA findings used to discriminate the presence of a parasitic Faradaic process. The results obtained with the EIS technique are in close agreement with those determined using the CA technique and in disagreement with the CV findings. In addition, while the cell remained quite stable for the charge-storage process accomplished at 1.2 V, the same cell was completely deactivated after a brief time interval when a voltage of 1.6 V was applied. We hope with this work to instigate the publication of more reliable findings regarding the electrochemical characterization of supercapacitors.

4. STUDY UNDER ABUSIVE REGIME OF SUPERCAPACITOR USING *OPERANDO* XRD & RAMAN TECHNIQUES

Electrochemical supercapacitors (ES) are ultra-fast energy storage devices, storing energy by ion adsorption and fast faradic processes [152]. The specific energy (E) and power (P) stored in ES can be calculated using the following equations.

$$E_{max} = \frac{C_{max}\, U_c^2}{2}$$

$$P_{max} = \frac{U_c^2}{4R_s}$$

where U_c is the total voltage drop referring to the equivalent series resistance (ESR), and R_S is the solution (ionic) resistance obtained from EIS spectra.

Since ES is a long lifespan power device, most researchers want to improve its specific energy (E) and power (P) storage [152]. In order to improve the capacitance, a great strategy is to combine the electrostatic process in all carbon electrodes by decorating them with metal oxides, introducing pseudocapacitance (i.e., solid-state fast faradaic reactions). Even more practical would be to improve cell voltage. In this sense, organic electrolytes are most successful because it has wide electrochemical stability window and allows broader working voltage windows (WVW) of the cell ~3.0 V, offering the best cost-effective relation at the moment [2-4]. Ionic liquid (IL) is also considered a promising class of electrolyte. Chen et al. [156] studied the enhancing capacitance of supercapacitor with both organic electrolyte and ionic liquid electrolyte on a biomass-derived carbon. The authors observed that the IL electrolyte resulted in higher operating WVW and higher capacitance, thus much higher energy density than the organic electrolyte.

Although most IL-cations ion size is more significant than organic-cation ions, the giant solvation shell of organic-cation ions reduces its access to micropores. Once that some carbon micropores can be estimated with the size close to 1.0 nm, such pores with similar ions in the electrolyte significantly enhanced the storage of ions in these confined pore volumes, thus drastically increasing the capacitance in IL electrolyte-carbon system. The impurities removal also opens the partial blocked micropores and mesopores to enhance the capacitance further. Hierarchical pore structure with highly integrated micropores and mesopores also results in superior organic and IL electrolyte material. Chen et al. [156] observed high specific capacitances of 146 F g^{-1} in the organic electrolyte and 224 F g^{-1} in the IL electrolyte at the current density of 0.1 A g^{-1}. However, IL and organic electrolytes are hard to handle due to their higher toxicity and humidity contamination issues. In this context, several recent reports have been studying alternatives considering aqueous-based electrolytes.

The water-in-salt (WISE) electrolytes and salt-in-water neutral aqueous electrolytes [157], [158] have promise WVW as wider as organic electrolytes [159]. Although our group has observed several optimistic issues with WISE experimentally, we have observed that both work reasonably well in WVW up to 2.0 V, close up to the most 2.5 V organic electrolytes [159]. Considering this issue, most researchers based only on Equations 1 and 2 used to work on the abuse voltage regime, where the device, instead of storing more energy, is on the working process of degradation state. Berg et al. [160] were the first to use spectrometric tools (*on-line* electrochemical mass spectrometry) combined with cell pressure analysis to study the ageing phenomena in "high-voltage" aqueous supercapacitors investigated by *in-situ* gas analysis. The authors observed that activated carbon electrodes and oxygen-based surface functionalities (mainly phenol, lactone and anhydride groups), were oxidised already at a cell voltage of 0.6 V to provoke the evolution of minor amounts of CO and CO_2.

Furthermore, water decomposition starts at a high voltage of 1.6 V with the evolution of H_2 on the negative electrode and carbon corrosion on the positive electrode with the generation of predominantly CO. Spectroscopy tools such as operando FTIR and Raman were also used to probing of lithium-ion storage on single-layer graphene under an abusive regime, i.e., 3.0 V [161] into single-layer of graphene. Utilising single-layer graphene eliminates the inevitable intercalation of Li-ions in graphite or few-layer graphene plays fundamental insights from a molecular level. However, from a practical point of view, the study of operando spectroscopy is pivotal to a proper coin-cell supercapacitor electrode device. Therefore, to the best of our knowledge, any paper in the literature reports the initial formation of Li_2CO_3 onto NiO@MWCNT supercapacitor using operando (XRD & Raman) spectroscopy under an abusive regime.

This work investigates the electrode/electrolyte interface within *in-situ* electrochemistry and XRD & Raman *operando* pattern transients. The XRD pattern was produced with high-flux X-ray synchrotron light. The cell is filled with NiO decorated carbon electrodes in the neutral aqueous electrolyte, which operates in normal and abusive voltage regime conditions. Whole *in-situ* electrochemistry and *operando* XRD pattern Raman spectra transients were performed for NiO@MWCNT and only MWCNT as a blank electrode.

Finally, we investigate the origin of cell failure and present a critical discussion on the effectiveness of widening WVW of supercapacitor in aqueous electrolytes.

4.1. Experimental Section

4.1.1. Synthesis and Characterisation of the Composite Electrode Material

MWCNT were grown radially aligned using a homemade CVD furnace onto an AISI 304L M100 fine-mesh substrate cut on disc format (mesh wire diameter of 0.1 mm and mesh pore size of 0.15 mm × 0.15 mm). Before deposition meshes were etched for 8 min using 50 mL of a solution containing concentrated nitric and hydrochloric acids in the proportion of 1:2 (*v*/*v*) and then they were washed with deionised water. In a furnace with N_2 atmosphere the temperature was increased at a rate of 65 °C min^{-1} up to 750 ºC. To MWCNT growth 43.6 wt% of Camphor and 2 wt% of $Ni(NO_3)_2$ dissolved in ethanol were carried into the furnace by 15000 sccm of N_2 gas for 20 min. $Ni(NO_3)_2$ forms nickel nanoparticles (NPs) in the furnace, catalytic particles for MWCNT formation. Other essential elements are iron and chromium, which came from the AISI substrate by diffusion in the early stage, in which the substrate is at 750 °C for 10 min. After preparation, MWCNT masses were roughly estimated at ~2.0 mg, comparing each disc's initial and final masses [162]. As prepared electrode material, we henceforward refer to as MWCNT.

The NiO particles onto MWCNTs were prepared by immersion in an ethanol solution containing 0.1 mol L^{-1} $Ni(NO_3)_2$ for 48 h. Afterwards was heated to 100 ºC to vaporise ethanol, annealed in an air atmosphere at 350 ºC for 1.0 h and cooling down for 24 h. The NiO mass of the active material per electrode is 0.1 mg measured by Radwag MYA 11.4Y ultra microbalance [162].

Morphology and nanostructure of the NiO@MWCNT electrode was characterised by scanning electron microscopy using a model Inspect F50 scanning electron microscope from FEI equipped with high-speed and sensitivity XEDS system of 80 mm^2 SDD from Oxford and by high-resolution transmission electron microscope using a model 2100 MSC JEOL. Samples were dispersed in isopropanol using an ultrasonic bath and dropped on a TEM lacey carbon film supported on a copper mesh.

Raman spectra were taken using a Renishaw inVia spectrometer to investigate the samples where a 785nm excitation wavelength was applied and focused on a 50× objective lens at room temperature. The Raman shift was calibrated using a standard diamond sample with the peak position at 1332 cm^{-1}. The adapted cell holder was coupled to the spectrometer to accomplish *operando* measurements.

XRD analyses were performed on the XPD beamline at the Brazilian Synchrotron Light Laboratory (LNLS-CNPEM), operating at an energy of 8 keV ($\lambda = 1.5473$ Å) in Bragg-Brentano geometry. Diffractograms were collected in a 2θ angular range with a Mythen - 1K linear detector (Dectris) installed at 1 m from the sample. All XRD measurements were performed using these parameters. XRD under dynamic polarisation conditions measurements were performed at a constant voltage all along with the experiment. Synchrotron Light had 8 keV ($\lambda = 1.5473$ Å) in Bragg-Brentano geometry. Diffractograms were collected in a 2θ angular range with a Mythen - 1K linear detector (Dectris) installed at 1 m from the sample.

Camphor PA ($C_{10}H_{16}O$) and nickel (II) nitrate hexahydrate PA $Ni(NO_3)_2{\cdot}6H_2O$ were purchased from Synth®. Ethanol PA (C_2H_5OH) was purchased from Merck®. Nitrogen gas (N_2) was purchased from White Martins®. All chemicals were used as received.

4.1.2. in situ Electrochemical characterisation studies

The electrochemical studies of NiO@MWCNT electrodes in a coin cell filled with 1.0 mol L^{-1} Li_2SO_4 aqueous solution were performed in VersaSTAT 4 potentiostat from Ametek. Coin cell set-up could be observed in detail elsewhere [132], [158]. The accomplished electrochemical techniques used as a figure of merit for supercapacitor characterisation e.g., cyclic voltammetry, galvanostatic charge-discharge, gravimetric current and electrochemical impedance spectroscopy, were described in detail elsewhere [162].

All electrochemical measurements under dynamic polarisation conditions (XRD & Raman) were taken under chronoamperometry steps from 0 up to 2.2 V using a coin cell with Kapton® window and an adapted cell holder for electrifying the device, shown in Figure 13. Each chronoamperometry step was recorded along 30 minutes towards cathodic and anodic values until obtained the stabilised residual current.

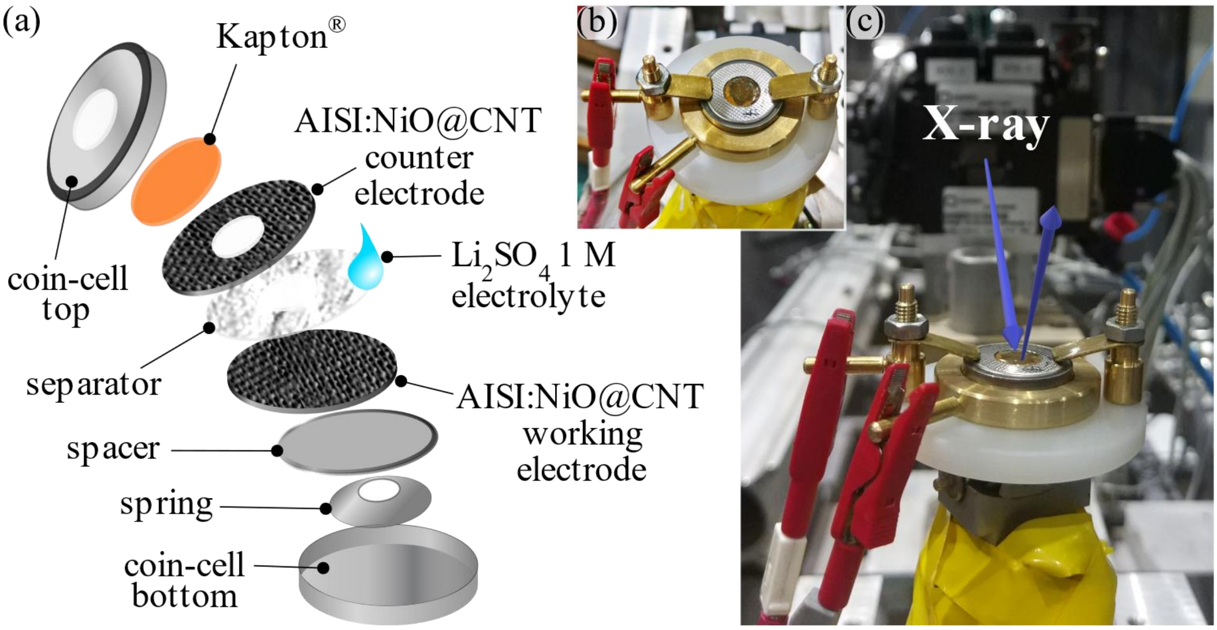

Figure 13. Measurements under dynamic polarization conditions: a) coin cell set up; b) coin cell with a Kapton® window and; c) adapted cell holder.

4.2. Results and discussion

Recently, our research group published [162] the study of NiO@MWCNT as electrodes for electrochemical capacitors in a proper symmetric CR2032 coin-cell arrangement device. The transmission electron microscopy analysis revealed that CNTs have a turbostratic multi-walled structure containing a few dozen walls with an interplanar spacing of 0.32 ± 0.02 nm and a diameter ranging from 20 to 100 nm [162]. It was confirmed using the X-ray technique that MWCNTs were successfully decorated with NiO nanoparticles having a diameter of ~ 2.7 nm [162]. It was verified that high specific capacitance of ~1200 F g^{-1} at 5 A g^{-1} due to NiO pseudocapacitance behaviour. The specific power (P) and energy (E) determined using cyclic voltammetry exhibited values of ~140 Wh kg^{-1} and ~ 9 W kg^{-1}, respectively, at 0.02 V s^{-1} [162]. Also, an extremely high specific capacitance of ~1028 F g^{-1} was obtained at this scan rate (Please note capacitance of CV is differential and from GCD is integral). It was verified that even after 40,000 cycles the symmetric coin cell exhibits an extremely high coulombic efficiency (h) of ~ 99% for the charge storage process [162]. In summary, all these promising figures of merit for supercapacitor characterisation lead us to study the initial formation of Li_2CO_3 onto NiO@MWCNT supercapacitor using operando (XRD & Raman) spectroscopy under the deliberate abusive regime.

4.2.1. XRD analysis

Figure 14 shows XRD diffractograms obtained along positive polarisation (green lines) and negative polarisation (orange lines) at different constant voltages from 0.2 to 2.2 V. Figure 1 (a) presents XRD pattern from the symmetrical coin cell with MWCNTs electrodes in 1.0 mol L^{-1} Li_2SO_4 aqueous medium. It is possible to observe that, even at 2.2V no crystalline phase was observed in the diffractogram. The XRD spectrum of pristine crystallography phase MWCNTs displayed a strong sharp peak at $2\theta \simeq 26.10°$ assigned as graphite (0 0 2)-*hkl* lattice face according to PDF# 00-058-1638. Figure 14 (b) presents the *operando* XRD diffraction pattern of NiO@MWCNT electrodes in a symmetrical coin cell with 1.0 mol L^{-1} Li_2SO_4 aqueous medium. The crystallography phase graphite (0 0 2)-*hkl* lattice face is still possible to observe, however, it was shifted to $2\theta \simeq 26.60°$ lower interplanar spacing value. It is related to a compressive strain observed in NiO@MWCNT compared to MWCNT nanostructures.

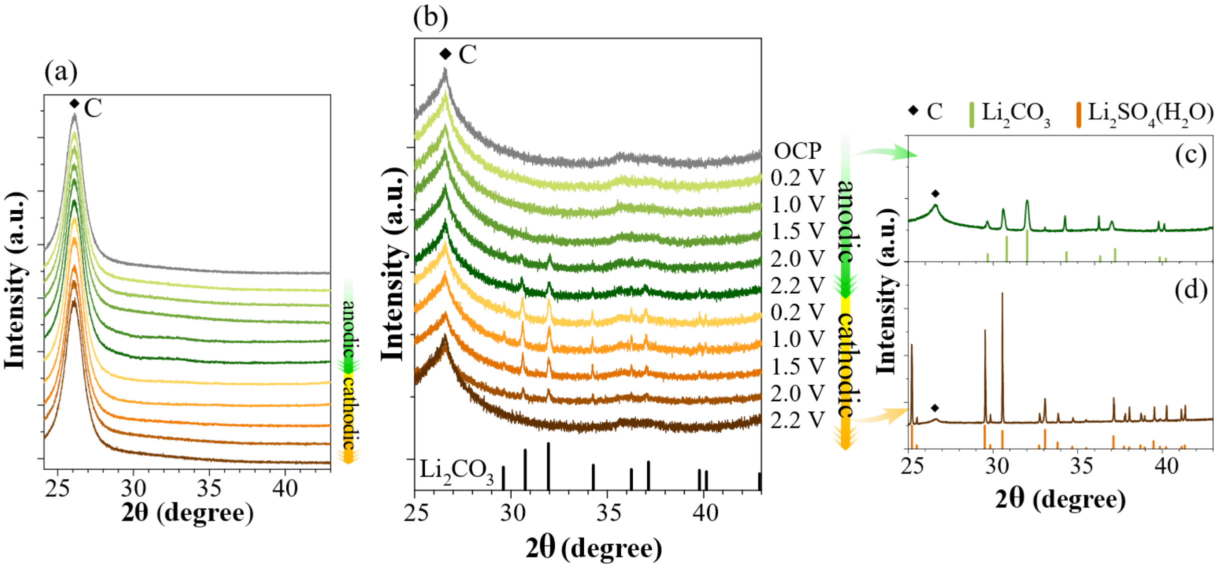

Figure 14. *Operando* XRD diffractograms from a) MWCNTs and b) NiO@MWCNTs electrodes in the coin cell. All XRD diffraction patterns were taken under constant voltage during anodic polarization for NiO@MWCNTs anode (positive pole) green lines and

NiO@MWCNTs cathode (negative pole) orange lines. XRD pattern after 2.0 hours floating time at 2.2 V for c) NiO@MWCNTs anode (positive pole) and d) NiO@MWCNTs cathode (negative pole). Symmetrical coin cell at 25 ^{o}C and Li_2SO_4 1.0 mol L^{-1} aqueous medium.

Compressive strain onto CNTs has been reported in the literature using experimental and/or theoretical approaches, even with Ni dispersed onto CNT (Ni-CNT) [163]–[166]. Miura et al. [163] studied the effects of uniaxial compressive strain on the electronic transport properties of zigzag carbon nanotubes using molecular dynamics. According to the authors [163], in the initial stage (up to column-buckling deformation), both the LDOS and the conductance near the Fermi level decreased because of the homogeneous axial strain. However, because column-buckling deformation relaxes the compressive strain on the bond lengths, the decreases in the LDOS and the conductance near the Fermi level begin to increase slightly. As a result, shell-buckling deformation causes a sudden increase in π-orbital angles near the buckled area, which causes σ*–π* orbital hybridisation and, thus, localisation of LDOS in the large π-orbital angle area. The critical value of the π-orbital angle required to induce σ*–π* orbital hybridisation observed by the authors [163] was estimated to be approximately 30°. Banerjee et al. [166] also studied the strength and ductility of Ni-CNT matrix nanocomposites. According to the authors [166], the I_D/I_G ratio Raman bands and peak shifts observed may imply a slight increase in structural disorder indicative of residual compressive stress.

It is possible to notice in Figure 14 (b) towards anodic sweep onto positive pole, i.e. 2.0V, peaks related to crystallography phase Li_2CO_3 of monoclinic crystal system and spatial group *C12/c1* located at 2θ ≃ 29.6°, 30.6°, 32.0°, 34.2°, 36.2°, 37.0°, 39.8°, and 40.1°, which correspond to (1 1 1), ($\bar{2}$ 0 2), (0 0 2), ($\bar{1}$ 1 2), (0 2 0), ($\bar{3}$ 1 1), (0 2 1) and, (3 1 0) *hkl*-planes, respectively, according to the file card ICSD-66941. The least squares refinement routine to retrieve unit cell constants from diffraction data were performed using Holland et al. [167] procedure and the lattice parameter are presented in Table 7, and the structure in Figure 15 (a). Also, in Table 7, the convergence parameters obtained residuals: standard, average, and maximum deviations. It was possible to notice a compressive strain for crystallography phase Li_2CO_3 obtained onto NiO@MWCNTs, once that lattice parameters related into file card ICSD-66941 were a = 8.35884(12) Å, b = 4.97375(6) Å, c = 6.19377(8) Å, β = 114.789(1)^{o} and unit cell volume = 233.78 Å^3.

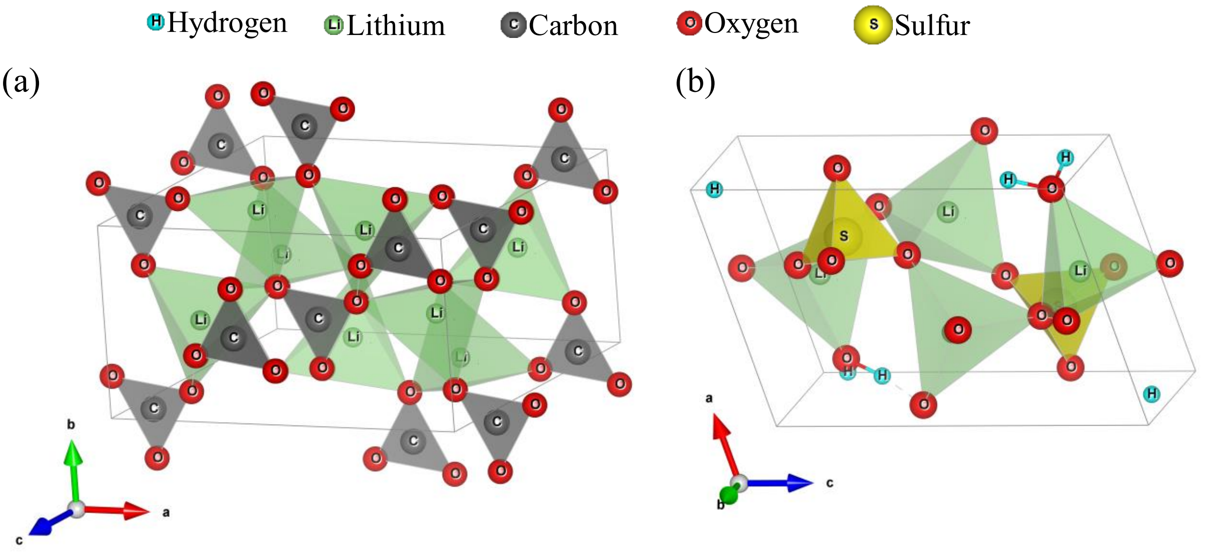

Figure 15. Crystallographic structures of a) Li_2CO_3 and b) $Li_2SO_4{\cdot}H_2O$ presented into XRD of Figure 14 (c-d).

The *in situ* XRD pattern of both NiO@MWCNT electrodes were also analyzed along anodic sweep up to 2.2 V for positive and negative symmetric coin-cell poles-electrodes. Figure 14 (c) shows the positive electrode containing the crystallography phase Li_2CO_3 as previously reported. Figure 14 (d) shows the negative pole which presented peaks related to crystallography phase $Li_2SO_4{\cdot}H_2O$ monoclinic crystal structure and space group $P2_1$ [168]–[170] located at $2\theta \simeq 25.20^{\circ}$, 25.50°, 29.54°, 30.55°, 32.76°, 33.84°, 37.13° and 39.53°, which correspond to $(1\ \bar{1}\ 0)$, $(1\ 1\ \bar{1})$, $(0\ 1\ 2)$, $(1\ 1\ \bar{2})$, $(2\ 0\ \bar{1})$, $(1\ 0\ \bar{3})$, $(0\ \bar{2}\ 0)$ and $(2\ 0\ 1)$ *hkl*-planes, respectively, according to the file card ICSD- 751. The least squares refinement routine to retrieve unit cell constants from diffraction data were also performed using Holland et al. [167] procedure and the lattice parameter are presented in Table 2, and the structure in Figure 2b. Also, in Table 2, the convergence parameters obtained residuals: standard, average, and maximum deviations. It was possible to notice a compressive strain for crystallography phase $Li_2SO_4{\cdot}H_2O$ obtained onto NiO@MWCNTs, once that lattice parameters related on file card ICSD-751 were a = 5.4535(2) Å, b = 4.8390(2) Å, c = 8.1481(3) Å, β = 107.196(1) ^{o} and unit cell volume = 205.41 Å^3.

Table 7. Least squares refinement of the Li_2CO_3 monoclinic crystal structure from diffraction data.

Parameter	**Value**	**Sigma (σ)**	**95% conf.**
a	8.35433 Å	0.00143	0.00616
b	4.95166 Å	0.00063	0.00273
c	6.17279 Å	0.00072	0.00311
β	115.17286°	0.01421	0.06143
Unit cell volume	231.1030 Å^3	0.0465	0.2010
Standard deviation (2T)	0.0040		
Average deviation (2T)	0.0033		
Maximum deviation (2T)	0.0069		
Sigmafit	1.3703		
Students *t*	4.32		

Table 8. Least squares refinement of the $Li_2SO_4 \cdot H_2O$ monoclinic crystal structure from diffraction data.

Parameter	**Value**	**Sigma (σ)**	**95% conf.**
a	5.44290 Å	0.00051	0.00130
b	4.83159 Å	0.00054	0.00139
c	8.11607 Å	0.00109	0.00279
β	106.96362°	0.01228	0.03152
Unit cell volume	204.1488 Å^3	0.0340	0.0873
Standard deviation (2T)	0.0823		
Average deviation (2T)	0.0650		
Maximum deviation (2T)	0.1543		
Sigmafit	22.0833		
Students *t*	2.57		

From water electrolysis, we know [171], [172]:

Overall: $$H_2O \longrightarrow H_2 + \frac{1}{2}O_2$$ Reaction 1

where, H_2 and O_2 are obtained at cathode (negative pole) and anode (positive pole) electrodes, respectively. Therefore, this reaction can be studied separately as:

Anode: $$H_2O \longrightarrow 2H^+ + \frac{1}{2}O_2 + 2\bar{e}$$ Reaction 2

Cathode: $$2H^+ + 2\bar{e} \longrightarrow H_2$$ Reaction 3

As a result, it can be noticed that gas evolution, i.e. O_2 and H_2 are prominent to occur onto anode (positive pole) and cathode (negative pole) electrodes, respectively. Several authors studied using experimental and theoretical models the H_2 and O_2 bubbles evolution under H_2O electrolysis conditions and its effect onto the surface [173]–[178]. Liu et al. [175] studied the H_2 bubble evolution from nickel wire electrode. According to the authors [175], the mean H_2 bubble diameter decreases from s 252 µm if the wire electrode is not magnetised, and the diameter can be reduced to 152 µm once the magnetised electrode is adopted. Also, the Lorentz force is along the axial direction of the electrode, which is up to the maximum of about 12 N m^{-3} nearby the electrode surface, and it is rapidly weakened away from the electrode surface and decreases to below 2 N m^{-3} at the bubble top [175]. Torem et al. [176] studied the H_2 and O_2 bubbles diameter produced by electroflotation processes. According to the authors [176], the O_2 bubbles attained Sauter mean diameters of d=64.0 µm, and d= 65.1 µm at pH 3 and 5, respectively. Therefore, these massive values of H_2 and O_2 bubble diameter and pressure e.g. 212.64 Pa [177] are responsible for MWCNT (diameter ranging from 20 to 100 nm [162]) degradation and obtaining Li_2CO_3 and $Li_2SO_4{\cdot}H_2O$ crystal structures, as discussed below.

As observed in Figure 14 (d), the XRD spectra of $Li_2SO_4{\cdot}H_2O$ monoclinic crystal structure were obtained onto the cathode (negative pole) electrode under 2.2V after 2.0 hours. Such harsh conditions lead to a significant H_2 gas evolution and, consequently, local exhausted H^+ and electron species. Toren et al. [176] observed under H_2O electrolysis conditions that H_2 bubble diameter increase from 60.1 μm up to 70.6 μm at pH = 7 and pH = 3 values, respectively. We must stress out that Li_2SO_4 1.0 mol L^{-1} presented pH = 8.0. Therefore, this local pH variation onto cathode (negative pole) electrode NiO@MWCNTs, described by Reaction 3 can significantly increase the diameter of H_2 bubble obtained.

The local and prominent H_2 gas evolution also led to an increase of Li^+ and SO_4^{2-} diffusion into inner of NiO@MWCNTs cathode (negative pole) electrode as a result of Fick's Second Law, once that the dynamic of detached H_2 bubble plays a key role on the concentration profile along the nanostructure. For instance, the H_2 and Li^+ diffusion coefficient in aqueous medium were report as 10^{-5} cm^2 s^{-1} [177] and 10^{-8} cm^2 s^{-1} [179], respectively. These three magnitude orders higher for H_2 bubble than Li^+ values certainly induce an unbalanced charge and concentration species into NiO@MWCNTs cathode (negative pole) electrode. Einarsrud et al. [177] studied the numerical simulation of continuum scale electrochemical H_2 bubble evolution using the finite element method. The authors [177] observed that due to the larger rise velocity for the initial detachment process compared to the completed detached one, the drag force acting on the rising bubble in the former is larger, resulting in a bigger H_2 bubble deformation and, consequently, a smaller current. As the bubble detaches from the electrode surface, the convection established seems to drag the dissolved H_2 in the concentration boundary layer in the wake of the rising bubble. As a result, there is a change along with the profile concentration from the electrode surface to the top.

Although Li_2SO_4 is mainly soluble in an aqueous medium, we must stress that the monoclinic crystal structure observed under operando conditions presented herein is $Li_2SO_4 \cdot H_2O$ aqua-complex. This unit cell crystal structure consists of LiO_4 and SO_4 tetrahedra [168]. The SO_4 tetrahedra are regular (S-O distances in the range 1.470 - 1.478 Å) with single S-sites, as confirmed by X-ray diffraction [180], [181] and ^{33}S solid-state NMR [182]. There are two crystallographically different Li sites, one with regular and the other with more distorted O-Li-O tetrahedral angles. The structure refinement and the re-determination of exact H-positions in the H_2O of crystallisation were also carried out by several groups [183]–[185]. In addition to the two Li atoms and one S atom, the asymmetric part of the unit cell also contains five O atoms and two H atoms.

As described previously, the anodic sweep onto NiO@MWCNTs anode (positive pole) electrodes evolves local pH variation, O_2 gas evolution and electron (Reaction 2).

Consequently, it is possible to suggest that Li_2CO_3 can arise in Figure 14 (c) onto NiO@MWCNTs anode (positive pole) electrodes according to the reaction below:

$$2Li^{+} + 2\bar{e} + \uparrow \frac{1}{2} O_2 + \uparrow CO_2 \longrightarrow \downarrow Li_2CO_3 \qquad \text{Reaction 4}$$

where, CO_2 arise as MWCNT degradation due to harsh electrochemical conditions.

Several papers on literature [160], [186]–[188] has reported the CO and CO_2 gas evolution as a function of applied voltage in carbon-based electrochemical supercapacitors. Piñero et al. [186] observed the electrochemical response and gas evolution using DEMS (*Differential electrochemical mass spectrometry*) into carbon-based electrodes and Li_2SO_4 aqueous medium. According to the authors [186], at positive polarisation e.g. NiO@MWCNTs anode electrodes, approaching the thermodynamic potential for H_2O electrolysis, results in the evolution of CO_2 even before the evolution of O_2. Berg et al. [160] studied the ageing phenomena in high-voltage aqueous supercapacitors investigated by in-situ gas analysis using OEMS (*on-line* electrochemical mass spectrometry), enabling both quantitative and qualitative *in-situ* analysis of gaseous. According to the authors [160], at cell voltage $U > 0.6$ V activated carbon electrode oxidized into significant amounts of phenol, anhydride, lactone, quinone and carbonyl functional groups apparently oxidize early to form mainly CO_2 gas at cell voltage $U > 0.6$ V. The H_2 gas evolution starts close to the thermodynamic HER potentials ($U > 1.2$ V), but because of carbon surface group modification (phenol, anhydride, lactone, quinone, carbonyl functional groups) and hydrogen storage, significant H_2 gas evolution occurs first at cell voltage of $U > 1.6$ V. Therefore, as a result of abusive voltage applied and, consequently, CO_2 gas evolution as a result of MWCNTs oxidation, the Li_2CO_3 (Reaction 4) is obtained at NiO@MWCNTs anode (positive pole) electrodes.

The detection of CO_2 is pivotal as a precise indicator of supercapacitor operation limits because it reflects the surface degradation at the positive electrode and may further increase the overall cell impedance. For instance, the formation of gas bubbles at the current collector and/or inside the electrode pores introduce both electronic and ionic resistance by inducing electric contact loss and/or obstructing ionic transport, respectively. In this sense, several authors reported the CO_2 and its by-side reaction were reported using spectrometric techniques. Herein, *operando* Raman analyses were also investigated to analyse these systems and a sequence of chemical reaction steps as a function of the applied voltage is suggested.

4.2.2. *Raman spectra*

Figure 16 (a-b) shows the *operando* Raman spectra of MWCNT and NiO@MWCNTs electrodes, respectively. Operando Raman spectra display bands from Li_2SO_4 in the aqueous electrolyte at ~983 cm^{-1}; $Li_2SO_4{\cdot}H_2O$ at 1010 cm^{-1}; Li_2CO_3 at 1088 cm^{-1} as described by reference [189] and carbon: D (~1317 cm^{-1}), G (~1580 cm^{-1}), D' (~1616 cm^{-1}), G' (~2632 cm^{-1}) and D*(~1480 cm^{-1}), which are described elsewhere [105].

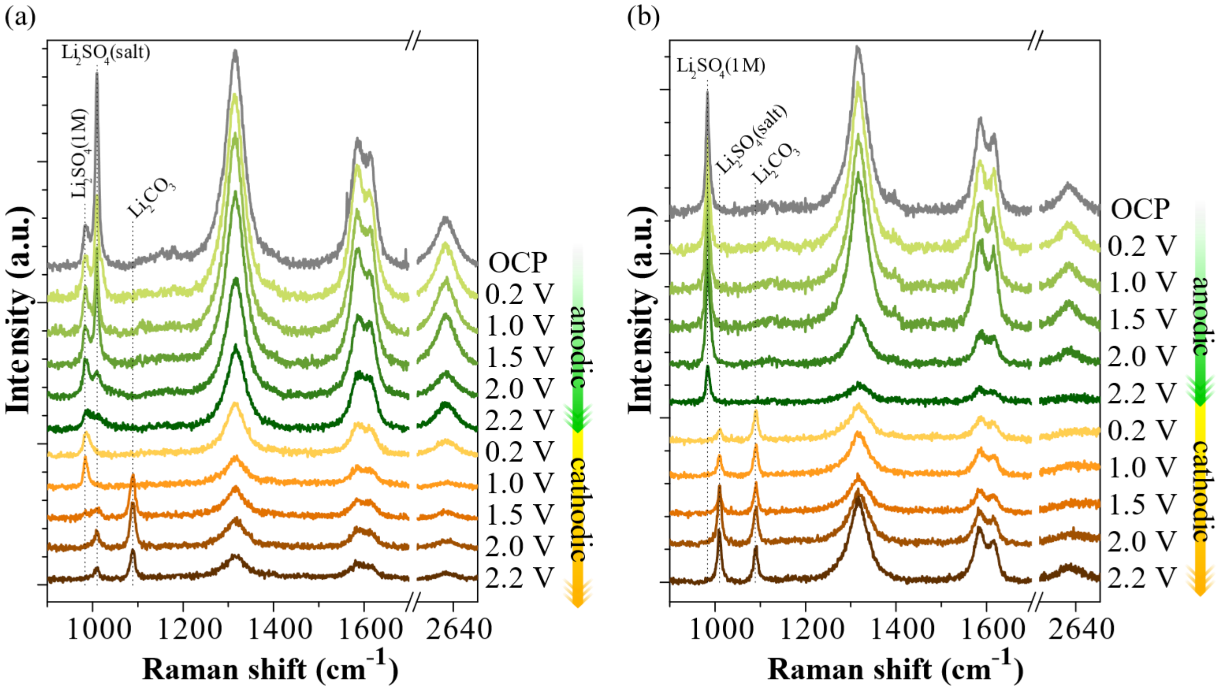

Figure 16. *Operando* Raman from a) MWCNT and b) NiO@MWCNTs from 0.0 - 2.2 V. Spectra were taken from electrode inside symmetrical coin-cell. Li_2SO_4 1.0 mol L^{-1} aqueous medium and 25 °C. Raman spectra were performed using a 785 nm excitation wavelength and focused on a 50× objective lens.

As expected, $Li_2SO_4{\cdot}H_2O$ Raman bands were detected onto NiO@MWCNTs cathode (negative pole) where H_2 gas evolution takes place. On contrary, Li_2CO_3 Raman bands were detected onto NiO@MWCNTs anode (positive pole) where O_2 gas evolution takes place. Even without NiO nanoparticles it was expected once that it is well known the H_2 [190]–[192] and O_2 [193]–[195] onto carbon-based electrodes (graphene, graphite, glassy Carbon, pyrolytic Carbon). The $Li_2SO_4 \cdot H_2O$ and Li_2CO_3 bands observed using *operando* Raman spectroscopy and not under XRD analysis are related to the design of the coin-cell onto sample-holder (electrode exposed surface) and the flux of incident beam.

Concerning MWCNTs structure, the G-band is an E_{2g} optical mode centered at 1582 cm^{-1}, originated by doubly degenerate vibrational mode of iLO (in-plane longitudinal optical) and iTO (in-plane transversal optical) phonon branches crossing at the Γ point in the graphite first Brillouin zone [105]. D-band is originated from the breathing modes of six-atom rings, associated with the LO (longitudinal optical) phonon at the K point of the Brillouin zone. D- and D’-bands originated by intervalley and intravalley double-resonance processes, respectively, involving a phonon and a defect [105]. G’-band at ~2632 cm^{-1} is the D-band overtone originated from an intervalley double-resonance process involving two-phonon. D^* is associated with oxygen functional groups onto carbon surface [196]. An electronic and structural study of MWCNTs and NiO@MWCNTs dynamic along the anodic polarization is observed in Figure 17.

It is possible to noticed in Figure 17 (a-b) that all carbon bands (D, G, D', G'and D*) reduced its intensities during anodic polarization onto cathode (negative pole) and anode (positive pole), which is a strong evidence of H_2 and O_2 gas evolution at electrode-electrolyte interface, and consequently diffusing signal beam. Such effect is related to Tyndall effect [197].

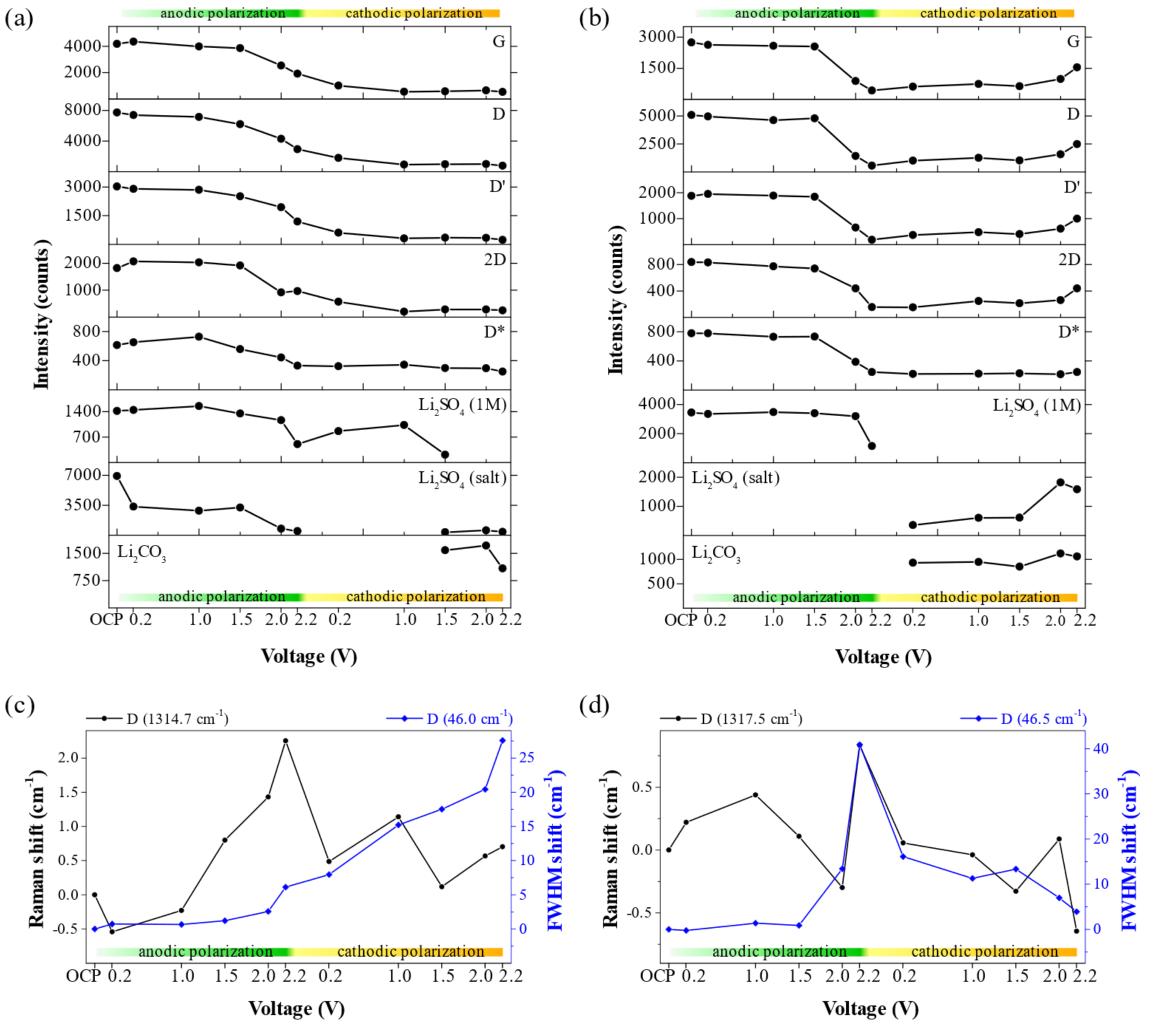

Figure 17. MWCNTs spectroscopy parameter as a) intensity and; c) position and FWHM shift of D-band. NiO@MWCNTs spectroscopy parameter as b) intensity and; d) position and FWHM shift of D-band. Spectra were taken from electrode inside symmetrical coin-cell, Li_2SO_4 1.0 mol L^{-1} aqueous medium and 25 ^oC.

We must note that under the abusive regime, and consequently O_2 and H_2 gas evolution, MWCNTs were partially oxidized and converted into CO_2. Liu et al. studied the [197] effect of ultrasonic processing time (30 up to 240 minutes) onto solvothermal-assisted liquid-phase exfoliation of large size and high-quality black phosphorus. According to the authors [197], Tyndall effect was observed in the solvent with different ultrasonic time, and this phenomenon indicated that the dispersions have good dispersity and homogeneity for black phosphorus nanosheets. Only a slightly voltage onset towards lower values for the decrease of all carbon bands (G, D, D', G' and D*) were pronounced for NiO@MWCNT compared to MWCNT, which are related to the higher catalytic effect of H_2O electrolysis onto NiO@MWCNT compared to MWCNT as already reported for our research group previously [162]. As expected, $Li_2SO_4{\cdot}H_2O$ bands were observed for both cathode (negative pole) and anode (positive pole) into MWCNTs and NiO@MWCNT, once that precursor species were presented on the electrolyte. However, as discussed previously, the Li_2CO_3 crystal phase are related to the O_2 and CO_2 gas evolution (Reaction 4), as a result, its bands were pronounced at the anode (positive pole) for both MWCNTs (Figure 17 (a)) and NiO@MWCNT (Figure 17 (b)) *operando* Raman spectra.

As can be observed in Figure 17 (a-b), the D'-band related to Carbon nanostructured defects decrease significantly at the cathode (negative pole) compared to the anode (positive pole) for both MWCNT and NiO@MWCNTs electrodes. A similar profile was exhibited by D*-band related to oxygen functional groups created along with Carbon nanostructured materials, also for both MWCNT and NiO@MWCNTs electrodes. Moreover, for D*-band, its decreasing is pronounced at the cathode (negative pole) and almost constant at low values at the anode (positive pole). We must point out that this fast decrease for D’-band and D*-band are both in-phase and their fast decreasing are related to H_2 gas evolution. At abusive voltage probed onto cathode (negative pole) electrode, the O_2 gas evolution converted carbon-based materials into several oxygen functional groups. As a result, the D*-band values remain constant. Similar results were observed for both MWCNT and NiO@MWCNTs electrodes. However, as O_2 gas evolution is higher at NiO@MWCNTs than MWCNTs electrodes, as already reported previously [162], the plateau observed for D*-band into NiO@MWCNTs electrodes (Figure 17 (b)) is larger and presented lower values.

In neutral solutions, the hydration of NiO and the redox activity of the Ni-species under anodic polarization conditions can be represented by the following mechanism adapted from Bode's model [198], [199]:

$$NiO + H_2O \leftrightharpoons NiO(OH)_2 \qquad \text{Reaction 5}$$

$$\alpha\text{-}Ni(OH)_2 + OH^- \longrightarrow \gamma\text{-}NiOOH + H_2O + \bar{e} \qquad \text{Reaction 6}$$

Also, the decomposition of Li_2CO_3 can be observed.

$$Li_2CO_3 + H_2O \longrightarrow 2Li^+ + HCO_3^- + OH^- \qquad \text{Reaction 7}$$

As a consequence of anodic polarization conditions observed for NiO materials used in supercapacitor devices, the NiO is converted into α-Ni(OH)$_2$. The promising and lamellar structure for supercapacitor Li-intercalation obtained is γ-NiOOH. As described in Reactions 5 & 6, the γ-NiOOH as a product lead to consumption of OH$^-$ species. In consequence of chemical equilibrium conditions of OH- consumption, the Li_2CO_3 is decomposed in an aqueous medium into HCO_3^- (Reaction 7) and further H_2O and CO_2. Once all this chemical equilibrium is envolving NiO materials are observed only into NiO@MWCNTs materials, it is possible to notice only an increase in FWHM values related for MWCNT materials for cathode (negative pole) followed by the anode (positive pole) in Figure 17 (c). On the other hand, for NiO@MWCNTs materials, it is possible to notice a competitive chemical equilibrium involving O_2 and CO_2 gas evolution followed by Li_2CO_3 product (Reaction 4) and its decomposition (Reaction 7). Therefore, as observed in Figure 17 (d), under the cathode (negative pole) regime and consequently H_2 gas evolution, it is possible to notice a hipsochromic shift and increase FWHM values. However, under the anode (positive pole) regime and consequently O_2 gas evolution, it is possible to notice a bathochromic shift (related to chemical equilibrium between Reaction 4 & 7) and decrease FWHM values. Notwithstanding, such chemical equilibrium between is not present in MWCNT materials, and due to the absence of NiO nanoparticles (Reaction 5 & 6), only an increase in the FWHM is observed, as noticed in Figure 17 (c).

In sumary, a overal scenario of abusive voltage for MWCNT and NiO@MWCNTs symmetric coin-cell is pictured in Figure 18. The whole dynamic process for such supercapacitor operation in the harsh condition is described as: OCP starting operating, carbon-based electrode oxidation (oxygen functional groups and further CO_2 gas evolution), O_2 gas evolution under anode (positive pole) electrode, Li_2CO_3 crystal structure obtained, H_2 gas evolution under cathode (negative pole) electrode, and finally $Li_2SO_4 \cdot H_2O$ crystal structure obtained.

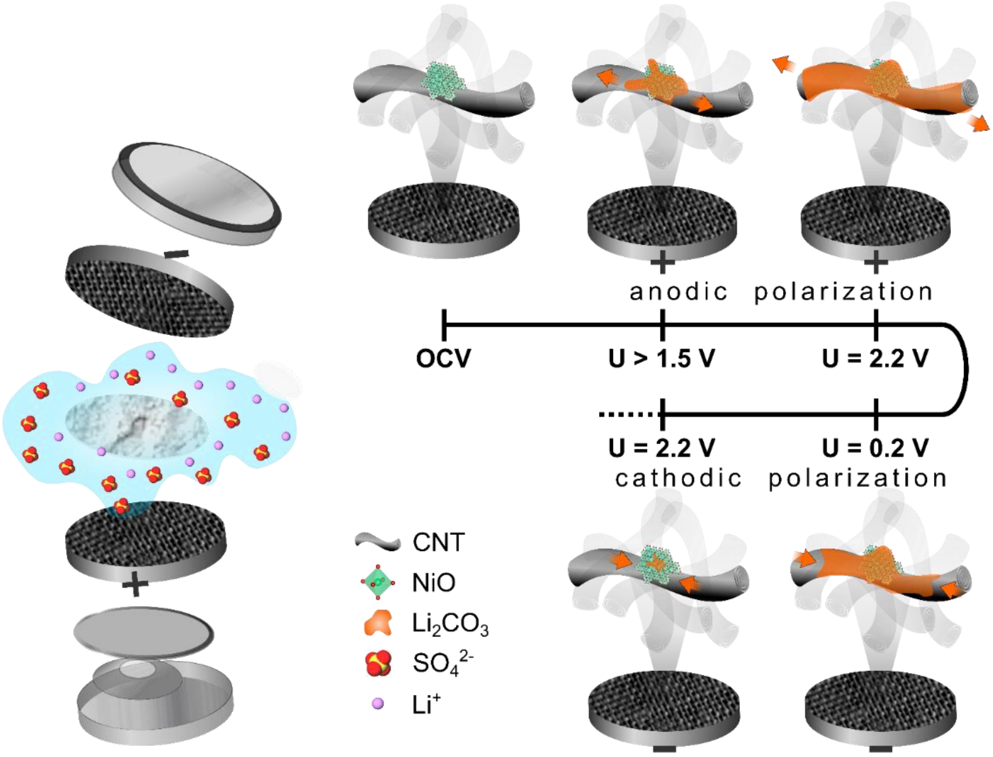

Figure 18. Scheme showing formation and the consumption of Li_2CO_3 into MWCNT surface catalyzed by NiO nanoparticles at different voltage applied in the symmetrical coin-cell. Li_2SO_4 1.0 mol L^{-1} aqueous medium and 25 ^oC.

After all, the *operando* Raman spectroscopy is also a powerful tool for investigating gas evolution (H_2, O_2 and CO_2) and species e.g., Li_2CO_3 and Li_2SO_4·H2O with drastically influence the supercapacitor performance.

4.3. Conclusions

We have been reporting on failure reasons due to voltage cell abuse. We tracked electrodes by operando XRD diffraction pattern in symmetrical coin cells filled with 1M Li_2SO_4 aqueous electrolyte. We first investigated the CNT system, then investigated the effect of CNT decorated with NiO nanoparticles as electrodes for supercapacitors. Carbon electrodes oxidize and internal pressure increase to critical levels open-up the coin cells. This failure is justified by CO_2 forming at the electrode and electrolyte interface. XRD pattern does not evidence any structural changes on the carbon electrode surface. On the other hand, XRD pattern from the NiO@CNT evidence formation of Li_2CO_3. The most probable origin of Li_2CO_3 is from CO_2 evolution from CNT electrode and Li^+ ions from the electrolyte, catalyzed by NiO nanoparticles. The Li_2CO_3 is interesting reversible on the full range cell scan, exploring filters (signals processing) and energy storage applications. The CO_2 evolution causes cell failure due to fatal internal pressure. It is mandatory to respect the cell voltage to a long lifespan and misleading on reporting energy storage in electrochemical supercapacitor.

5. CONCLUDING REMARKS

Self-supported and flexible electrodes were successfully developed by the use of buckypaper electrodes followed by a systematic and advanced study to determine the correct working voltage window (WVW) for supercapacitors using different electrochemical techniques and finally an operating study of electrochemical capacitors when the WVW is extrapolated under abuse mode.

The buckypaper electrodes composed of mixtures containing Activated Carbon (AC) and multi-walled carbon nanotubes (MWCNT) is presented as a binder-free, self-supported, and flexible high-surface-area material alternative. This composite is current collector free, which avoids corrosion processes in the electrode, it can be welded with metallic connectors and have high electronic contact. The MWCNT:AC composite simultaneously provides several electron transport pathways and large specific surface area due to properties of MWCNT and AC respectively. The contribution of the material AC permitted an increase of the capacitance from 7.6 to 51.7 F g^{-1} for the ratio of 1:3 (MWCNT:AC) compared to a composite containing only MWCNT at a high WVW of 1.4 V. The electrode composed presented a great cyclability stability with 93% capacitance retention after one million cycles being a promising candidate for applications in aqueous-based supercapacitors.

During the electrochemical analysis of this material, the need for a systematic study to determine the WVW emerged. This inspired a study to investigate the correct potential window for aqueous-based systems. From this study, a scientific routine was presented to better determine the correct capacitive working voltage window for supercapacitors. We note that although there is a pronounced capacitive characteristic in the voltammetric study (when observing a quasi-rectangular shaped voltammograms) it is necessary to evaluate several electrochemical figures-of-merit to determine the correct WVW and not just the voltammetric curve because it can mask the parasitic occurrence of the Faradaic water-splitting process. Therefore, complementary studies such as galvanostatic charge–discharge (GCD) chronoamperometry (CA) and the electrochemical impedance spectroscopy (EIS) in addition to cyclic voltammetry (CV) are recommended techniques to be used together for the interpretation of a reliable electrochemical characterization of supercapacitors. The incorrect characterization of WVW, for higher voltages, promotes the water-splitting process, shortening the life cycle and damaging the device. Thus, the correct determination of WVW contributes to the stable operation of charge storage processes in electrochemical supercapacitor systems.

Knowing the ideal voltage window for the supercapacitor to work we aim to investigate the behavior of the system when applying voltage cell abuse. In a symmetric device with CNT electrodes and electrodes of CNT decorated with NiO nanoparticles filled with 1M Li_2SO_4 we observed failures starting at voltages of 1.5 V with increasing internal pressure due to the evolution of gases causing open-up the coin cell. The application of higher voltages contributes to the carbon electrode oxidize and evolving CO_2 at the electrode and electrolyte interface. Operating XRD diffraction pattern from the NiO@CNT evidence formation of Li_2CO_3 probably originated from the evolution of CO_2 from the decomposition of the CNT electrode combined with the Li^+ ions of the electrolyte catalyzed by the NiO nanoparticles. Operando Raman supports this information that also demonstrate the formation of Li_2CO_3. Another important point observed here is the reversibility of the process with the decomposition of Li_2CO_3 initially formed, this process occurs in the presence of NiO which performs as a catalyst in the formation process as well as the decomposition of Li_2CO_3. Therefore, it is important to respect the correct cell voltage for a long lifespan and to avoid damage to the cell during energy storage in electrochemical supercapacitor.

BIBLIOGRAPHY

[1] N. Kularatna, “Energy Storage Devices for Electronic Systems: Rechargeable Batteries and Supercapacitors,” *Energy Storage Devices Electron. Syst. Recharg. Batter. Supercapacitors*, pp. 1–267, Nov. 2014, doi: 10.1016/C2012-0-06356-9.

[2] V. S. Bagotsky, A. M. Skundin, and Y. M. Volfkovich, “Electrochemical Power Sources: Batteries, Fuel Cells, and Supercapacitors,” *Electrochem. Power Sources Batter. Fuel Cells, Supercapacitors*, pp. 1–374, Jan. 2015, doi: 10.1002/9781118942857.

[3] A. Yu, V. Chabot, and J. Zhang, “Electrochemical supercapacitors for energy storage and delivery: Fundamentals and applications,” *Electrochem. Supercapacitors Energy Storage Deliv. Fundam. Appl.*, pp. 1–355, Jan. 2017, doi: 10.1201/B14671.

[4] C. Antônio Rufino Júnior, E. R. Sanseverino, P. Gallo, D. Koch, H. G. Schweiger, and H. Zanin, “Blockchain review for battery supply chain monitoring and battery trading,” *Renew. Sustain. Energy Rev.*, vol. 157, p. 112078, Apr. 2022, doi: 10.1016/J.RSER.2022.112078.

[5] C. A. Rufino Júnior *et al.*, “Towards a business model for second-life batteries – barriers, opportunities, uncertainties, and technologies,” *J. Energy Chem.*, vol. 78, pp. 507–525, Mar. 2023, doi: 10.1016/J.JECHEM.2022.12.019.

[6] V. S. Carvalho *et al.*, “Radially ordered carbon nanotubes performance for Li-O2 batteries: Pre-treatment influence on capacity and discharge products,” *Catal. Today*, vol. 348, pp. 299–306, May 2020, doi: 10.1016/J.CATTOD.2019.09.030.

[7] C. G. Real, E. H. N. S. Thaines, L. A. Pocrifka, R. G. Freitas, G. Singh, and H. Zanin, “Freestanding niobium pentoxide-decorated multiwalled carbon nanotube electrode: Charge storage mechanism in sodium-ion pseudocapacitor and battery,” *J. Energy Storage*, vol. 52, p. 104793, Aug. 2022, doi: 10.1016/J.EST.2022.104793.

[8] M. A. Scibioh and B. Viswanathan, “Materials for supercapacitor applications,” *Mater. Supercapacitor Appl.*, pp. 1–400, Jan. 2020, doi: 10.1016/C2019-0-00454-2.

[9] R. Vicentini *et al.*, “Ragone Plots for Electrochemical Double-Layer Capacitors,” *Batter. Supercaps*, vol. 4, no. 8, pp. 1291–1303, Aug. 2021, doi:

10.1002/BATT.202100093.

[10] J. G. Wang, F. Kang, and B. Wei, “Engineering of MnO2-based nanocomposites for high-performance supercapacitors,” *Prog. Mater. Sci.*, vol. 74, pp. 51–124, Oct. 2015, doi: 10.1016/J.PMATSCI.2015.04.003.

[11] P. Simon, T. Brousse, and F. Favier, *Supercapacitors based on carbon or pseudocapacitive materials*. 2017.

[12] T. S. Mathis, N. Kurra, X. Wang, D. Pinto, P. Simon, and Y. Gogotsi, “Energy Storage Data Reporting in Perspective—Guidelines for Interpreting the Performance of Electrochemical Energy Storage Systems,” *Adv. Energy Mater.*, vol. 9, no. 39, p. 1902007, Oct. 2019, doi: 10.1002/AENM.201902007.

[13] B. E. Conway, “Electrochemical Supercapacitors,” *Electrochem. Supercapacitors*, 1999, doi: 10.1007/978-1-4757-3058-6.

[14] A. J. Paulista Neto, D. A. C. Da Silva, V. A. Gonçalves, H. Zanin, R. G. Freitas, and E. E. Fileti, “An evaluation of the capacitive behavior of supercapacitors as a function of the radius of cations using simulations with a constant potential method,” *Phys. Chem. Chem. Phys.*, vol. 24, no. 5, pp. 3280–3288, Feb. 2022, doi: 10.1039/D1CP04350A.

[15] O. Vitor Silva Moreira *et al.*, “Diamond and Carbon Nanotube Composites for Supercapacitor Devices,” doi: 10.1007/s11664-016-5010-7.

[16] J. Pedro Aguiar dos Santos *et al.*, “Ion dynamics into different pore size distributions in supercapacitors under compression,” *J. Energy Chem.*, vol. 80, pp. 110–119, May 2023, doi: 10.1016/J.JECHEM.2022.12.063.

[17] C. G. M. Real *et al.*, “Electric double layer capacitors prepared with polyvinyl alcohol and multi-walled carbon nanotubes,” *SAE Tech. Pap.*, no. September, Sep. 2018, doi: 10.4271/2018-36-0313.

[18] M. Alexandreli *et al.*, “Pseudocapacitive behaviour of iron oxides supported on carbon nanofibers as a composite electrode material for aqueous-based supercapacitors,” *J. Energy Storage*, vol. 42, p. 103052, Oct. 2021, doi: 10.1016/J.EST.2021.103052.

[19] W. G. Nunes *et al.*, “Pseudo-capacitive behavior of multi-walled carbon nanotubes decorated with nickel and manganese (hydr)oxides nanoparticles,” *J. Energy Storage*, vol. 31, p. 101583, Oct. 2020, doi: 10.1016/J.EST.2020.101583.

[20] W. G. Nunes *et al.*, “Electrochemical Behavior of Symmetric Electrical Double-Layer Capacitors and Pseudocapacitors and Identification of Transport Anomalies in the Interconnected Ionic and Electronic Phases Using the Impedance Technique,” *Nanomater. 2022, Vol. 12, Page 676*, vol. 12, no. 4, p. 676, Feb. 2022, doi: 10.3390/NANO12040676.

[21] B. M. Pires *et al.*, “Characterization of porous cobalt hexacyanoferrate and activated carbon electrodes under dynamic polarization conditions in a sodium-ion pseudocapacitor,” *J. Energy Chem.*, vol. 54, pp. 53–62, Mar. 2021, doi: 10.1016/J.JECHEM.2020.05.045.

[22] B. Freitas *et al.*, “Robust, flexible, freestanding and high surface area activated carbon and multi-walled carbon nanotubes composite material with outstanding electrode properties for aqueous-based supercapacitors,” *Mater. Adv.*, vol. 2, no. 13, pp. 4264–4276, Jul. 2021, doi: 10.1039/D0MA00783H.

[23] C. G. M. Real *et al.*, “Polyacrylonitrile and activated carbon composite for electric double layer capacitors,” *SAE Tech. Pap.*, no. September, Sep. 2018, doi: 10.4271/2018-36-0310.

[24] A. G. dos Santos Neto *et al.*, “Electrochemical sensor for detection of imipramine antidepressant at low potential based on oxidized carbon nanotubes, ferrocenecarboxylic acid, and cyclodextrin: application in psychotropic drugs and urine samples,” *J. Solid State Electrochem.*, vol. 22, no. 5, pp. 1385–1394, May 2018, doi: 10.1007/S10008-017-3772-3/TABLES/1.

[25] R. Venâncio, R. Vicentini, L. H. Costa, R. Teófilo, L. M. Da Silva, and H. Zanin, “In-situ electrochemical and operando Raman techniques to investigate the effect of porosity in different carbon electrodes in organic electrolyte supercapacitors,” *J. Energy Storage*, vol. 50, p. 104219, Jun. 2022, doi: 10.1016/J.EST.2022.104219.

[26] C. G. Real *et al.*, “Analyses of dispersive effects and the distributed capacitance in the time and frequency domains of activated carbon nanofiber electrodes as symmetric supercapacitors,” *Electrochim. Acta*, vol. 402, p. 139299, Jan. 2022, doi: 10.1016/J.ELECTACTA.2021.139299.

[27] R. Vicentini *et al.*, “Multi-walled carbon nanotubes and activated carbon composite material as electrodes for electrochemical capacitors,” *J. Energy Storage*, vol. 33, p.

100738, Jan. 2021, doi: 10.1016/J.EST.2019.04.012.

[28] M. M. Amaral, M. J. Pinzón C., A. C. Peterlevitz, C. A. Rufino Júnior, L. M. Da Silva, and H. Zanin, “Robust, freestanding, and bendable multi-walled carbon nanotube buckypapers as electrode materials for quasi-solid-state potassium-ion supercapacitors,” *Diam. Relat. Mater.*, vol. 115, p. 108354, May 2021, doi: 10.1016/J.DIAMOND.2021.108354.

[29] R. Vicentini *et al.*, “Environmentally friendly functionalization of porous carbon electrodes for aqueous-based electrochemical capacitors,” *IEEE Trans. Nanotechnol.*, vol. 18, pp. 73–82, 2019, doi: 10.1109/TNANO.2018.2878663.

[30] M. J. Pinzón C., J. M. de Aquino, R. G. Freitas, G. A. Pereira, L. M. Da Silva, and H. Zanin, “A comprehensive study about the influence of pore structures of carbon-based electrode materials on the charge-storage processes of water-in-salt based supercapacitors,” *J. Energy Storage*, vol. 62, p. 106858, Jun. 2023, doi: 10.1016/J.EST.2023.106858.

[31] R. Vicentini, R. Venâncio, W. Nunes, L. M. Da Silva, and H. Zanin, “New Insights on the Sodium Water-in-Salt Electrolyte and Carbon Electrode Interface from Electrochemistry and Operando Raman Studies,” *ACS Appl. Mater. Interfaces*, vol. 13, no. 51, pp. 61139–61153, Dec. 2021, doi: 10.1021/ACSAMI.1C18777/ASSET/IMAGES/MEDIUM/AM1C18777_M010.GIF.

[32] M. M. Amaral *et al.*, “Direct observation of the CO2 formation and C–H consumption of carbon electrode in an aqueous neutral electrolyte supercapacitor by in-situ FTIR and Raman,” *J. Energy Chem.*, vol. 71, pp. 488–496, Aug. 2022, doi: 10.1016/J.JECHEM.2022.03.020.

[33] N. A. Zambianco *et al.*, “Determination of tadalafil in pharmaceutical samples by vertically oriented multi-walled carbon nanotube electrochemical sensing device,” *J. Electroanal. Chem.*, vol. 877, p. 114501, Nov. 2020, doi: 10.1016/J.JELECHEM.2020.114501.

[34] R. Vicentini *et al.*, “Direct growth of mesoporous Carbon on aluminum foil for supercapacitors devices,” *J. Mater. Sci. Mater. Electron.*, vol. 29, no. 12, pp. 10573–10582, Jun. 2018, doi: 10.1007/S10854-018-9121-1/FIGURES/9.

[35] L. H. Costa, R. Vicentini, T. Almeida Silva, D. Vilela Franco, L. Morais Da Silva, and

H. Zanin, “Identification and quantification of the distributed capacitance and ionic resistance in carbon-based supercapacitors using electrochemical techniques and the analysis of the charge-storage dynamics,” *J. Electroanal. Chem.*, vol. 929, p. 117140, Jan. 2023, doi: 10.1016/J.JELECHEM.2022.117140.

[36] J. P. A. Santos *et al.*, “Boosting energy-storage capability in carbon-based supercapacitors using low-temperature water-in-salt electrolytes,” *J. Energy Chem.*, vol. 70, pp. 521–530, Jul. 2022, doi: 10.1016/J.JECHEM.2022.02.055.

[37] M. M. Amaral, R. Venâncio, A. C. Peterlevitz, and H. Zanin, “Recent advances on quasi-solid-state electrolytes for supercapacitors,” *J. Energy Chem.*, vol. 67, pp. 697–717, Apr. 2022, doi: 10.1016/J.JECHEM.2021.11.010.

[38] W. G. Nunes, B. G. A. Freitas, R. M. Beraldo, R. M. Filho, L. M. Da Silva, and H. Zanin, “A rational experimental approach to identify correctly the working voltage window of aqueous-based supercapacitors,” *Sci. Reports 2020 101*, vol. 10, no. 1, pp. 1–9, Nov. 2020, doi: 10.1038/s41598-020-75851-7.

[39] D. A. C. Da Silva, A. J. Paulista Neto, A. M. Pascon, E. E. Fileti, L. R. C. Fonseca, and H. G. Zanin, “Combined density functional theory and molecular dynamics simulations to investigate the effects of quantum and double-layer capacitances in functionalized graphene as the electrode material of aqueous-based supercapacitors,” *J. Phys. Chem. C*, vol. 125, no. 10, pp. 5518–5524, Mar. 2021, doi: 10.1021/ACS.JPCC.0C11602/ASSET/IMAGES/LARGE/JP0C11602_0008.JPEG.

[40] J. Pedro Aguiar dos Santos *et al.*, “Best practices for electrochemical characterization of supercapacitors,” *J. Energy Chem.*, vol. 80, pp. 265–283, May 2023, doi: 10.1016/J.JECHEM.2022.12.034.

[41] D. A. C. Da Silva *et al.*, “Effect of conductivity, viscosity, and density of water-in-salt electrolytes on the electrochemical behavior of supercapacitors: molecular dynamics simulations and in situ characterization studies,” *Mater. Adv.*, vol. 3, no. 1, pp. 611–623, Jan. 2022, doi: 10.1039/D1MA00890K.

[42] D. M. Soares, R. Vicentini, A. C. Peterlevitz, C. B. Rodella, L. M. da Silva, and H. Zanin, “Tungsten oxide and carbide composite synthesized by hot filament chemical deposition as electrodes in aqueous-based electrochemical capacitors,” *J. Energy Storage*, vol. 26, p. 100905, Dec. 2019, doi: 10.1016/J.EST.2019.100905.

[43] L. C. C. B. Oliveira *et al.*, “Reviewing perovskite oxide sites influence on electrocatalytic reactions for high energy density devices,” *J. Energy Chem.*, Feb. 2023, doi: 10.1016/J.JECHEM.2023.02.013.

[44] W. G. Nunes *et al.*, “Charge-storage mechanism of highly defective NiO nanostructures on carbon nanofibers in electrochemical supercapacitors,” *Nanoscale*, vol. 13, no. 21, pp. 9590–9605, Jun. 2021, doi: 10.1039/D1NR00065A.

[45] J. J. S. Teles *et al.*, “Supercapacitive properties, anomalous diffusion, and porous behavior of nanostructured mixed metal oxides containing Sn, Ru, and Ir,” *Electrochim. Acta*, vol. 295, pp. 302–315, Feb. 2019, doi: 10.1016/J.ELECTACTA.2018.10.131.

[46] R. Vicentini *et al.*, “Niobium pentoxide nanoparticles decorated graphene as electrode material in aqueous-based supercapacitors: Accurate determination of the working voltage window and the analysis of the distributed capacitance in the time domain,” *J. Energy Storage*, vol. 44, p. 103371, Dec. 2021, doi: 10.1016/J.EST.2021.103371.

[47] W. G. Nunes *et al.*, “Operando Raman spectroelectrochemical study of polyaniline degradation: A joint experimental and theoretical analysis,” *J. Energy Storage*, vol. 55, p. 105770, Nov. 2022, doi: 10.1016/J.EST.2022.105770.

[48] E. Frackowiak, “Electrode Materials with Pseudocapacitive Properties,” *Supercapacitors Mater. Syst. Appl.*, pp. 207–237, 2013, doi: 10.1002/9783527646661.ch6.

[49] D. A. C. Da Silva, A. J. Paulista Neto, A. M. Pascon, E. E. Fileti, L. R. C. Fonseca, and H. G. Zanin, “Exploring doped or vacancy-modified graphene-based electrodes for applications in asymmetric supercapacitors,” *Phys. Chem. Chem. Phys.*, vol. 22, no. 7, pp. 3906–3913, Feb. 2020, doi: 10.1039/C9CP06495H.

[50] D. M. Soares *et al.*, “Additive Manufacturing of Electrochemical Energy Storage Systems Electrodes,” *Adv. Energy Sustain. Res.*, vol. 2, no. 5, p. 2000111, May 2021, doi: 10.1002/AESR.202000111.

[51] P. Ratajczak, K. Jurewicz, and F. Béguin, “Factors contributing to ageing of high voltage carbon/carbon supercapacitors in salt aqueous electrolyte,” *J. Appl. Electrochem.*, vol. 44, no. 4, pp. 475–480, 2014, doi: 10.1007/s10800-013-0644-0.

[52] C. Merlet *et al.*, “On the molecular origin of supercapacitance in nanoporous carbon electrodes,” *Nat. Mater.*, vol. 11, no. 4, pp. 306–310, 2012, doi: 10.1038/nmat3260.

[53] M. Salanne *et al.*, “Efficient storage mechanisms for building better supercapacitors,” *Nat. Energy*, vol. 1, no. 6, p. 16070, 2016, doi: 10.1038/nenergy.2016.70.

[54] P. Simon and Y. Gogotsi, “Materials for electrochemical capacitors,” *Nat. Mater.*, vol. 7, no. 11, pp. 845–854, 2008, doi: 10.1038/nmat2297.

[55] H. Helmholtz, “Ueber einige Gesetze der Vertheilung elektrischer Ströme in körperlichen Leitern, mit Anwendung auf die thierisch-elektrischen Versuche (Schluss.),” *Ann. Phys.*, vol. 165, no. 7, pp. 353–377, May 1853, doi: 10.1002/andp.18531650702.

[56] B. Lobato, L. Suárez, L. Guardia, and T. A. Centeno, “Capacitance and surface of carbons in supercapacitors,” *Carbon N. Y.*, vol. 122, pp. 434–445, 2017, doi: 10.1016/j.carbon.2017.06.083.

[57] J. Chmiola, G. Yushin, Y. Gogotsi, C. Portet, P. Simon, and P. L. Taberna, “Anomalous increase in carbon at pore sizes less than 1 nanometer,” *Science (80-.).*, vol. 313, no. 5794, pp. 1760–1763, 2006, doi: 10.1126/science.1132195.

[58] H. Shao, Y.-C. Wu, Z. Lin, P.-L. Taberna, and P. Simon, “Nanoporous carbon for electrochemical capacitive energy storage,” *Chem. Soc. Rev.*, pp. 3005–3039, 2020, doi: 10.1039/d0cs00059k.

[59] L. L. Zhang and X. S. Zhao, “Carbon-based materials as supercapacitor electrodes,” *Chem. Soc. Rev.*, vol. 38, no. 9, pp. 2520–2531, 2009, doi: 10.1039/B813846J.

[60] L. A. Malley *et al.*, “CHRONIC TOXICITY AND ONCOGENICITY OF N-METHYLPYRROLIDONE (NMP) IN RATS AND MICE BY DIETARY ADMINISTRATION,” *Drug Chem. Toxicol.*, vol. 24, no. 4, pp. 315–338, 2001, doi: 10.1081/DCT-100106262.

[61] C. Zhong, Y. Deng, W. Hu, J. Qiao, L. Zhang, and J. Zhang, “A review of electrolyte materials and compositions for electrochemical supercapacitors,” *Chem. Soc. Rev.*, vol. 44, no. 21, pp. 7484–7539, 2015, doi: 10.1039/C5CS00303B.

[62] C. Arbizzani, S. Beninati, M. Lazzari, F. Soavi, and M. Mastragostino, “Electrode materials for ionic liquid-based supercapacitors,” *13th Int. Meet. Lithium Batter.*, vol.

174, no. 2, pp. 648–652, 2007, doi: 10.1016/j.jpowsour.2007.06.162.

[63] Z. Li, J. Liu, K. Jiang, and T. Thundat, "Carbonized nanocellulose sustainably boosts the performance of activated carbon in ionic liquid supercapacitors," *Nano Energy*, vol. 25, pp. 161–169, 2016, doi: 10.1016/j.nanoen.2016.04.036.

[64] K. L. Van Aken, M. Beidaghi, and Y. Gogotsi, "Formulation of Ionic-Liquid Electrolyte To Expand the Voltage Window of Supercapacitors," *Angew. Chemie Int. Ed.*, vol. 54, no. 16, pp. 4806–4809, Jun. 2015, doi: 10.1002/anie.201412257.

[65] F. Béguin, V. Presser, A. Balducci, and E. Frackowiak, "Carbons and Electrolytes for Advanced Supercapacitors," *Adv. Mater.*, vol. 26, no. 14, pp. 2219–2251, Jun. 2014, doi: 10.1002/adma.201304137.

[66] C. Portet, G. Yushin, and Y. Gogotsi, "Electrochemical performance of carbon onions, nanodiamonds, carbon black and multiwalled nanotubes in electrical double layer capacitors," *Carbon N. Y.*, vol. 45, no. 13, pp. 2511–2518, 2007, doi: 10.1016/j.carbon.2007.08.024.

[67] N. Jung *et al.*, "Synthesis of Chemically Bonded Graphene/Carbon Nanotube Composites and their Application in Large Volumetric Capacitance Supercapacitors," *Adv. Mater.*, vol. 25, no. 47, pp. 6854–6858, Jun. 2013, doi: 10.1002/adma.201302788.

[68] M. F. El-Kady, Y. Shao, and R. B. Kaner, "Graphene for batteries, supercapacitors and beyond," *Nat. Rev. Mater.*, vol. 1, no. 7, p. 16033, 2016, doi: 10.1038/natrevmats.2016.33.

[69] D. Li, M. B. Müller, S. Gilje, R. B. Kaner, and G. G. Wallace, "Processable aqueous dispersions of graphene nanosheets," *Nat. Nanotechnol.*, vol. 3, no. 2, pp. 101–105, 2008, doi: 10.1038/nnano.2007.451.

[70] H. Sun *et al.*, "Hierarchical 3D electrodes for electrochemical energy storage," *Nat. Rev. Mater.*, vol. 4, no. 1, pp. 45–60, 2019, doi: 10.1038/s41578-018-0069-9.

[71] Z. Yang, J. Tian, Z. Yin, C. Cui, W. Qian, and F. Wei, "Carbon nanotube- and graphene-based nanomaterials and applications in high-voltage supercapacitor: A review," *Carbon N. Y.*, vol. 141, pp. 467–480, 2019, doi: 10.1016/j.carbon.2018.10.010.

[72] E. D. Walsh *et al.*, "Dry-Processed, Binder-Free Holey Graphene Electrodes for

Supercapacitors with Ultrahigh Areal Loadings," *ACS Appl. Mater. Interfaces*, vol. 8, no. 43, pp. 29478–29485, 2016, doi: 10.1021/acsami.6b09951.

[73] R. Francke, D. Cericola, R. Kötz, D. Weingarth, and S. R. Waldvogel, "Novel electrolytes for electrochemical double layer capacitors based on 1,1,1,3,3,3-hexafluoropropan-2-ol," *Electrochim. Acta*, vol. 62, pp. 372–380, 2012, doi: 10.1016/j.electacta.2011.12.050.

[74] B. E. Conway, *Electrochemical supercapacitors: scientific fundamentals and technological applications*. Springer Science & Business Media, 2013.

[75] M. J. Loveridge *et al.*, "Looking deeper into the Galaxy (Note 7)," *Batteries*, vol. 4, no. 1, p. 3, 2018.

[76] L. Demarconnay, E. Raymundo-Piñero, and F. Béguin, "A symmetric carbon/carbon supercapacitor operating at 1.6V by using a neutral aqueous solution," *Electrochem. commun.*, vol. 12, no. 10, pp. 1275–1278, 2010, doi: 10.1016/j.elecom.2010.06.036.

[77] L. Deng, Y. Gu, Y. Gao, Z. Ma, and G. Fan, "Carbon nanotubes/holey graphene hybrid film as binder-free electrode for flexible supercapacitors," *J. Colloid Interface Sci.*, vol. 494, pp. 355–362, 2017, doi: 10.1016/j.jcis.2017.01.062.

[78] M. Kaempgen, C. K. Chan, J. Ma, Y. Cui, and G. Gruner, "Printable Thin Film Supercapacitors Using Single-Walled Carbon Nanotubes," *Nano Lett.*, vol. 9, no. 5, pp. 1872–1876, 2009, doi: 10.1021/nl8038579.

[79] Y. Chang *et al.*, "Embedding Reduced Graphene Oxide in Bacterial Cellulose-Derived Carbon Nanofibril Networks for Supercapacitors," *ChemElectroChem*, vol. 4, no. 10, pp. 2448–2452, Jun. 2017, doi: 10.1002/celc.201700625.

[80] M. D. Stoller and R. S. Ruoff, "Best practice methods for determining an electrode material's performance for ultracapacitors," *Energy Environ. Sci.*, vol. 3, no. 9, pp. 1294–1301, 2010, doi: 10.1039/C0EE00074D.

[81] Y. Gogotsi and P. Simon, "True Performance Metrics in Electrochemical Energy Storage," *Science (80-.).*, vol. 334, no. 6058, p. 917, 2011, doi: 10.1126/science.1213003.

[82] C. Peng, X. Yan, R. Wang, J. Lang, Y. Ou, and Q. Xue, "Promising activated carbons derived from waste tea-leaves and their application in high performance

supercapacitors electrodes,” *Electrochim. Acta*, vol. 87, pp. 401–408, 2013, doi: 10.1016/j.electacta.2012.09.082.

[83] Z.-S. Wu, W. Ren, D.-W. Wang, F. Li, B. Liu, and H.-M. Cheng, “High-Energy MnO2 Nanowire/Graphene and Graphene Asymmetric Electrochemical Capacitors,” *ACS Nano*, vol. 4, no. 10, pp. 5835–5842, 2010, doi: 10.1021/nn101754k.

[84] J. Ge, G. Cheng, and L. Chen, “Transparent and flexible electrodes and supercapacitors using polyaniline/single-walled carbon nanotube composite thin films,” *Nanoscale*, vol. 3, no. 8, pp. 3084–3088, 2011, doi: 10.1039/C1NR10424A.

[85] J. Yu *et al.*, “Omnidirectionally Stretchable High-Performance Supercapacitor Based on Isotropic Buckled Carbon Nanotube Films,” *ACS Nano*, vol. 10, no. 5, pp. 5204–5211, 2016, doi: 10.1021/acsnano.6b00752.

[86] D. Yu and L. Dai, “Self-Assembled Graphene/Carbon Nanotube Hybrid Films for Supercapacitors,” *J. Phys. Chem. Lett.*, vol. 1, no. 2, pp. 467–470, 2010, doi: 10.1021/jz9003137.

[87] Y. S. Yun, H. H. Park, and H.-J. Jin, “Pseudocapacitive effects of N-doped carbon nanotube electrodes in supercapacitors,” *Materials (Basel).*, vol. 5, no. 7, pp. 1258–1266, 2012.

[88] N. Díez, C. Botas, R. Mysyk, E. Goikolea, T. Rojo, and D. Carriazo, “Highly packed graphene–CNT films as electrodes for aqueous supercapacitors with high volumetric performance,” *J. Mater. Chem. A*, vol. 6, no. 8, pp. 3667–3673, 2018, doi: 10.1039/C7TA10210K.

[89] X. Li *et al.*, “Self-supporting activated carbon/carbon nanotube/reduced graphene oxide flexible electrode for high performance supercapacitor,” *Carbon N. Y.*, vol. 129, pp. 236–244, 2018, doi: 10.1016/j.carbon.2017.11.099.

[90] R. Berenguer *et al.*, “Biomass-derived binderless fibrous carbon electrodes for ultrafast energy storage,” *Green Chem.*, vol. 18, no. 6, pp. 1506–1515, 2016, doi: 10.1039/C5GC02409A.

[91] S. Hu, S. Zhang, N. Pan, and Y.-L. Hsieh, “High energy density supercapacitors from lignin derived submicron activated carbon fibers in aqueous electrolytes,” *J. Power Sources*, vol. 270, pp. 106–112, 2014, doi: 10.1016/j.jpowsour.2014.07.063.

[92] S. Zhu, P.-L. Taberna, N. Zhao, and P. Simon, “Salt-template synthesis of mesoporous carbon monolith for ionogel-based supercapacitors,” *Electrochem. commun.*, vol. 96, pp. 6–10, 2018, doi: 10.1016/j.elecom.2018.09.003.

[93] L. Wei, N. Nitta, and G. Yushin, “Lithographically Patterned Thin Activated Carbon Films as a New Technology Platform for On-Chip Devices,” *ACS Nano*, vol. 7, no. 8, pp. 6498–6506, 2013, doi: 10.1021/nn4028129.

[94] T. Purkait, G. Singh, M. Singh, D. Kumar, and R. S. Dey, “Large area few-layer graphene with scalable preparation from waste biomass for high-performance supercapacitor,” *Sci. Rep.*, vol. 7, no. 1, p. 15239, 2017, doi: 10.1038/s41598-017-15463-w.

[95] Y. Li, Q. Zhang, J. Zhang, L. Jin, X. Zhao, and T. Xu, “A top-down approach for fabricating free-standing bio-carbon supercapacitor electrodes with a hierarchical structure,” *Sci. Rep.*, vol. 5, no. 1, p. 14155, 2015, doi: 10.1038/srep14155.

[96] Y. Zhang, H. Gao, X. Song, X. Kong, and H. Xu, “Preparation of Hierarchical Porous Carbon from Wheat Bran for Free-Standing Electrode of High Areal Capacitance Supercapacitor,” *ChemElectroChem*, vol. 6, no. 21, pp. 5486–5491, Jun. 2019, doi: 10.1002/celc.201901440.

[97] P. Xu *et al.*, “Carbon Nanotube Fiber Based Stretchable Wire-Shaped Supercapacitors,” *Adv. Energy Mater.*, vol. 4, no. 3, p. 1300759, Jun. 2014, doi: 10.1002/aenm.201300759.

[98] X. Yang, J. Zhu, L. Qiu, and D. Li, “Bioinspired Effective Prevention of Restacking in Multilayered Graphene Films: Towards the Next Generation of High-Performance Supercapacitors,” *Adv. Mater.*, vol. 23, no. 25, pp. 2833–2838, Jun. 2011, doi: 10.1002/adma.201100261.

[99] Q. Wang *et al.*, “Three-dimensional flower-like and hierarchical porous carbon materials as high-rate performance electrodes for supercapacitors,” *Carbon N. Y.*, vol. 67, pp. 119–127, 2014, doi: 10.1016/j.carbon.2013.09.070.

[100] M. F. El-Kady, V. Strong, S. Dubin, and R. B. Kaner, “Laser Scribing of High-Performance and Flexible Graphene-Based Electrochemical Capacitors,” *Science (80-.).*, vol. 335, no. 6074, p. 1326, 2012, doi: 10.1126/science.1216744.

[101] R. Vicentini *et al.*, “Core-niobium pentoxide carbon-shell nanoparticles decorating multiwalled carbon nanotubes as electrode for electrochemical capacitors,” *J. Power Sources*, vol. 434, 2019, doi: 10.1016/j.jpowsour.2019.226737.

[102] W. G. Nunes *et al.*, “Study of the aging process of nanostructured porous carbon-based electrodes in electrochemical capacitors filled with aqueous or organic electrolytes,” *J. Energy Storage*, vol. 28, no. December 2019, p. 101249, 2020, doi: 10.1016/j.est.2020.101249.

[103] L. M. Aleixo, “Voltametria: conceitos e técnicas,” *Rev. Chemkeys*, no. 3, pp. 1–21, 2018, doi: 10.20396/chemkeys.v0i3.9609.

[104] S. Reich and C. Thomsen, “Raman spectroscopy of graphite,” *Philos. Trans. R. Soc. A Math. Phys. Eng. Sci.*, vol. 362, no. 1824, pp. 2271–2288, 2004, doi: 10.1098/rsta.2004.1454.

[105] R. Vicentini *et al.*, “Raman probing carbon & aqueous electrolytes interfaces and molecular dynamics simulations towards understanding electrochemical properties under polarization conditions in supercapacitors,” *J. Energy Chem.*, Jan. 2021, doi: 10.1016/j.jechem.2021.01.003.

[106] A. C. Ferrari and D. M. Basko, “Raman spectroscopy as a versatile tool for studying the properties of graphene,” *Nat. Nanotechnol.*, vol. 8, no. 4, pp. 235–246, 2013, doi: 10.1038/nnano.2013.46.

[107] A. C. Ferrari, “Raman spectroscopy of graphene and graphite: Disorder, electron-phonon coupling, doping and nonadiabatic effects,” *Solid State Commun.*, vol. 143, no. 1–2, pp. 47–57, 2007, doi: 10.1016/j.ssc.2007.03.052.

[108] K. N. Kudin, B. Ozbas, H. C. Schniepp, R. K. Prud’homme, I. A. Aksay, and R. Car, “Raman spectra of graphite oxide and functionalized graphene sheets,” *Nano Lett.*, vol. 8, no. 1, pp. 36–41, 2008, doi: 10.1021/nl071822y.

[109] T. A. Silva *et al.*, “Electrochemical behaviour of vertically aligned carbon nanotubes and graphene oxide nanocomposite as electrode material,” *Electrochim. Acta*, vol. 119, pp. 114–119, Feb. 2014, doi: 10.1016/j.electacta.2013.12.024.

[110] A. O. Lobo, S. C. Ramos, E. F. Antunes, F. R. Marciano, V. J. Trava-Airoldi, and E. J. Corat, “Fast functionalization of vertically aligned multiwalled carbon nanotubes using

oxygen plasma," *Mater. Lett.*, vol. 70, pp. 89–93, Mar. 2012, doi: 10.1016/j.matlet.2011.11.071.

[111] H. Zanin, C. M. R. Rosa, N. Eliaz, P. W. May, F. R. Marciano, and A. O. Lobo, "Assisted deposition of nano-hydroxyapatite onto exfoliated carbon nanotube oxide scaffolds," *Nanoscale*, vol. 7, no. 22, pp. 10218–10232, Jun. 2015, doi: 10.1039/c4nr07317g.

[112] M. A. V. M. Grinet, H. Zanin, A. E. Campos Granato, M. Porcionatto, F. R. Marciano, and A. O. Lobo, "Fast preparation of free-standing nanohydroxyapatite-vertically aligned carbon nanotube scaffolds," *J. Mater. Chem. B*, vol. 2, no. 9, pp. 1196–1204, Mar. 2014, doi: 10.1039/c3tb21525c.

[113] E. Saito *et al.*, " Oxygen Plasma Exfoliated Vertically-Aligned Carbon Nanotubes as Electrodes for Ultrasensitive Stripping Detection of Pb 2+ ," *J. Electrochem. Soc.*, vol. 161, no. 5, pp. H321–H325, Mar. 2014, doi: 10.1149/2.039405jes.

[114] M. Pawlyta, J. N. Rouzaud, and S. Duber, "Raman microspectroscopy characterization of carbon blacks: Spectral analysis and structural information," *Carbon N. Y.*, vol. 84, no. 1, pp. 479–490, 2015, doi: 10.1016/j.carbon.2014.12.030.

[115] P. Trucano and R. Chen, "Structure of graphite by neutron diffraction," *Nature*, vol. 258, no. 5531, pp. 136–137, 1975, doi: 10.1038/258136a0.

[116] M. Thommes *et al.*, "Physisorption of gases, with special reference to the evaluation of surface area and pore size distribution (IUPAC Technical Report)," *Pure Appl. Chem.*, vol. 87, no. 9–10, pp. 1051–1069, Oct. 2015, doi: 10.1515/pac-2014-1117.

[117] J. Bisquert, G. Garcia-Belmonte, F. Fabregat-Santiago, and A. Compte, "Anomalous transport effects in the impedance of porous film electrodes," *Electrochem. commun.*, vol. 1, no. 9, pp. 429–435, 1999, doi: https://doi.org/10.1016/S1388-2481(99)00084-3.

[118] T. A. Centeno, O. Sereda, and F. Stoeckli, "Capacitance in carbon pores of 0.7 to 15 nm: A regular pattern," *Phys. Chem. Chem. Phys.*, vol. 13, no. 27, pp. 12403–12406, 2011, doi: 10.1039/c1cp20748b.

[119] R. Vicentini *et al.*, "Niobium pentoxide nanoparticles @ multi-walled carbon nanotubes and activated carbon composite material as electrodes for electrochemical capacitors," *Energy Storage Mater.*, vol. 22, 2019, doi: 10.1016/j.ensm.2019.08.007.

[120] W. G. Nunes, R. Vicentini, L. M. Da Silva, L. H. Costa, T. Tadeu, and H. Zanin, "Surface and Electrochemical Properties of Radially Oriented Multiwalled Carbon Nanotubes Grown on Stainless Steel Mesh," *J. Electrochem. Soc.*, vol. 165, no. 16, pp. A3684–A3696, Dec. 2018, doi: 10.1149/2.022816JES/XML.

[121] R. Vicentini *et al.*, "Highly stable nickel-aluminum alloy current collectors and highly defective multi-walled carbon nanotubes active material for neutral aqueous-based electrochemical capacitors," *J. Energy Storage*, vol. 23, pp. 116–127, Jun. 2019, doi: 10.1016/J.EST.2019.01.013.

[122] F. Béguin and E. Frackowiak, "Supercapacitors: Materials, Systems, and Applications," *Supercapacitors Mater. Syst. Appl.*, Mar. 2013, doi: 10.1002/9783527646661.

[123] H. Krienke, "Modern Aspects of Electrochemistry, No. 31," *Zeitschrift für Phys. Chemie*, vol. 213, no. 2, pp. 216–217, Feb. 1999, doi: 10.1524/ZPCH.1999.213.PART_2.216.

[124] A. J. De Bethune, "Atlas d'equilibres electrochimiques a 25 C (Pourbaix, Marcel)," *J. Chem. Educ.*, vol. 42, no. 10, p. A834, Oct. 1965, doi: 10.1021/ED042PA834.

[125] X. Bu, L. Su, Q. Dou, S. Lei, and X. Yan, "A low-cost 'water-in-salt' electrolyte for a 2.3 V high-rate carbon-based supercapacitor," *J. Mater. Chem. A*, vol. 7, no. 13, pp. 7541–7547, Mar. 2019, doi: 10.1039/C9TA00154A.

[126] M. Zhang, S. Makino, D. Mochizuki, and W. Sugimoto, "High-performance hybrid supercapacitors enabled by protected lithium negative electrode and 'water-in-salt' electrolyte," *J. Power Sources*, vol. 396, pp. 498–505, Aug. 2018, doi: 10.1016/J.JPOWSOUR.2018.06.037.

[127] P. K. Adusei *et al.*, "Fabrication and study of supercapacitor electrodes based on oxygen plasma functionalized carbon nanotube fibers," *J. Energy Chem.*, vol. 40, pp. 120–131, Jan. 2020, doi: 10.1016/J.JECHEM.2019.03.005.

[128] F. R. Costa, D. V. Franco, and L. M. Da Silva, "Electrochemical impedance spectroscopy study of the oxygen evolution reaction on a gas-evolving anode composed of lead dioxide microfibers," *Electrochim. Acta*, vol. 90, pp. 332–343, Feb. 2013, doi: 10.1016/J.ELECTACTA.2012.12.043.

[129] M. He, K. Fic, E. Frackowiak, P. Novák, and E. J. Berg, “Ageing phenomena in high-voltage aqueous supercapacitors investigated by in situ gas analysis,” *Energy Environ. Sci.*, vol. 9, no. 2, pp. 623–633, Feb. 2016, doi: 10.1039/C5EE02875B.

[130] P. Ratajczak, K. Jurewicz, and F. Béguin, “Factors contributing to ageing of high voltage carbon/carbon supercapacitors in salt aqueous electrolyte,” *J. Appl. Electrochem.*, vol. 44, no. 4, pp. 475–480, Apr. 2014, doi: 10.1007/S10800-013-0644-0/FIGURES/7.

[131] H. Chen, J. Di, Y. Jin, M. Chen, J. Tian, and Q. Li, “Active carbon wrapped carbon nanotube buckypaper for the electrode of electrochemical supercapacitors,” *J. Power Sources*, vol. 237, pp. 325–331, Sep. 2013, doi: 10.1016/J.JPOWSOUR.2013.02.082.

[132] M. P. Bichat, E. Raymundo-Piñero, and F. Béguin, “High voltage supercapacitor built with seaweed carbons in neutral aqueous electrolyte,” *Carbon N. Y.*, vol. 48, no. 15, pp. 4351–4361, Dec. 2010, doi: 10.1016/J.CARBON.2010.07.049.

[133] H. Tomiyasu, H. Shikata, K. Takao, N. Asanuma, S. Taruta, and Y. Y. Park, “An aqueous electrolyte of the widest potential window and its superior capability for capacitors,” *Sci. Reports 2017 71*, vol. 7, no. 1, pp. 1–12, Mar. 2017, doi: 10.1038/srep45048.

[134] Y. Z. Wu, Y. Ding, T. Hayat, A. Alsaedi, and S. Y. Dai, “Enlarged working potential window for MnO2 supercapacitors with neutral aqueous electrolytes,” *Appl. Surf. Sci.*, vol. 459, pp. 430–437, Nov. 2018, doi: 10.1016/J.APSUSC.2018.07.147.

[135] M. Bahdanchyk, M. Hashempour, and A. Vicenzo, “Evaluation of the operating potential window of electrochemical capacitors,” *Electrochim. Acta*, vol. 332, p. 135503, Feb. 2020, doi: 10.1016/J.ELECTACTA.2019.135503.

[136] Y. Wang, J. Cao, Y. Zhou, J.-H. Ouyang, D. Jia, and L. Guo, “Ball-Milled Graphite as an Electrode Material for High Voltage Supercapacitor in Neutral Aqueous Electrolyte,” *J. Electrochem. Soc.*, vol. 159, no. 5, pp. A579–A583, Mar. 2012, doi: 10.1149/2.071205JES/XML.

[137] D. Reber, R. S. Kühnel, and C. Battaglia, “High-voltage aqueous supercapacitors based on NaTFSI,” *Sustain. Energy Fuels*, vol. 1, no. 10, pp. 2155–2161, Nov. 2017, doi: 10.1039/C7SE00423K.

[138] A. Tatlisu, Z. Huang, and R. Chen, “High-Voltage and Low-Temperature Aqueous Supercapacitor Enabled by ‘Water-in-Imidazolium Chloride’ Electrolytes,” *ChemSusChem*, vol. 11, no. 22, pp. 3899–3904, Nov. 2018, doi: 10.1002/CSSC.201802046.

[139] H. Xia, Y. Shirley Meng, G. Yuan, C. Cui, and L. Lu, “A symmetric RuO 2RuO 2 supercapacitor operating at 1.6 v by using a neutral aqueous electrolyte,” *Electrochem. Solid-State Lett.*, vol. 15, no. 4, p. A60, Feb. 2012, doi: 10.1149/2.023204ESL/XML.

[140] Q. Gao, L. Demarconnay, E. Raymundo-Piñero, and F. Béguin, “Exploring the large voltage range of carbon/carbon supercapacitors in aqueous lithium sulfate electrolyte,” *Energy Environ. Sci.*, vol. 5, no. 11, pp. 9611–9617, Oct. 2012, doi: 10.1039/C2EE22284A.

[141] Q. T. Qu, Y. Shi, S. Tian, Y. H. Chen, Y. P. Wu, and R. Holze, “A new cheap asymmetric aqueous supercapacitor: Activated carbon//NaMnO2,” *J. Power Sources*, vol. 194, no. 2, pp. 1222–1225, Dec. 2009, doi: 10.1016/J.JPOWSOUR.2009.06.068.

[142] X. Yang, Y. S. He, G. Jiang, X. Z. Liao, and Z. F. Ma, “High voltage supercapacitors using hydrated graphene film in a neutral aqueous electrolyte,” *Electrochem. commun.*, vol. 13, no. 11, pp. 1166–1169, Nov. 2011, doi: 10.1016/J.ELECOM.2011.09.006.

[143] K. Fic, G. Lota, M. Meller, and E. Frackowiak, “Novel insight into neutral medium as electrolyte for high-voltage supercapacitors,” *Energy Environ. Sci.*, vol. 5, no. 2, pp. 5842–5850, Jan. 2012, doi: 10.1039/C1EE02262H.

[144] L. Demarconnay, E. Raymundo-Piñero, and F. Béguin, “A symmetric carbon/carbon supercapacitor operating at 1.6 V by using a neutral aqueous solution,” *Electrochem. commun.*, vol. 12, no. 10, pp. 1275–1278, Oct. 2010, doi: 10.1016/J.ELECOM.2010.06.036.

[145] V. Khomenko, E. Raymundo-Piñero, E. Frackowiak, and F. Béguin, “High-voltage asymmetric supercapacitors operating in aqueous electrolyte,” *Appl. Phys. A 2005 824*, vol. 82, no. 4, pp. 567–573, Nov. 2005, doi: 10.1007/S00339-005-3397-8.

[146] G. Hasegawa, K. Kanamori, T. Kiyomura, H. Kurata, T. Abe, and K. Nakanishi, “Hierarchically Porous Carbon Monoliths Comprising Ordered Mesoporous Nanorod Assemblies for High-Voltage Aqueous Supercapacitors,” *Chem. Mater.*, vol. 28, no. 11, pp. 3944–3950, Jun. 2016, doi:

10.1021/ACS.CHEMMATER.6B01261/SUPPL_FILE/CM6B01261_SI_001.PDF.

[147] J. Suárez-Guevara, V. Ruiz, and P. Gomez-Romero, “Hybrid energy storage: high voltage aqueous supercapacitors based on activated carbon–phosphotungstate hybrid materials,” *J. Mater. Chem. A*, vol. 2, no. 4, pp. 1014–1021, Dec. 2013, doi: 10.1039/C3TA14455K.

[148] L. Zhao, Y. Qiu, J. Yu, X. Deng, C. Dai, and X. Bai, “Carbon nanofibers with radially grown graphene sheets derived from electrospinning for aqueous supercapacitors with high working voltage and energy density,” *Nanoscale*, vol. 5, no. 11, pp. 4902–4909, May 2013, doi: 10.1039/C3NR33927K.

[149] X. Yang *et al.*, “Removal of natural organic matter in water using functionalised carbon nanotube buckypaper,” *Carbon N. Y.*, vol. 59, pp. 160–166, Aug. 2013, doi: 10.1016/J.CARBON.2013.03.005.

[150] E. F. Antunes, A. O. Lobo, E. J. Corat, V. J. Trava-Airoldi, A. A. Martin, and C. Veríssimo, “Comparative study of first- and second-order Raman spectra of MWCNT at visible and infrared laser excitation,” *Carbon N. Y.*, vol. 44, no. 11, pp. 2202–2211, Sep. 2006, doi: 10.1016/j.carbon.2006.03.003.

[151] R. Vicentini, L. M. Da Silva, E. P. Cecilio Junior, T. A. Alves, W. G. Nunes, and H. Zanin, “How to Measure and Calculate Equivalent Series Resistance of Electric Double-Layer Capacitors,” *Molecules*, vol. 24, no. 8, p. 1452, Apr. 2019, doi: 10.3390/molecules24081452.

[152] L. M. Da Silva *et al.*, “Reviewing the fundamentals of supercapacitors and the difficulties involving the analysis of the electrochemical findings obtained for porous electrode materials,” *Energy Storage Materials*, vol. 27. Elsevier B.V., pp. 555–590, May 01, 2020, doi: 10.1016/j.ensm.2019.12.015.

[153] K. Chiba, T. Ueda, Y. Yamaguchi, Y. Oki, F. Saiki, and K. Naoi, “Electrolyte Systems for High Withstand Voltage and Durability II. Alkylated Cyclic Carbonates for Electric Double-Layer Capacitors,” *J. Electrochem. Soc.*, vol. 158, no. 12, p. A1320, Nov. 2011, doi: 10.1149/2.038112jes.

[154] C. Zhong, Y. Deng, W. Hu, J. Qiao, L. Zhang, and J. Zhang, “A review of electrolyte materials and compositions for electrochemical supercapacitors,” *Chem. Soc. Rev.*, vol. 44, no. 21, pp. 7484–7539, 2015, doi: 10.1039/c5cs00303b.

[155] C. F. Liu, Y. C. Liu, T. Y. Yi, and C. C. Hu, “Carbon materials for high-voltage supercapacitors,” *Carbon*, vol. 145. Elsevier Ltd, pp. 529–548, Apr. 01, 2019, doi: 10.1016/j.carbon.2018.12.009.

[156] X. Wang, Y. Li, F. Lou, M. E. Melandsø Buan, E. Sheridan, and D. Chen, “Enhancing capacitance of supercapacitor with both organic electrolyte and ionic liquid electrolyte on a biomass-derived carbon,” *RSC Adv.*, vol. 7, no. 38, pp. 23859–23865, Apr. 2017, doi: 10.1039/c7ra01630a.

[157] M. P. Bichat, E. Raymundo-Piñero, and F. Béguin, “High voltage supercapacitor built with seaweed carbons in neutral aqueous electrolyte,” *Carbon N. Y.*, vol. 48, no. 15, pp. 4351–4361, Nov. 2010, doi: 10.1016/j.carbon.2010.07.049.

[158] A. G. Berezhnaya, V. V. Chernyavina, and A. L. Sinyavin, “Electrochemical Parameters of Supercapacitors on a Neutral Aqueous Electrolyte with Various Electrode Materials,” *Russ. J. Electrochem.*, vol. 55, no. 8, pp. 802–806, Aug. 2019, doi: 10.1134/S1023193519080044.

[159] M. Zhang, Y. Li, and Z. Shen, “‘Water-in-salt’ electrolyte enhanced high voltage aqueous supercapacitor with all-pseudocapacitive metal-oxide electrodes,” *J. Power Sources*, vol. 414, pp. 479–485, Feb. 2019, doi: 10.1016/j.jpowsour.2019.01.037.

[160] M. He, K. Fic, E. Frackowiak, P. Novák, and E. J. Berg, “Ageing phenomena in high-voltage aqueous supercapacitors investigated by in situ gas analysis,” *Energy Environ. Sci.*, vol. 9, no. 2, pp. 623–633, Feb. 2016, doi: 10.1039/c5ee02875b.

[161] K. Ni *et al.*, “In Operando Probing of Lithium-Ion Storage on Single-Layer Graphene,” *Adv. Mater.*, vol. 31, no. 23, p. 1808091, Jun. 2019, doi: 10.1002/adma.201808091.

[162] W. G. Nunes *et al.*, “Nickel oxide nanoparticles supported onto oriented multi-walled carbon nanotube as electrodes for electrochemical capacitors,” *Electrochim. Acta*, vol. 298, pp. 468–483, Mar. 2019, doi: 10.1016/j.electacta.2018.12.102.

[163] M. Ohnishi, K. Suzuki, and H. Miura, “Effects of uniaxial compressive strain on the electronic-transport properties of zigzag carbon nanotubes,” *Nano Res.*, vol. 9, no. 5, pp. 1267–1275, May 2016, doi: 10.1007/s12274-016-1022-0.

[164] E. A. Korznikova *et al.*, “Chain Model for Carbon Nanotube Bundle under Plane Strain Conditions,” *Materials (Basel).*, vol. 12, no. 23, p. 3951, Nov. 2019, doi:

10.3390/ma12233951.

[165] L. Kirkayak, “Strain rate effects on compressive behavior of covalently bonded CNT networks,” *Phys. E Low-Dimensional Syst. Nanostructures*, vol. 80, pp. 168–175, Jun. 2016, doi: 10.1016/j.physe.2016.02.004.

[166] T. Borkar *et al.*, “Strength versus ductility in carbon nanotube reinforced nickel matrix nanocomposites,” *J. Mater. Res.*, vol. 29, no. 6, pp. 761–769, Mar. 2014, doi: 10.1557/jmr.2014.53.

[167] T. J. B. Holland and S. A. T. Redfern, “Unit cell refinement from powder diffraction data: the use of regression diagnostics,” *Mineral. Mag.*, vol. 61, no. 404, pp. 65–77, Feb. 1997, doi: 10.1180/minmag.1997.061.404.07.

[168] E. Witt, C. V. Chandran, and P. Heitjans, “Slow ion exchange in crystalline Li2SO4 ·H2OA 6Li 2D EXSY NMR investigation,” *Solid State Ionics*, vol. 304, pp. 60–64, Jun. 2017, doi: 10.1016/j.ssi.2017.03.016.

[169] W. Lang and R. Claus, “The orientation of water molecules in monoclinic Li2SO4·H2O investigated by light scattering,” *J. Phys. Chem. Solids*, vol. 44, no. 8, pp. 789–791, Jan. 1983, doi: 10.1016/0022-3697(83)90011-2.

[170] O. Schmidt, S. Gorfman, L. Bohatý, E. Neumann, B. Engelen, and U. Pietsch, “Investigations of the bond-selective response in a piezoelectric Li 2SO4·H2O crystal to an applied external electric field,” *Acta Crystallogr. Sect. A Found. Crystallogr.*, vol. 65, no. 4, pp. 267–275, Jun. 2009, doi: 10.1107/S0108767309015566.

[171] X. Li *et al.*, “Water Splitting: From Electrode to Green Energy System,” *Nano-Micro Letters*, vol. 12, no. 1. Springer, Jun. 01, 2020, doi: 10.1007/s40820-020-00469-3.

[172] J. M. Gonçalves, P. R. Martins, K. Araki, and L. Angnes, “Recent progress in water splitting and hybrid supercapacitors based on nickel-vanadium layered double hydroxides,” *Journal of Energy Chemistry*, vol. 57. Elsevier B.V., pp. 496–515, Jun. 01, 2021, doi: 10.1016/j.jechem.2020.08.047.

[173] A. Battistel, C. R. Dennison, A. Lesch, and H. H. Girault, “Local Study on Hydrogen and Hydrogen Gas Bubble Formation on a Platinum Electrode,” *J. Phys. Chem. C*, vol. 123, no. 17, pp. 10849–10856, May 2019, doi: 10.1021/acs.jpcc.8b10920.

[174] Q. Chen, R. Ranaweera, and L. Luo, “Hydrogen Bubble Formation at Hydrogen-

Insertion Electrodes," *J. Phys. Chem. C*, vol. 122, no. 27, pp. 15421–15426, Jul. 2018, doi: 10.1021/acs.jpcc.8b03770.

[175] H. B. Liu, D. Zhong, J. Han, L. M. Pan, and Y. Liu, "Hydrogen bubble evolution from magnetized nickel wire electrode," *Int. J. Hydrogen Energy*, vol. 44, no. 60, pp. 31724–31730, Dec. 2019, doi: 10.1016/j.ijhydene.2019.10.063.

[176] R. R. Hacha, A. G. Merma, H. J. B. Couto, and M. L. Torem, "Measurement and analysis of H2 and O2 bubbles diameter produced by electroflotation processes in a modified Partridge-Smith cell," *Powder Technol.*, vol. 342, pp. 308–320, Jan. 2019, doi: 10.1016/j.powtec.2018.09.062.

[177] K. J. Vachaparambil and K. E. Einarsrud, "Numerical simulation of continuum scale electrochemical hydrogen bubble evolution," *Appl. Math. Model.*, vol. 98, pp. 343–377, Oct. 2021, doi: 10.1016/j.apm.2021.05.007.

[178] A. Coskun Avci and E. Toklu, "A new analysis of two phase flow on hydrogen production from water electrolysis," *Int. J. Hydrogen Energy*, Apr. 2021, doi: 10.1016/j.ijhydene.2021.03.180.

[179] H. Seyyedhosseinzadeh, F. Mahboubi, and A. Azadmehr, "Estimation on diffusion coefficient of lithium ions at the interface of LiNi 0.5 Mn 1.5 O 4 /electrolyte in Li-ion battery," doi: 10.1007/s11581-014-1189-x.

[180] J. G. Albright, "The Crystal Structure of Lithium Sulphate," *Zeitschrift für Krist. - Cryst. Mater.*, vol. 84, no. 1–6, pp. 150–158, Oct. 1933, doi: 10.1524/zkri.1933.84.1.150.

[181] G. E. Ziegler, " The Crystal Structure of Lithium Sulphate Mono-Hydrate, Li 2 SO 4 ·H 2 O. ," *Zeitschrift für Krist. - Cryst. Mater.*, vol. 89, no. 1–6, pp. 456–461, Dec. 1934, doi: 10.1524/zkri.1934.89.1.456.

[182] P. J. Pallister, I. L. Moudrakovski, G. D. Enright, and J. A. Ripmeester, "Structural assessment of anhydrous sulfates with high field 33S solid state NMR and first principles calculations," *CrystEngComm*, vol. 15, no. 43, pp. 8808–8822, Nov. 2013, doi: 10.1039/c3ce41233d.

[183] A. C. Larson, "The crystal structure of Li2SO4.H2O. A three-dimensional refinement," *Acta Crystallogr.*, vol. 18, no. 4, pp. 717–724, 1965, doi:

10.1107/S0365110X65001652.

[184] A. G. Nord, “ Crystal structure of β-Li 2 SO 4 ,” *Acta Crystallogr. Sect. B Struct. Crystallogr. Cryst. Chem.*, vol. 32, no. 3, pp. 982–983, Mar. 1976, doi: 10.1107/s0567740876004433.

[185] J. O. Lundgren, Å. Kvick, M. Karppinen, R. Liminga, and S. C. Abrahams, “Neutron diffraction structural study of pyroelectric Li2SO 4·H2O at 293, 80, and 20 K,” *J. Chem. Phys.*, vol. 80, no. 1, pp. 423–430, Aug. 1984, doi: 10.1063/1.446465.

[186] N. Batisse and E. Raymundo-Piñero, “Pulsed Electrochemical Mass Spectrometry for Operando Tracking of Interfacial Processes in Small-Time-Constant Electrochemical Devices such as Supercapacitors,” *ACS Appl. Mater. Interfaces*, vol. 9, no. 47, pp. 41224–41232, Nov. 2017, doi: 10.1021/acsami.7b12068.

[187] P. Przygocki, P. Ratajczak, and F. Béguin, “Quantification of the Charge Consuming Phenomena under High-Voltage Hold of Carbon/Carbon Supercapacitors by Coupling Operando and Post-Mortem Analyses,” *Angew. Chemie - Int. Ed.*, vol. 58, no. 50, pp. 17969–17977, Dec. 2019, doi: 10.1002/anie.201907914.

[188] K. Fic, M. He, E. J. Berg, P. Novák, and E. Frackowiak, “Comparative operando study of degradation mechanisms in carbon-based electrochemical capacitors with Li2SO4 and LiNO3 electrolytes,” *Carbon N. Y.*, vol. 120, pp. 281–293, Aug. 2017, doi: 10.1016/j.carbon.2017.05.061.

[189] P. Pasierb, S. Komornicki, M. Rokita, and M. Rękas, “Structural properties of Li2CO3-BaCO3 system derived from IR and Raman spectroscopy,” in *Journal of Molecular Structure*, Sep. 2001, vol. 596, no. 1–3, pp. 151–156, doi: 10.1016/S0022-2860(01)00703-7.

[190] J. B. Raoof, S. R. Hosseini, and S. Z. Mousavi-Sani, “Improved hydrogen evolution on glassy carbon electrode modified with novel Pt/cetyltrimethylammonium bromide nanoscale aggregates,” *Cuihua Xuebao/Chinese J. Catal.*, vol. 36, no. 2, pp. 216–220, Feb. 2015, doi: 10.1016/S1872-2067(14)60207-2.

[191] M. P. J. Brennan and O. R. Brown, “Carbon electrodes: Part 1. Hydrogen evolution in acidic solution,” *J. Appl. Electrochem.*, vol. 2, no. 1, pp. 43–49, Feb. 1972, doi: 10.1007/BF00615191.

[192] A. Koca, “Hydrogen evolution reaction on glassy carbon electrode modified with titanyl phthalocyanines,” *Int. J. Hydrogen Energy*, vol. 34, no. 5, pp. 2107–2112, Mar. 2009, doi: 10.1016/j.ijhydene.2009.01.013.

[193] Y. Yi *et al.*, “Electrochemical corrosion of a glassy carbon electrode,” *Catal. Today*, vol. 295, pp. 32–40, Oct. 2017, doi: 10.1016/j.cattod.2017.07.013.

[194] C. Sun *et al.*, “Graphene-Co3O4 nanocomposite as an efficient bifunctional catalyst for lithium-air batteries,” *J. Mater. Chem. A*, vol. 2, no. 20, pp. 7188–7196, May 2014, doi: 10.1039/c4ta00802b.

[195] M. Islam, M.-G. Jeong, F. Ghani, and H.-G. Jung, “Micro Emulsion Synthesis of LaCoO 3 Nanoparticles and their Electrochemical Catalytic Activity,” *J. Electrochem. Sci. Technol*, vol. 6, no. 4, p. 121, 2015, doi: 10.5229/JECST.2015.6.4.121.

[196] S. Osswald, E. Flahaut, H. Ye, and Y. Gogotsi, “Elimination of D-band in Raman spectra of double-wall carbon nanotubes by oxidation,” *Chem. Phys. Lett.*, vol. 402, no. 4–6, pp. 422–427, Feb. 2005, doi: 10.1016/j.cplett.2004.12.066.

[197] Z. Yan *et al.*, “Solvothermal-assisted liquid-phase exfoliation of large size and high quality black phosphorus,” *J. Mater.*, vol. 4, no. 2, pp. 129–134, Jun. 2018, doi: 10.1016/j.jmat.2018.01.003.

[198] S. L. Medway, C. A. Lucas, A. Kowal, R. J. Nichols, and D. Johnson, “In situ studies of the oxidation of nickel electrodes in alkaline solution,” *J. Electroanal. Chem.*, vol. 587, no. 1, pp. 172–181, Feb. 2006, doi: 10.1016/j.jelechem.2005.11.013.

[199] P. Oliva *et al.*, “Review of the structure and the electrochemistry of nickel hydroxides and oxy-hydroxides,” *J. Power Sources*, vol. 8, no. 2, pp. 229–255, Jan. 1982, doi: 10.1016/0378-7753(82)80057-8.

[200] N. Wright, “Application of Infrared Spectroscopy to Industrial Research,” *Ind. Eng. Chem. - Anal. Ed.*, vol. 13, no. 1, pp. 1–8, 1941, doi: 10.1021/i560089a001.

APPENDIX

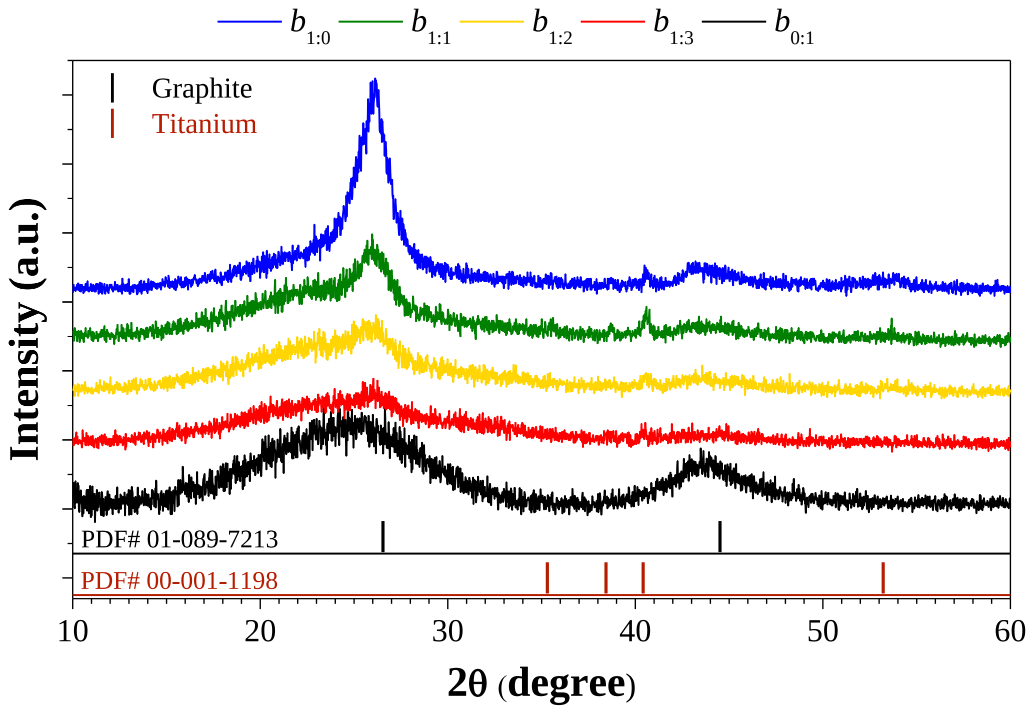

Figure A.1. XRD of the carbon materials MWCNT ($b_{1:0}$) in blue; MWCNT:AC ($b_{1:1}$, $b_{1:2}$, and $b_{1:3}$) in green, yellow and red; and AC in black. The Titanium corresponds to the hexagonal phase of spatial group *P63/mmc* (PDF# 00-001-1198) [200], which was the catalyst for MWCNT preparation.

Table A.1. Influence of the MWCNT:AC ratio on the specific (gravimetric) capacitance (SC) and the equivalent series resistance (ESR) as a function of the applied voltage.

Electrode	SC (F g^{-1})								
	1.0 V	1.1 V	1.2 V	1.3 V	1.4 V	1.5 V	1.6 V	1.7 V	1.8 V
$b_{1:0}$	7.59	7.71	7.79	7.86	7.95	8.07	8.18	8.26	8.34
$b_{1:1}$	45.87	46.23	46.25	46.02	45.82	45.64	45.59	45.58	45.54
$b_{1:2}$	49.47	49.45	49.34	49.19	49.03	48.95	48.99	49.35	49.81
$b_{1:3}$	52.75	52.08	53.86	54.14	54.30	54.33	54.36	54.41	54.36
Note:	Data extracted from the GCD data at 0.15 A g^{-1}.								
	ESR* (mΩ g)								
$b_{1:0}$	245.5	242.5	239.6	235.9	231.8	228.0	222.0	214.5	204.7
$b_{1:1}$	116.8	118.3	118.8	120.9	123.4	123.9	124.2	127.9	133.9
$b_{1:2}$	133.1	132.9	132.1	130.8	129.7	128.9	130.8	134.2	143.5
$b_{1:3}$	155.2	203.9	155.6	155.4	154.9	154.9	157.9	160.7	160.8

* ESR values were calculated from GCD data using the relation ESR (mΩ g) = $\Delta U/2I$, where ΔU (V) is the voltage drop, I (A g–1) is the modulus of the applied specific current, and 2 is the rational normalizing factor proposed by Vicentini et al. [151].

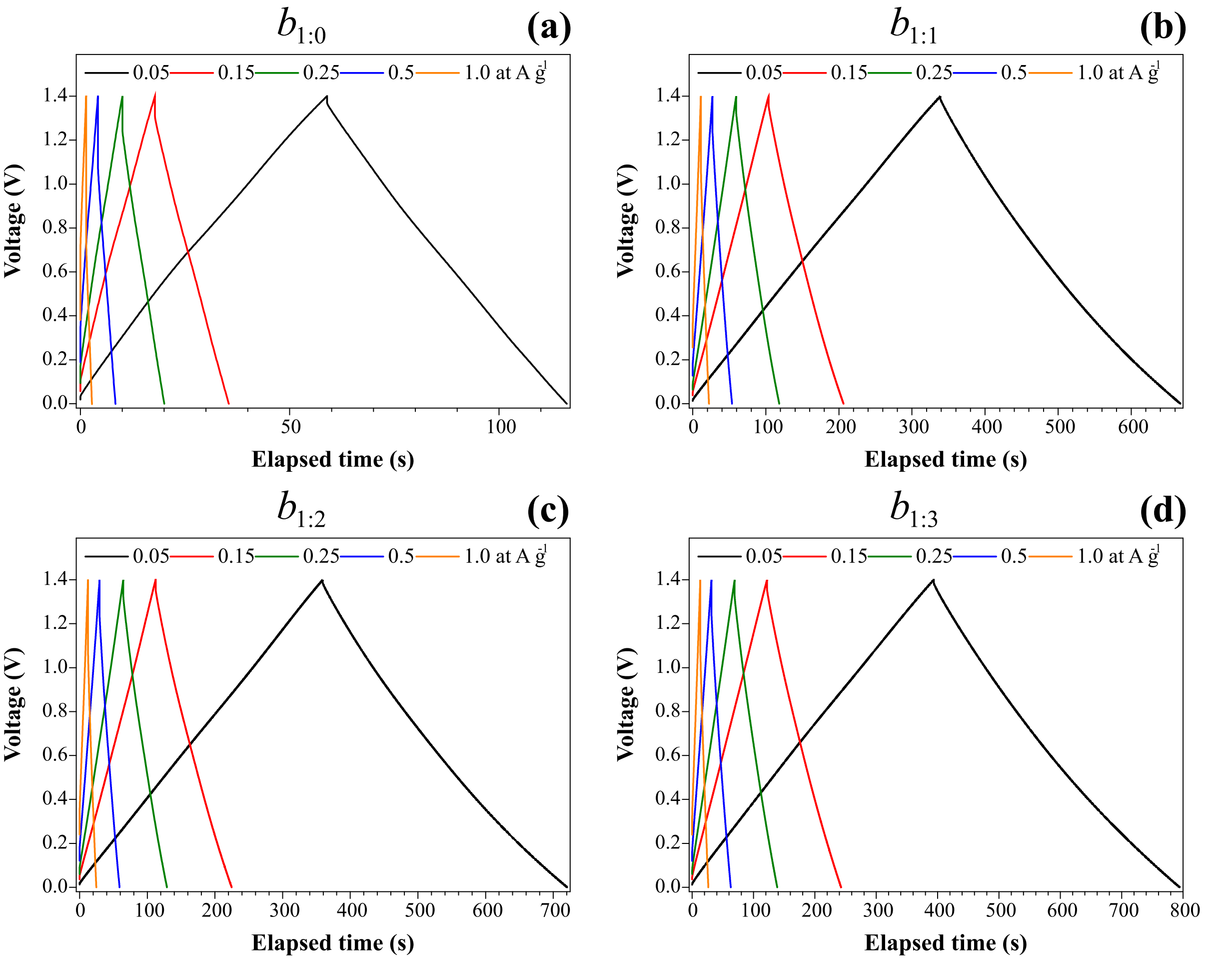

Figure A.2. GCD data at different applied gravimetric currents. (a) $b_{1:0}$, (b) $b_{1:1}$, (c) $b_{1:2}$, and (d) $b_{1:3}$.

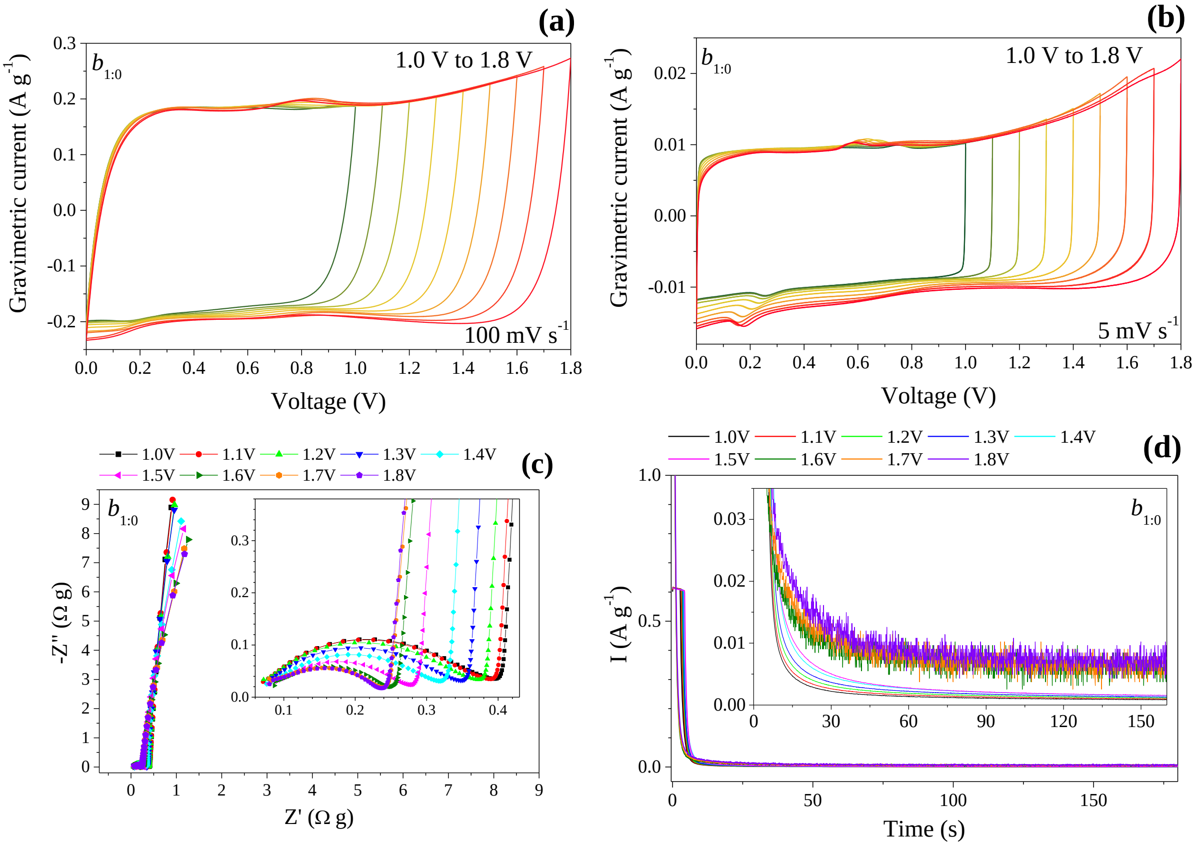

Figure A.3. Defining the working voltage window (WVW) of the symmetric coin cell (CR 2032). Electrodes: $b_{1:0}$ sample. Electrolyte: 1.0 mol dm^{-3} Li_2SO_4 aqueous solution. We performed (a & b) CV, (c) EIS, and (d) SSC experiments at different cell voltages.

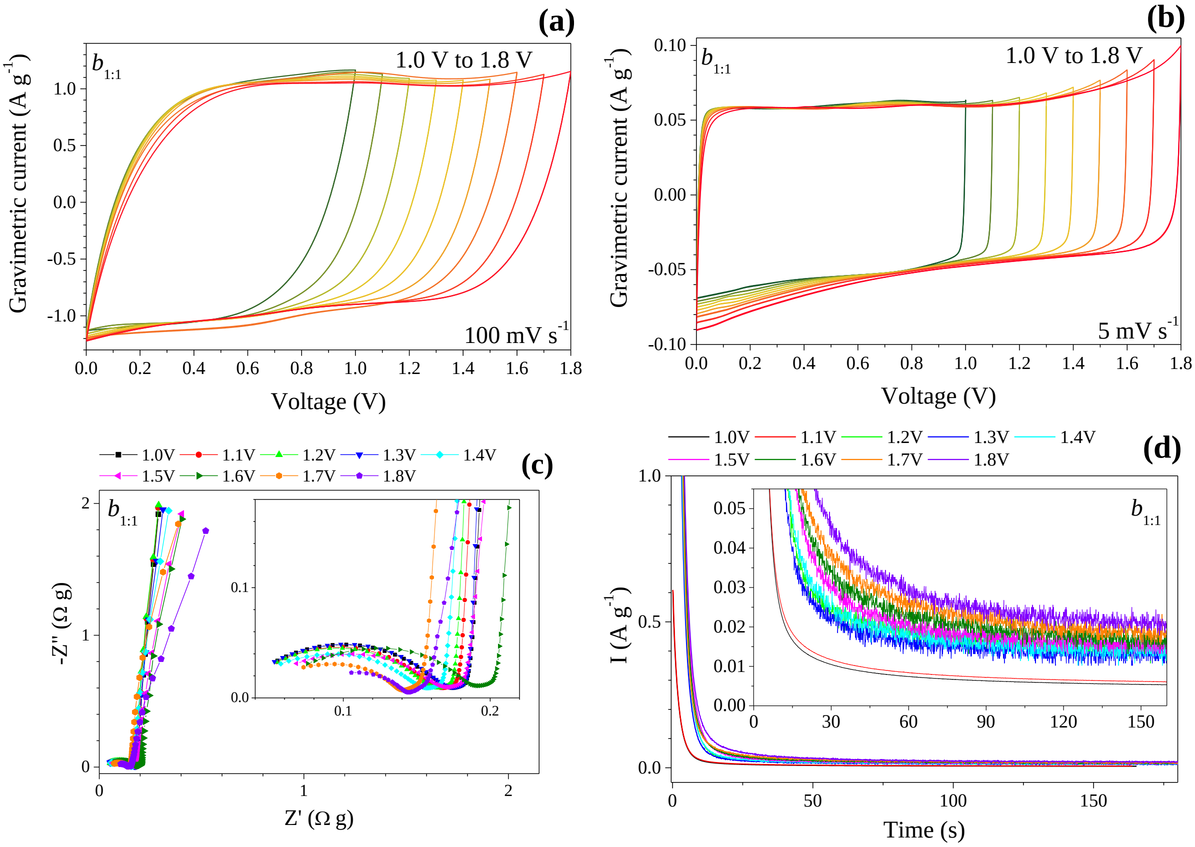

Figure A.4. Defining the working voltage window (WVW) of the symmetric coin cell (CR 2032). Electrodes: $b_{1:1}$ sample. Electrolyte: 1.0 mol dm^{-3} Li_2SO_4 aqueous solution. We performed (a & b) CV, (c) EIS, and (d) SSC experiments at different cell voltages.

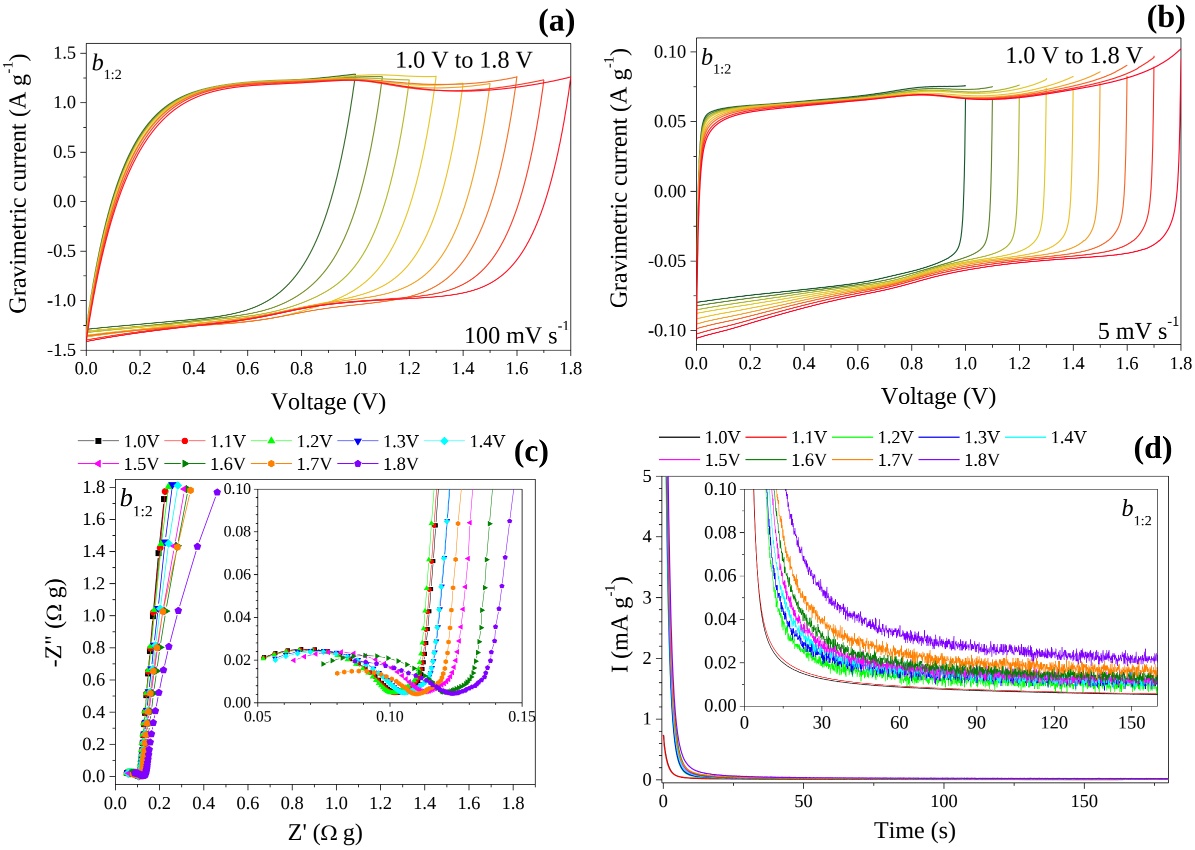

Figure A.5. Defining the working voltage window (WVW) of the symmetric coin cell (CR 2032). Electrodes: *b*$_{1:2}$ sample. Electrolyte: 1.0 mol dm^{-3} Li_2SO_4 aqueous solution. We performed (a & b) CV, (c) EIS, and (d) SSC experiments at different cell voltages.

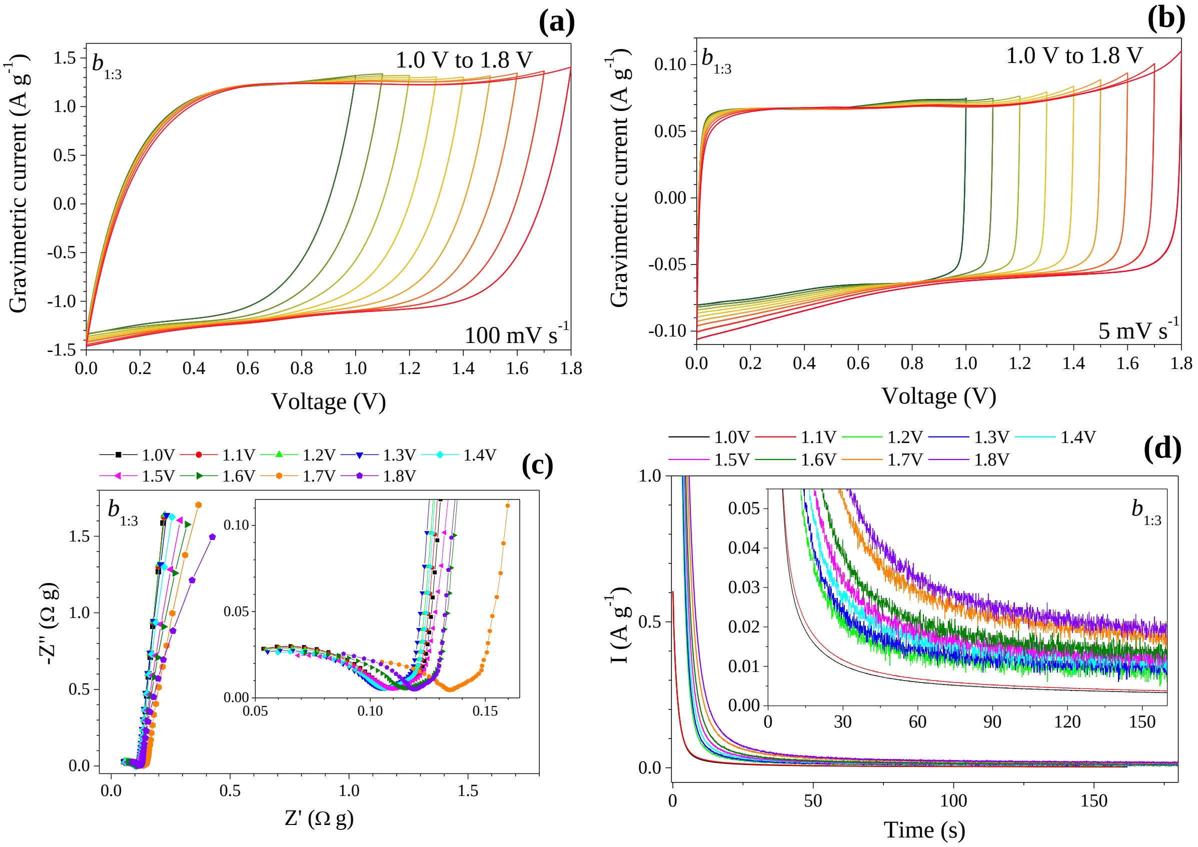

Figure A.6. Defining the working voltage window (WVW) of the symmetric coin cell (CR 2032). Electrodes: $b_{1:3}$ sample. Electrolyte: 1.0 mol dm^{-3} Li$_2$SO$_4$ aqueous solution. We performed (a & b) CV, (c) EIS, and (d) SSC experiments at different cell voltages.